ABSTRACT

Title of Thesis:

CHARACTERIZATION OF FATIGUE
CRACK GROWTH IN
UNIDIRECTIONAL CARBON FIBER
EPOXY COMPOSITES USING
DIGITAL IMAGE CORRELATION

Prakhar Singh, Master of Science, 2014

Directed By:

Professor Hugh A. Bruck
Department of Mechanical Engineering

This work studies fatigue fracture behavior of carbon fiber laminated composites by measuring deformation fields directly from the surface of the material using Digital Image Correlation (DIC). Energy release rate of laminated composites was determined from DIC measurements using Linear Elastic Fracture Mechanics (LEFM) theory under different mixed mode loading. Crack tip location was more accurately identified using the DIC and it was found that the strain energy release rate strongly depends on accurate identification of crack tip. The energy release rate determined from direct deformation measurement was compared with that obtained from global load displacement response of the materials as per ASTM standard. Evolution of energy release rate under cyclic loading has been quantified. Attempt has been made to identify the micro-mechanisms in the material under fatigue load through high magnification imaging and deformation analysis. The present work is an attempt to utilize the full field measurement of deformation around the crack tip to characterize fatigue fracture behavior.

CHARACTERIZATION OF FATIGUE CRACK GROWTH IN UNIDIRECTIONAL CARBON FIBER EPOXY COMPOSITES USING DIGITAL IMAGE CORRELATION

By

Prakhar Singh

Thesis submitted to the Faculty of the Graduate School of the
University of Maryland, College Park, in partial fulfillment
of the requirements for the degree of
Master of Science
2014

Advisory Committee:
Professor Hugh A. Bruck, Chair
Professor Sung W. Lee
Professor Patrick McCluskey

Acknowledgements

I wish to acknowledge and thank Dr. Hugh Bruck for his guidance, encouragement and motivation that has made this work possible and in the process helped me develop a knack for problem solving.

I also wish to acknowledge the thesis committee members for their suggestions, assistance and instructions.

This work would not have been possible without the mentorship of Sandip Haldar, who helped me grasp the basics of experimental mechanics and provided valuable guidance during the entirety of this research.

I thank Ananth Virakhti for his input on the simulation aspect of this research.

Lastly, I would like to acknowledge my parents for providing all the love and support over the years and for understanding that I was working in the lab if not biking outside.

Table of Contents

List of Tables

List of Figures

1 Introduction

1.1 Background

Over the past five decades there has been a prevalent change in the way industry utilizes materials. The end of the Second World War saw a paradigm shift away from heavy, homogeneous metals and towards more versatile and lightweight polymer matrix composites. Composites were first used immediately after the Second World War in the construction of small personnel boats for the US Navy. These boats proved to be stiff, strong and easy to repair, and these attributes led to a rapid expansion of composite use in other types of US naval craft between mid-1940s and 1960s. The US Navy also used composites in deckhouses for small ships, masts for some communication ships, piping for destroyers, and fairwaters and castings for submarines. [1] Composites have found a wide scale use in the airplane industry today, which is very well elaborated by its use in Boeing 787 Dreamliner.
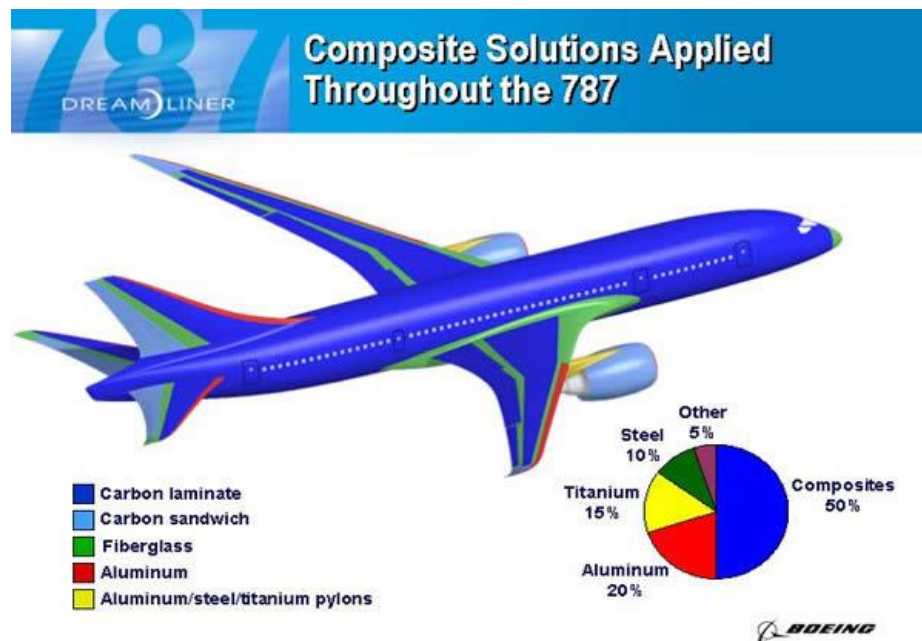
Figure 1.1 ©Boeing 787: A state of the art example showing the use of CFRP [2]

"Emerging technologies are driving the composites business into the future. The transportation market is a leading market, especially trucks. As world economies face inevitable competition for petroleum supplies, we are on the cusp of development for new categories of energy-efficient vehicles. But the integration of technology and the composites business is evident in other markets too. The emerging requirements for larger wind turbines, seismic protection, ballistic protection and infrastructure applications also lead the way for expanding the composites market."[3].

The Composites Market Report 2012 [4] reports that about 95% of the carbon fiber used in composite materials is processed into carbon fiber reinforced plastic (CRP). The rest is used in composites with matrices based on carbon, ceramic or metal. In 2011, the global composites market was valued at € 72 billion. Assuming an annual growth rate of around 6%, the market volume is estimated to reach € 91 billion by 2015. A growth rate of 13%-[JEC] or 17%[McKinsey] is expected for the CRP market, which represents only a small part of the composites market. Single aisle aircraft, such as the A320 – Neo or Boeing 737-Max, account for 70% of the fleet of passenger aircrafts that use carbon fiber composites [4]. However, the proportion of composites used in these aircraft is much smaller than in the new Boeing 786 and Airbus A340 wide-body aircraft [4].
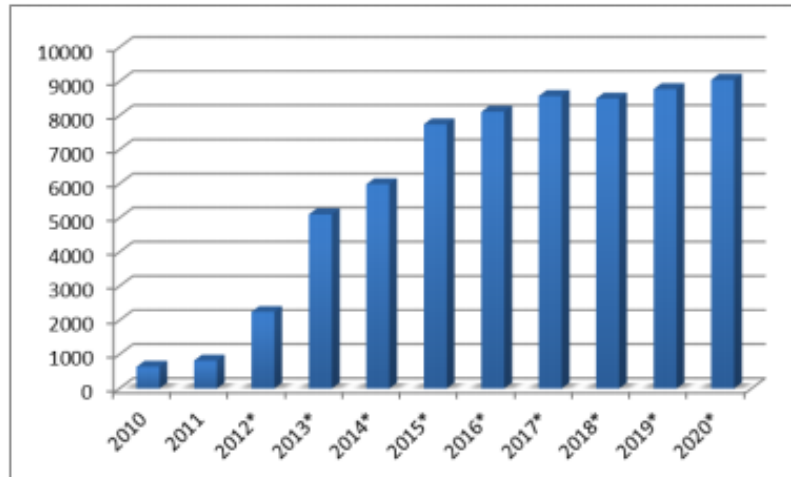
Figure 1.2 Carbon fiber consumption in wide-body aircraft [5]

There has long been a consensus in society that there must be a greater focus on conservation of resources and raw materials. Energy use is one of the key considerations here. The potential of high performance fiber composites in lightweight construction is making an important contribution to increasing energy efficiency and certainly offers many opportunities whether in generating, consuming or storing energy [4].

The durability and long life of carbon fiber composites and its ability to be combined with traditional lightweight materials to form sandwich structures is opening the way to additional fields of application [6].

Over the development of several decades, the concept of advanced composite materials has led to the structural strength with light weight replacing conventional material. Considerable literature is available on the investigation of behavior of laminated composite structures and their failure modes under tension-compression [7], quasi-static load [8] and Impact [9]. However, most of the failure in real world application of laminated composites occur due to mechanical fatigue. In laminated composite structures, fatigue involves different damage mechanisms that result in the degradation of the matrix and the fibers [13].

1.2 Motivation

Various methods of predicting fatigue damage have been developed over a long period since composites have found applications in the modern day world. Pascoe et al. [10] discusses in his recent review paper that various models that have been developed are based on macro-scale behavior of the test specimens. Most previously developed models [11, 12, 13, 14] either predict the total fatigue life based on the gradual reduction of macroscopically observable properties as residual strength or stiffness, or the evolution of actual damage features such as matrix cracking or delamination, and not the actual degradation mechanisms. It is, therefore, critical to study these damage mechanisms on a microscopic level in order to develop a better understanding of these specimens and their damage criteria. In this study, the fracture mechanics based method has been used to study the delamination growth under fatigue loading. An attempt has been made to link the fracture mechanics concepts of stress intensity factor (SIF) and strain energy release rate to these damage mechanisms using Digital Image Correlation (DIC) based on the previous research carried out by Puishys et al. [8, 15].

1.3 Thesis Goals and Scope

The challenges outlined above elucidate that characterizing the mechanical behavior of pre-impregnated composite materials to fabricate advanced composite laminate structures with enhanced mechanical behavior is a non-trivial problem. These composite structures are susceptible to delamination and knowledge of a composite materials resistance to interlaminar fracture under fatigue loads is useful for product development and material selection. It is, therefore, important to establish a relationship of the mixed mode strain energy release rate and the number of cycles to delamination growth, which is independent

of the specimen geometry or the method of loading [16]. Moreover, the behavior of mixed mode loading is also known to depend on the micro mechanisms taking place during delamination growth [13]. These results are useful for establishing design safety factors used in damage tolerance analyses of composite. Since the understanding of crack propagation in unidirectional laminated fiber specimens is a prerequisite to address the more general case of damage in bidirectional fiber reinforced composites, and occurrence of different mechanisms in particle reinforced composites, this research has been restricted to studying damage in unidirectional carbon fiber reinforced composites.

The literature review is presented in subsequent pages, briefly describing the fundamentals of composite material engineering, the most common failure mechanisms involved with them, as well as an introduction to the principles behind Linear Elastic Fracture Mechanics. Also, presented in the literature review are the basic principles behind Digital Image Correlation, and its application for this course of study under section 2.5. Following the discussion of these principles comes the mathematical analysis used for traditional analysis of fracture parameters, followed by a detailed test protocol which shows in depth method for conducting fatigue tests using the Wyoming Test Fixtures MMB apparatus and the DCB apparatus in Chapter 4. Theoretical analysis using traditional methods, crack tip displacement analysis, full field and near field data analysis are presented in the subsequent chapters. Conclusions about the use of DIC for extraction of fatigue damage parameters are made. Lastly, future work and suggested improvements to this course of study finish the thesis.

2 Literature Review

Advanced composite materials have drawn attention of the researcher for over six decades and significant effort has been devoted in designing, developing and implementing concepts of advanced composite laminates. Composite materials are engineered materials made from two primary constituents, which remain separate and distinct within the finished structure, but combine to create a lightweight yet resilient structure. Laminated composites make use of the directional properties of reinforcement, and by stacking several plies in multiple directions a much stronger structure is formed, resistant to stresses in multiple directions. They have been used in several applications like aerospace, marine, automotive, etc.

The present research aims at developing and characterizing a carbon fiber laminate composites under cyclic loading conditions. For this purpose, it is important to develop an understanding and survey the research performed in the relevant areas. The following sections briefly describe the relevant areas pertaining to the present research and the aspects that have been explored. Finally, a summary of the literature review will be presented in section 2.6.

2.1 Composite Laminate

Composite laminates are advanced composite materials with high strength to weight ratio, which utilize the directional properties of reinforcement, stacked to create a much stronger structure. These structures are characterized by high stiffness, high strength, and small thickness which make it resistant to in-plane and lateral loads. The primary constituents remain separate and distinct within the finished structure. The pre-preg can be

made up of glass fiber and epoxy resin. The first material is typically a patterned weave of fibrous material called the reinforcement, usually consisting of extruded glass fibers, carbon fibers, and Kevlar fibers, metal or in some cases ceramic particles. These fibers are then embedded in a much softer matrix. The matrix may vary with the use of select soft metals, epoxy resins, or even ceramics. This course of study, however, focuses explicitly on the use of polymer matrix compositions as they are commonly found in the aerospace industry. The reinforcement material is what gives the composite its high axial strength and other favorable properties, while the matrix serves to transfer the load among the reinforcements, and hold the reinforcement in an orderly and continuous fashion. The reinforcement may vary with orientation with the fibers all in one orientation, known as a unidirectional composite, or in two directions, known as a bidirectional weave. Non-continuous fibers are also used for composite materials, and the reinforcement may vary from short randomly spaced fibers to discrete particles, however, only continuous fibers are investigated in this research program. Composites may also be comprised of numerous discrete fiber orientations; this is most commonly referred to as a laminate. Laminates make use of the directional properties of the reinforcement, and by stacking several plies in multiple directions a much stronger structure is formed, resistant to stresses in multiple directions. Characterization of the stacking sequence is intrinsic to understanding the nature of a particular laminate under investigation. The laminate thickness is another important specification which needs to be controlled to avoid large applied displacements and, therefore, geometric nonlinear errors [17]. This course of study primarily analyzes unidirectional carbon fiber composite laminates.

Composite laminated structures have been used for several applications like aerospace, automotive and several infrastructural applications, as well. Since the engineering of transportation devices, materials with high strength and light weight have been of huge interest. The advanced composite laminated structures have been especially successful and leading material in the aviation industry. Aircraft parts have utilized composite materials in areas such as fairings, spoilers, and flight controls since the 1960s for their weight savings over aluminum parts. Newer and larger aircrafts are designed with all composite fuselage and wing structures and the repair of these advanced composite materials requires an in-depth knowledge of composite structures, materials, and tooling. The primary advantages of composite materials as outlined in the literature are their high strength, relatively low weight, and corrosion resistance [18].
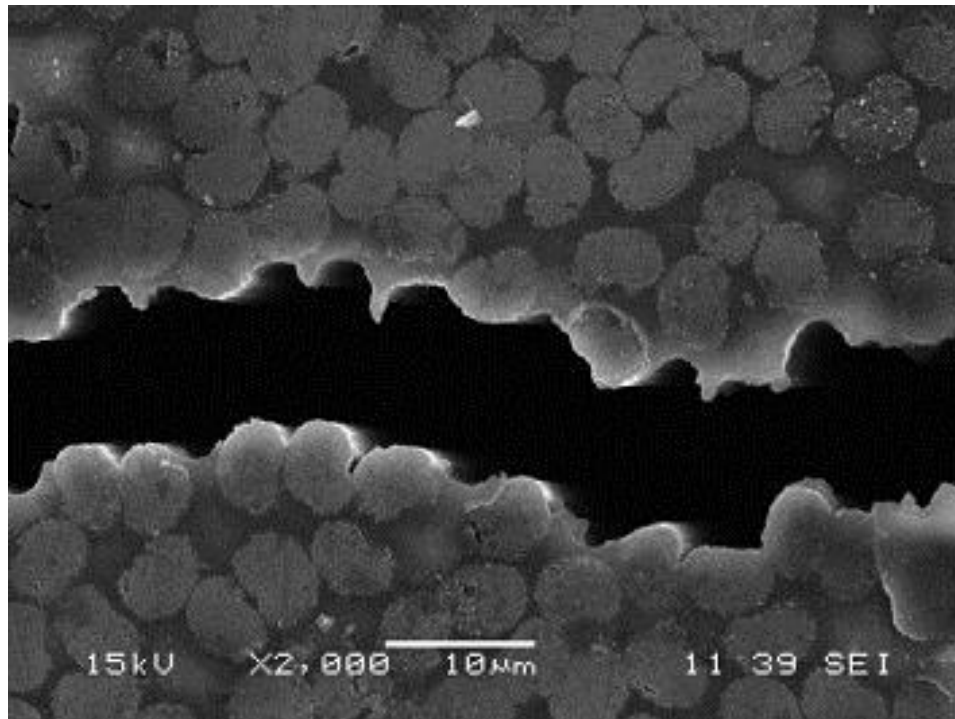
Figure 2.1 SEM showing cross section of fiber and matrix with
transverse tensile failure of unidirectional epoxy composite [19]

2.2 Damage Mechanisms in Carbon Fiber Laminate

Several investigations have been performed to study the failure modes of laminated composites. The failure modes of laminates are typically delamination via fracture, shearing, and fatigue and matrix cracking. Although Composite laminates may be characterized by good strength to weight ratio, they do have significant drawbacks. Unidirectional laminates are weaker particularly when loaded transverse to the fiber direction [8, 20]. This becomes worse when the specimens are loaded in bending. Defects in the composite's matrix, such as voids, contaminants, resin pockets, and ply drop off, combined with defects in the fibers themselves such as broken fibers, fiber slacks, kinks, misalignments, and deboned areas are all issues unique to composite engineering [21]. These defects do not affect the ultimate strength as much; however, the failure mechanisms of composite materials maybe impacted drastically. These problems are unique to composite laminates and differentiate them form homogeneous materials. Although many failure mechanisms are not specifically unique to composites, the propensity for delamination certainly is [8]. *Figure 2.2* shows a catastrophic delamination in F155/PW epoxy laminate.

Figure 2.2 F155/PW laminate after compression test showing "shear failure" [22]

Composite material systems predominantly fail due to the physical failure of the matrix material bonds in the interlaminar failure. Delamination results from the stress concentration in the notch which breaks the cohesive matrix holding together the reinforcement, resulting in separation of layers with a significant loss to the mechanical strength of the laminate. Although it is the engineer's duty to ensure that the composite system is designed to carry the bulk of the load in the fibers, the matrix still proves essential in maintaining the structural integrity of the system, as well as transferring and distributing the load across the entire specimen. Fracture in the matrix, and the subsequent debonding of lamina may not be catastrophic for a composite laminate; however, delamination does reduce structural stiffness, and results in a loss of the system's integrity [8]. As previously stated, delamination is not usually the structural failure, rather the point for further damage to the system. Typical delamination in composite laminates is initiated by compressive loads, something that composites are notoriously poor at withstanding. Buckling and

bending, especially with a large cross- sectional area results in large displacements that are different for each lamina ply [21]. Delamination is a process in the overall failure of a laminate while fracture is the ultimate destruction of the structure [21]. Delamination is closely linked to the primary damage mechanism of fracture and is the main failure mechanism which will be investigated in this course of study.

2.3   Fracture under Fatigue Loading

Fracture is the separation of an object into two or more subsequent pieces. Fracture can occur globally, as is the case for a specimen which has completely parted, or locally as in the case for cracks that propagate across the length of the specimen. Crack propagation and initiation always accompanies fracture of materials; the rate at which it occurs, all depends upon the loading condition as well as material properties. Fracture in homogeneous materials can undergo trans-granular fracture, or inter-granular fracture; however, in composite materials crack propagation is usually limited to the matrix material as it offers the path of least resistances. Matrix materials tend to fail in a brittle manner, and cracks spread rapidly with little or no plastic deformation. Tracking crack growth under unstable conditions becomes an issue [24].

A body that is subjected to repeated loads less than the ultimate failure stress can fracture too. Fatigue failure is one of the most common causes of failure that an engineer comes across [26]. Fatigue failure can occur even under elastic loading. However the primary damage mechanism under cyclic loading is fracture, it is, therefore, necessary to discuss fracture in detail.

Fracture is characterized in one of three basic modes, or a combination of two modes as seen in *Figure 2.3*. The first is Mode I, or opening mode fracture, where load is applied

in tension to separate layers of the material. The second is Mode II, in plane shear, or sliding mode. And the last fracture mode is Mode III, out of plane shear, or tearing mode. Any combination of these three modes of fracture can be referred to as Mixed Mode fracture. The course of this study will be, however, limited to a combination of Mode I (opening) and Mode II (in-plane shear). These tests will be performed using methods developed by William et al. [11,24,25] such as the Double Cantilever Beam (DCB) test, discussed in greater detail later, as well as the Mixed Mode Bending (MMB) method, first developed for use by NASA in 1988 [24].
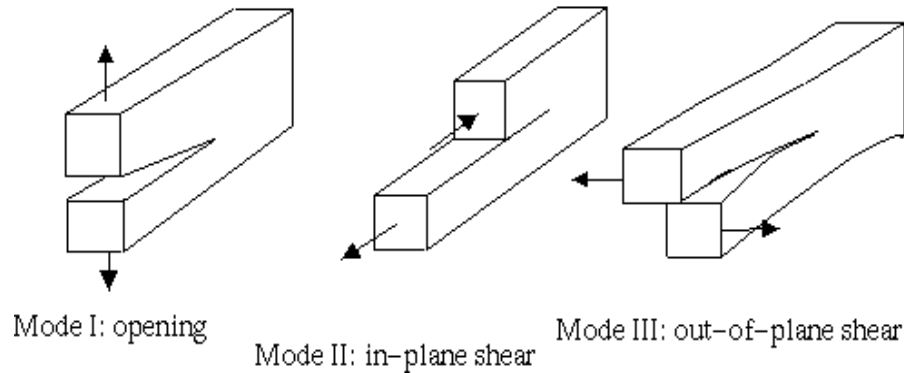
Figure 2.3 Fracture modes [23]

The parameters governing crack propagation under fatigue were first examined by A.A. Griffith. Griffith's criterion for quasi-static loads explains crack propagation with stress intensity factors and by comparing energy stored in the deformed crack tip. This approach can be used to conduct tests and calculate the strain energy release rate, as well as the stress intensity factors directly from test data, material properties, and geometry [26].

The solution for stress intensity factor and stress in homogeneous materials is given by the following equations, which were developed by Tada, Irwin, et al. [27]. For tensile cracks (Mode I):

12

$$K_I = \sigma^\infty \sqrt{\pi a} \tag{2.1}$$

$$\sigma_{22} = \frac{\sigma^\infty x_1}{\sqrt{x_1^2 - a^2}} \tag{2.2}$$

And the solution for shear cracks (Mode II):

$$K_{II} = \tau^\infty \sqrt{\pi a} \tag{2.3}$$

$$\sigma_{12} = \frac{\tau^\infty x_1}{\sqrt{x_1^2 - a^2}} \tag{2.4}$$

Where,

K_I = Stress intensity factor in Mode I

K_{II} = Stress intensity factor in Mode II

σ = Tensile Stress

τ = Shear Stress

a = Half crack length

x_1 = Point of load application in an infinite plate

These equations are, however, valid for homogeneous materials only. The course of this study is based on composite materials, where a number of other effects cause the estimated value for strain energy to be skewed.

Delamination and fracture in composites is usually initiated by higher interlaminar stresses at geometric discontinuities. Priel et al. [28] demonstrated this for brittle elastic V-notched structures. He also showed that mode mixity ratio influences greatly both the failure load and crack initiation angle. These geometric discontinuities are usually in the form of an intentionally implemented delamination insert. These experiments have been previously affirmed with Cohesive Zone Modelling (FEA) and numeric Finite Element

Analysis (FEA) [6, 8, 29]. Although there are a number of methods for improving the determination of material behavior, the use of energy conservation concepts for fracture mechanics in composite materials is most common [7, 8, 11, 17, 21, 25].

In the preceding work, experimental investigation was performed to determine fracture parameters of carbon fiber laminate composites under quasi- static loading [8]. The strain and displacement fields were determined using Digital Image Correlation (DIC). The experimental results were compared with the computational results. The present course of study will extend this work to fatigue testing of carbon fiber composites and studying the delamination characteristics and conditions of loading. The initial tests are based on capturing the varying stress and strain field, as well as other microstructural features in unidirectional carbon fiber specimens similar to the ones used during the previous fracture study using 2D DIC. These details are to be used to enhance existing models by providing critical details and explanations of the crack growth under low & high cycle fatigue.

The linear elastic fracture mechanics (LEFM) solution remains valid for slow crack growth under cyclic loading.

2.4 Crack Tip Displacement Theory

Poursartip et al. [30] investigated the measurement of crack tip displacement fields in composites and focused his analysis on the crack opening as well as crack shear displacement. Global parameters such as load, compliance, and specimen dimensions have been used to infer the localized effects around the crack tip which dominate the crack response but not without facing difficulties. Phenomena like fiber bridging in opening mode loading of delamination, and influence of friction between the surfaces of the delamination crack in shear loading shield the crack tip from seeing the full effect of the

14

far field loads [30]. The ASTM standards used for performing the mixed mode tests [7,17,31] also assume that fiber bridging is negligible, an incorrect assumption, yet experiments have shown its presence under high mode I loading as seen in *Figure 2.4*. An attempt has been made to account for these effects in our research using DIC.

Fiber bridging and multiple crack tip growth
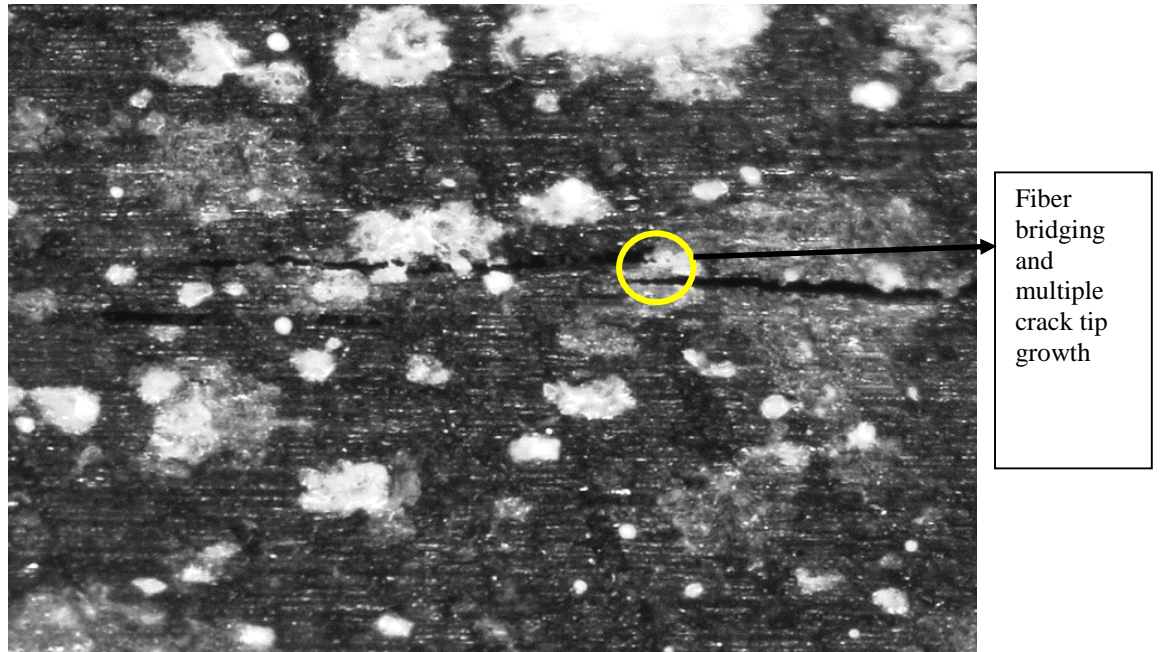
Figure 2.4 Fiber bridging in specimen in 22% mode I cyclic loading at 39 N and 25X

Poursartip [30] suggests that crack tip displacement analysis can account for these anomalies and still provide accurate results with minimal assumptions. The expressions for Crack tip displacement and Crack shear displacement in the crack tip region for rectilinearly orthotropic bodies were developed by Lekhnitskii et al. [32] and Sih et al. [33] and are as follows:

$$COD = \left[4(2)^{1/4} \frac{(a_{11}a_{22})^{1/4}}{\sqrt{\pi}} \left(\frac{2a_{12} + a_{66}}{2a_{11}} + \sqrt{\frac{a_{22}}{a_{11}}} \right)^{1/4} \right] \sqrt{G_I} \sqrt{r} \tag{2.5}$$

$$CSD = \left[4(2)^{\frac{1}{4}} \sqrt{\frac{a_{11}}{r}} \left(\frac{2a_{12} + a_{66}}{2a_{11}} + \sqrt{\frac{a_{22}}{a_{11}}} \right)^{\frac{1}{4}} \right] \sqrt{G_{II}} \sqrt{r} \qquad (2.6)$$

The analytical framework set forth here is the basis for the initial DIC work collected in this research, and along with certain higher order terms added to these equations, can be applied to composite laminate structures. Although Poursartip et al. [30] assumes that these orthotropic materials can be assumed homogeneous as there were no practical analytical alternatives; we have taken the orthotropic nature of fiber reinforced laminates into consideration. They also conclude that the crack tip singularity is of order $r^{-1/2}$, as assumed by LEFM. But the conclusion that "global G (strain energy due to the applied load) is equal to local G (seen in the crack tip region)" is taken otherwise. Our calculations and observations in Chapter 5 show that global G is not equal to local G, suggesting that energy is dissipated in other parts of the specimen due to anomalies like fiber bridging, though it has been difficult to calculate the strain energy in the fiber bridging region due to the limitations of the microscopic resolutions and subsequent DIC analysis on these images.

2.5 Deformation Measurement Using Digital Image Correlation

Digital image correlation is fast emerging due to its versatility and simplicity. It evaluates the displacement fields corresponding to a series of images taken at various instances of loading. In essence, it is an optical non-contact method for tracking and registering discrete changes between two or more images. It may be implemented in 2D (2D-DIC), in 3D (3D-DIC), volumetric digital image correlation (V-DIC) and digital volume correlation (DVC) [34]. The technique was first pioneered by H. Bruck, S. McNeil,

and M. Sutton [35] in the 1980s, and has since been an ideal tool for obtaining accurate displacement measurements at multiple length scales. The author has used 2D-DIC this research. Using DIC programs like Vic-2D by Correlated Solutions, Inc. allows users to quickly measure displacements in a specimen for many different length scales. DIC being length scale independent can be used at the macro to nano-length scales and several time scale measurements with the use of appropriate camera and speckle pattern on the surface.

Haldar et al. [36] used DIC to measure the deformation of palmetto wood specimens during three- point bending under low velocity impact loading to use it as a biological inspiration for impact resistant polymer composites. Hamam et al. [37] studied fatigue crack growth in steel via digital image correlation. Hamam discusses the measurement of stress intensity factor change during one cycle using decomposition of the displacement field onto a tailored set of elastic fields. Mogadpalli et al. [38] applied DIC technique to determine stress intensity factor for cracks in orthotropic composites. DIC is an essential tool because it removes the additional analysis and uncertainty present with the use of strain gauges. Strain gauges, though common, require a complex and meticulous application process and cannot precisely account for the microscopic changes occurring in the specimen. Sometimes, the presence of a strain gauge and the mounting mechanism alters the fracture properties of the specimen being measured. DIC can be used for measuring displacements because of the minimal effort involved in surface preparation, but its scope is limited to surface displacements only, or anywhere a series of images may be captured. Mogadpalli et al. [38] investigated pre-cracked, transversely loaded composites, whereas our research is based on studying delamination in composite laminates. This course of study is much more useful as it investigates a more challenging and common failure

mechanism i.e. fatigue loading. DIC negates the necessity for using compliance correction in the calculation of the material properties. This is helpful in tests like the DCB and MMB, where the compliance of the load frame and testing apparatus must be calculated and accounted for to prevent results from being skewed. Because the measurements in DIC are collected directly from the specimen, there is no need to consider deformations in the loading fixture [8].

Poursartip's [30] assumption that composite specimens are considered homogenous during testing due to lack of analytical alternative, or assumption that fiber bridging and influence of friction between the surfaces is negligible, can now be avoided while using DIC. However, the drawback of DIC is that it requires a relatively stable platform and that the same local area be monitored throughout the tests. Using the DCB test, and MMB test, results in large displacements in some cases, and keeping the camera in focus on the location of the crack tip can become a daunting task. As DIC can be utilized at varying length scales, this enables characterization and comparison of crack propagation at both global and local scales. Although DIC has been previously used accurately to extract fracture parameters of orthotropic materials. And an attempt was made by Puishys et al. [8] to analyze the near field crack tip phenomena common in composite laminates under quasi-static loading, it has been not utilized to understand the behavior of composites under cyclic loading. This research intends to use DIC to capture, analyze and explain unique phenomena in fracture under cyclic fatigue loading of transversely isotropic materials such as carbon fiber laminates.

2.6 Summary

This research was possible because of the significant ground work done that has been used to establish the theories for this research. The use of DIC has helped the author closely understand and characterize the behavior of these laminated composites under cyclic loading conditions. DIC is the ideal tool for characterizing fracture at multiple length scales will neglecting the common assumptions required for analysis in the past. Mixed mode bending tests have been previously performed on carbon fiber laminate composites with varying levels of success. An attempt has been made to utilize the potentials of a non-contact full field optical technique, DIC in determining crack tip fields under cyclic load. The ASTM method based on a global response of the specimen is complimented with the direct full field deformation measurement of on the specimen surface using DIC. DIC has been used to characterize these laminated specimens under mixed mode cyclic loading in the region near the crack tip using optical microscopy. This research establishes a means of accurately characterizing failure mechanism for laminated composite materials on a microscopic level and comparing the results with macroscopically acquired data.

3 Experimental Technique for Mechanical Characterization of Fatigue Fracture

Pre-existing experimental methodology has been used to characterize the mechanical behavior of the carbon fiber laminate composites at multiple length scales based on optical characterization of the deformation. The carbon fiber laminate specimens under study have been deformed under quasi-static [8,17], and cyclic loading in mixed mode bending [7,17], Double cantilever beam [7] and three-point bend configuration [12] and the mechanical properties have been quantified.

3.1 Test Protocol Used

ASTM D6115-97. "Standard Test Method for Mode I Fatigue Delamination Growth Onset of Unidirectional Fiber- Reinforced Polymer Matrix Composites" [7] and ASTM D6671/D6671M-06. "Standard Test Method for Mixed Mode I-Mode II Interlaminar Fracture Toughness of Unidirectional Fiber Reinforced Polymer Matrix Composites" [17]. These tests were performed using the Double Cantilever Beam specimen and Wyoming Test Fixture, MMB-35 with end-notch-flexure (ENF) specimen respectively, as shown in *Figure 3.1, Figure 3.2* and *Figure 3.3*.
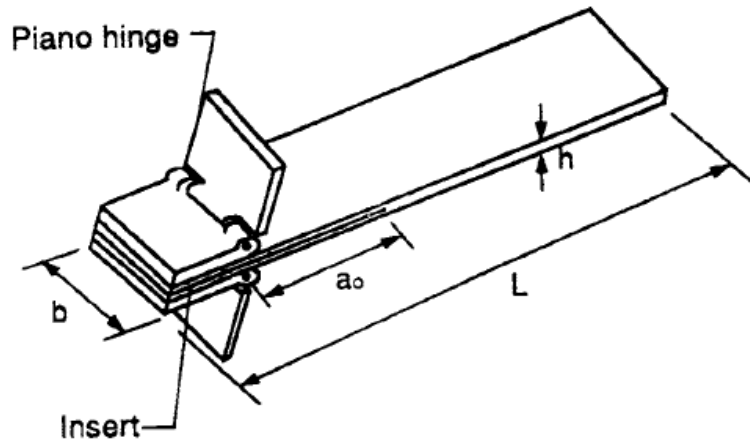
Figure 3.1 Double Cantilever Beam Specimen with Piano hinges [7]
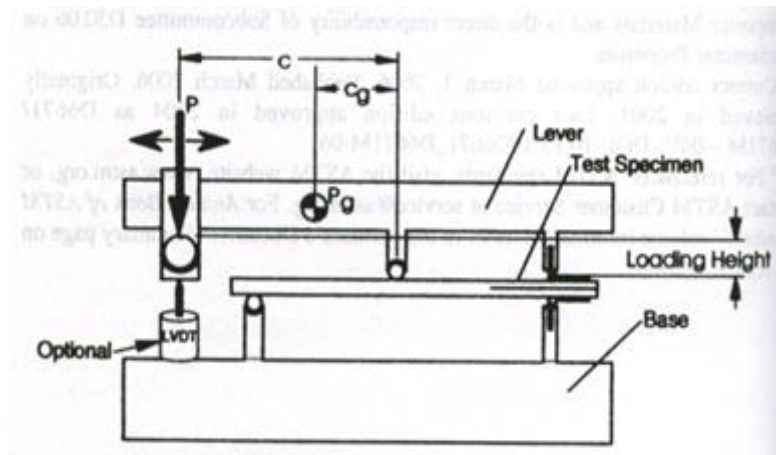
Figure 3.2 Mixed Mode Bending Fixture with a loaded specimen [17]
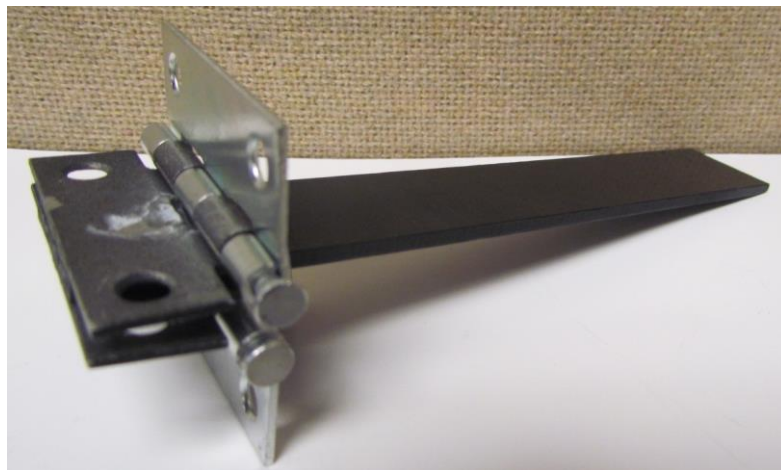
Figure 3.3 Tested specimen with hinges

3.2 Definitions

Mode I strain energy release rate: G_I "The loss of strain energy associated with Mode I deformation in the test specimen per unit of specimen width for an infinitesimal increase in delamination length, da" [17]

Mode II strain energy release rate: G_{II} "The loss of strain energy associated with Mode II deformation in the test specimen per unit of specimen width for an infinitesimal increase in delamination length, da" [17]

Strain Energy Release Rate: G, The total shear fracture toughness, maybe calculated by the sum of G_I, the mode I component, and G_{II}, the mode II component.

3.3 Nomenclature

This section defines the nomenclature used for the tests. These are as follows:

a: Crack Length

a_o: Initial Delamination Length (measured from the loading tab)

b: Specimen width

c: Lever arm length for MMB apparatus

c_g: Lever arm length to center of gravity

h: half thickness of specimen

L: Half Span Length of MMB apparatus

m: Slope of Load Displacement Curve

V: Fiber Volume Fraction

β: Non-dimensional Crack Length Correction Parameter

x: Crack length Correction parameter

P: applied load

P_g: Weight of Lever and Attached Apparatus

P_{nl}: Critical Load at Nonlinear Point of Curve

P_{tab}: load on the loading tab

P_{vis}: Critical Observed Load

d: Load point deflection

C: Compliance

CV: Coefficient of Variation

E_{11}: Longitudinal Modulus of Elasticity

E_{22}: Transverse Modulus of Elasticity

G_{12}: Shear Modulus (out of plane and in plane)

G: Total Strain Energy Release Rate

G_I: Strain Energy Release Rate (Mode I)

G_{II}: Strain Energy Release Rate (Mode II)

G_c: Total Mixed Mode Fracture Toughness

$\dfrac{G_{II}}{G}$: Mode Mixture

$\Gamma = 1.18 \dfrac{\sqrt{E_{11}E_{22}}}{G_{13}}$: Transverse Modulus Correction Parameter

$\chi = \sqrt{\dfrac{E_{11}}{11G_{13}}\left[3 - 2\left(\dfrac{\Gamma}{1+\Gamma}\right)^2\right]}$: Crack Length Correction Parameter

3.4 Identification of Specimen for Testing

The specimens used for this study are unidirectional as ASTM Standard D6671 is limited to use with zero degree ply lay-up. Secondly, it is easier to analyze unidirectional specimens in the course of this study and account for crack shielding effects like fiber bridging. Because this technique will be used with DIC, restrictions on use of the global conditions for obtaining the localized mixed-mode fracture conditions with this standard can be obviated. Though the ASTM standard equations will be used for a baseline result for comparison, much more accurate means of calculating local fracture parameters will be achieved, negating the necessity to use only unidirectional samples. Despite these extenuating circumstances, several material assumptions present in the analysis used to calculate task critical parameters are: (1) a brittle and tough single phase polymer matrix must be used, (2) reinforcement must be long and continuous, and (3) delamination must be initiated with an insert. Linear Elastic Fracture Mechanics (LEFM) behavior is assumed in the calculation of fracture toughness for the ASTM standard, but as indicated previously is not necessarily an assumption with the use of DIC for localized displacement field measurements near the crack tip. Typically, this assumption would be valid only if the damage zone, where ideally minimal plastic deformation is present at the crack tip propagation, is small relative to the specimen thickness. This is consistent with the assumption that a brittle polymer matrix is used. Another requirement of successful use of the Wyoming Test Fixture is that displacements are kept to acceptable values. The following equations with estimated critical load, and estimated load point of deflection may be used to determine the specimen thickness to achieve permissible amounts of displacement:

$$\delta^{est} = \frac{p^{est}}{8bE_{11}h^3L^2}\left[4(3c-L)^2(a+h\chi)^3 + (c+L)^2\left(2L^3 + 3(a+0.42h\chi)^3\right)\right] \quad (3.1)$$

$$p^{est} = \sqrt{\frac{\dfrac{3}{4}G_c^{est}b^2E_{11}h^3L^2}{(3c-L)^2(a+h\chi)^2 + \dfrac{3}{4}(c+L)^2(a+0.42h\chi)^2}} \quad (3.2)$$

The specifications for these specimens were kept similar to the ones used previously in the study involving the fracture parameters [8]. Using these equations, specimens were manufactured to have 24 plies, resulting in a nominal manufactured thickness of 3.14 mm with a variation of no more than .1 mm. Specimens which were outside the acceptable parameters were rejected and subsequently not used for testing. The carbon fiber laminate structures used as specimens for this study were fabricated in large quantities throughout the course of this study. This was done in order to test multiple samples under similar loading conditions. This process has helped during the research to discover ways to conduct unsuccessfully, learn from them and invalidate any discrepancies that might result in other tests.

3.5 Preparation of Laminated Composite Specimen

A unidirectional pre-impregnated carbon fiber tape from *Composites Store, Inc.* was used as the material for fabricating the specimens. The specifications are as follows:

Carbon Fiber	X534-SR-150/35 with 580 ksi tensile strength
Matrix material	Aldila AR250 with 11.4 ksi tensile strength and 35% by volume

Table 3.1 Properties of the Carbon fiber and matrix material

These standard modulus fibers were found to be similar to the AS4 fibers used commonly in industry. Aldila AR250 resin system is the matrix material in this pre-preg

tape. AR250 is 99.5% solids and ideal for low outgassing applications. AR250 resin is a phenol novolac epoxy which is very similar to bisphenol F. This resin system has a specific gravity of 1.2 g/cc, a tensile modulus of 450 ksi, and a flexural strength of 17 ksi. The overall composite used has 150 grams of resin per square meter fiber, resulting in a nominally 35% by volume resin content. The aerial weight is 150 gm.

Care was taken to preserve the pre-preg tape in order to increase its shelf life and prevent the resin from curing though heat is used to speed up the process. The tape was stored at 0° C in a freezer until it was cut into smaller pieces for fabrication. All the samples used for testing were fabricated within the first 6 months of the research in order to maintain uniformity and prevent degradation of performance within the uncured resin which occurs over time.

As discussed in the section above, the specimens have a mean thickness of 3.14mm. 24 plies of the pre-preg tape were used to achieve the required thickness and stiffness values after curing. The tape was cut into 6" X 6" square sheets and then laid up in 0° orientation to ensure that crack propagation was consistent for all the fibers. A non-adhesive 13 μm Teflon (2" X 6") was inserted in the mid-plane (12th and 13th layer) of the pre-cut tapes starting from one end of the tapes. This film formed the initiation site for the delamination [17].

The 24 ply square laminate was then wrapped in a thick Teflon sheet to protect it from contamination during curing. The lay-up was placed between two aluminum plates and compressed to 2000lbs using a hydraulic press. The setup was then securely clamped and placed in a vacuum oven to follow the temperature cycle given below:
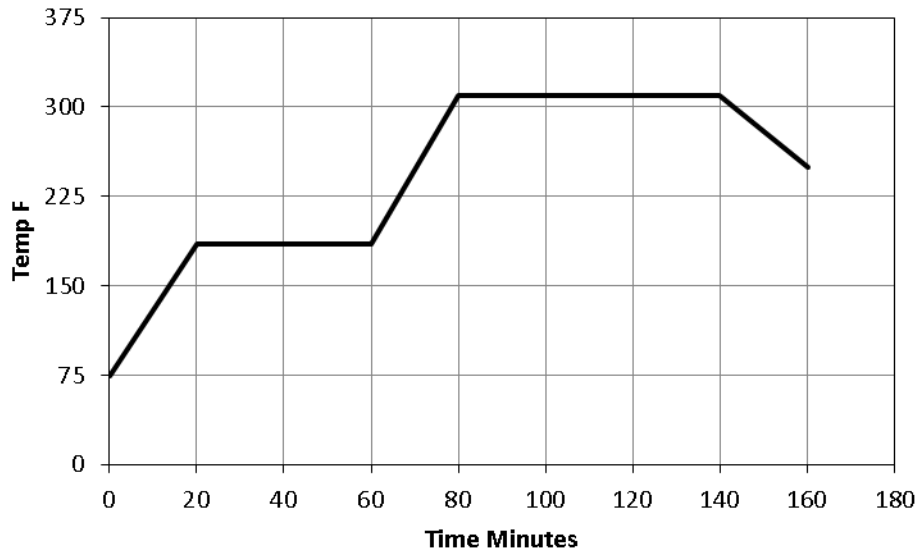
Figure 3.4 Curing cycle for the specimens

Once cured the composite plate is removed from the vacuum oven and carefully cut into the long specimens measuring 6" X 1" X 0.134" (152.4 mm * 25.4 mm * 3.14mm).The exact dimensions of the specimen are not critical for testing as long as careful measurements are made before each test in order to be thoroughly redundant in the experiments. The thickness of the specimen may need to be increased to avoid large applied displacements and, therefore, geometric nonlinear errors [17] as described in Equation (3.1) and (3.2). The cleaning and sanding of the edges effectively gave 5 good specimens from each batch of laminate plate prepared. The ends of the specimen were made rough to apply the loading tabs. The tabs were applied such that the initial delamination length from the loading line to the end of the insert was between 0.45L<a<L-3h. The tabs were adhesively bonded using cyano-acrylate glue and cured at room temperature.

The cured samples are then spray painted with a speckle pattern for DIC. The type of the speckle pattern depends on the magnification level required for analyzing the specimens. The traditional speckle pattern used for DIC, and the one used during the

previous research had a black coating with a fine, random white speckle pattern sprayed

on it, as seen in *Figure 3.5 (a), (b)*. But we found out that, at higher magnification levels

of order of (8X-10X) 0.5-1 micron a plain black coating resulted in better correlation when

analyzed in VIC 2D. This is primarily because, at these magnification levels the white

speckles look like big blobs and become saturated at high light intensity required at these

magnification levels. The black pattern on the other hand looks like a micro speckle pattern

due the fibers and the matrix texture. The plain black pattern is illustrated in *Figure 3.5 (c)*.
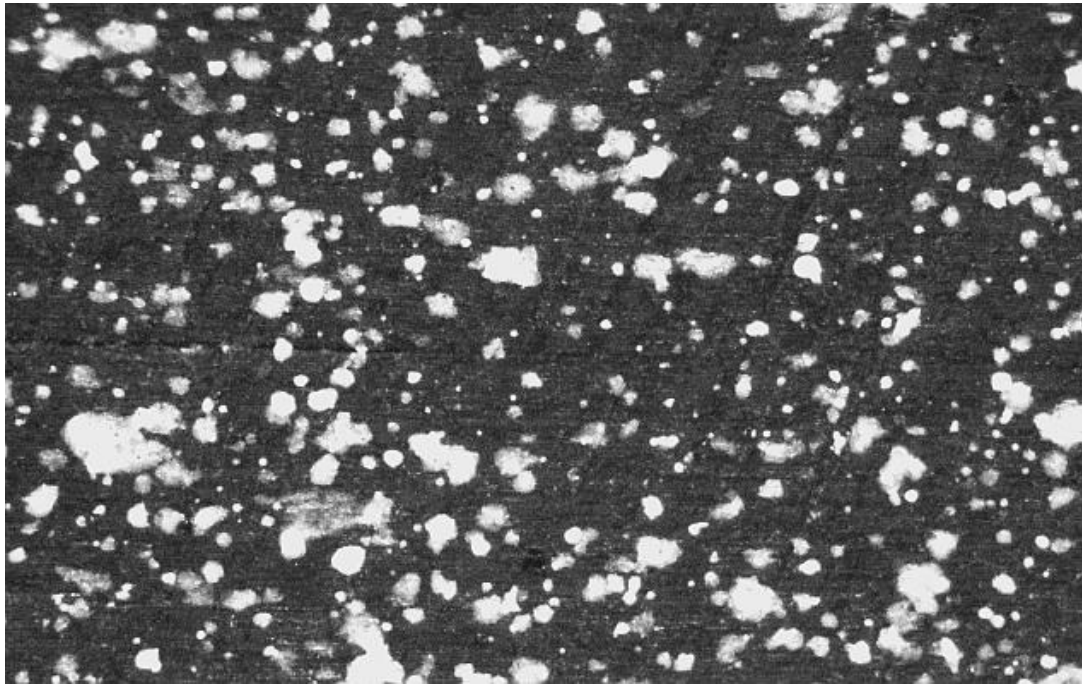
(a) Traditional speckle pattern at 25 X

Index: 39   Pixels: 549
                        (0.1 %)
Total pixels: 888930   Average: 112.85
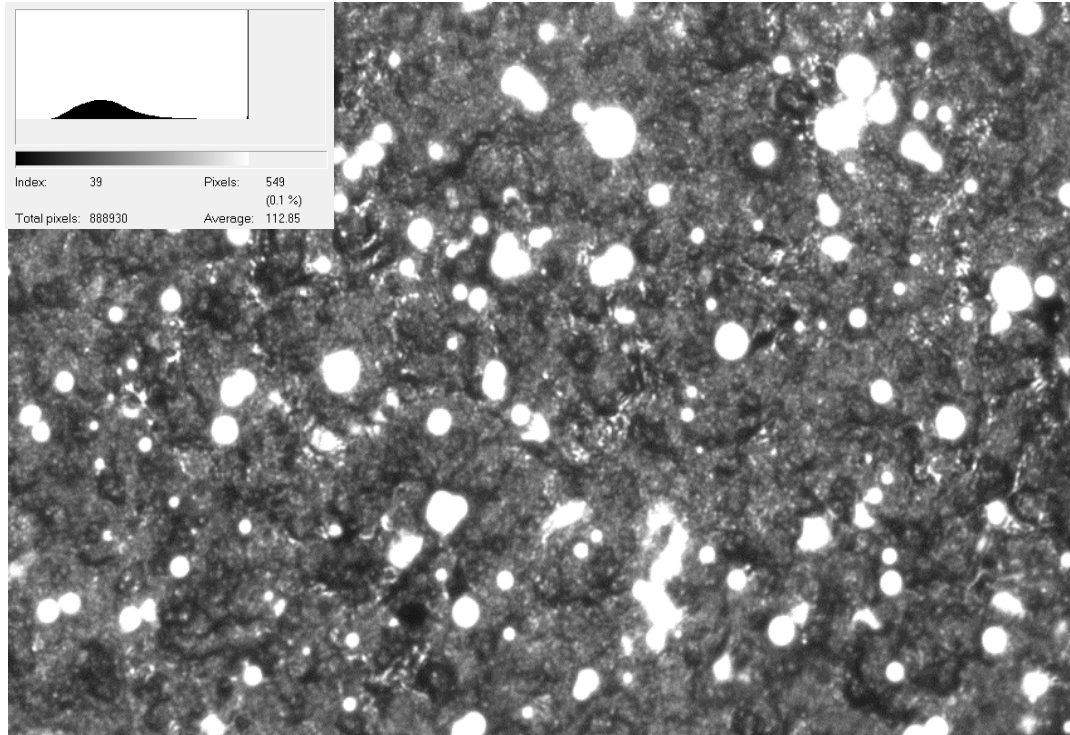
(b) Saturated image showing speckle at 50 X

Index: Pixels:
Total pixels: 581970   Average: 133.45
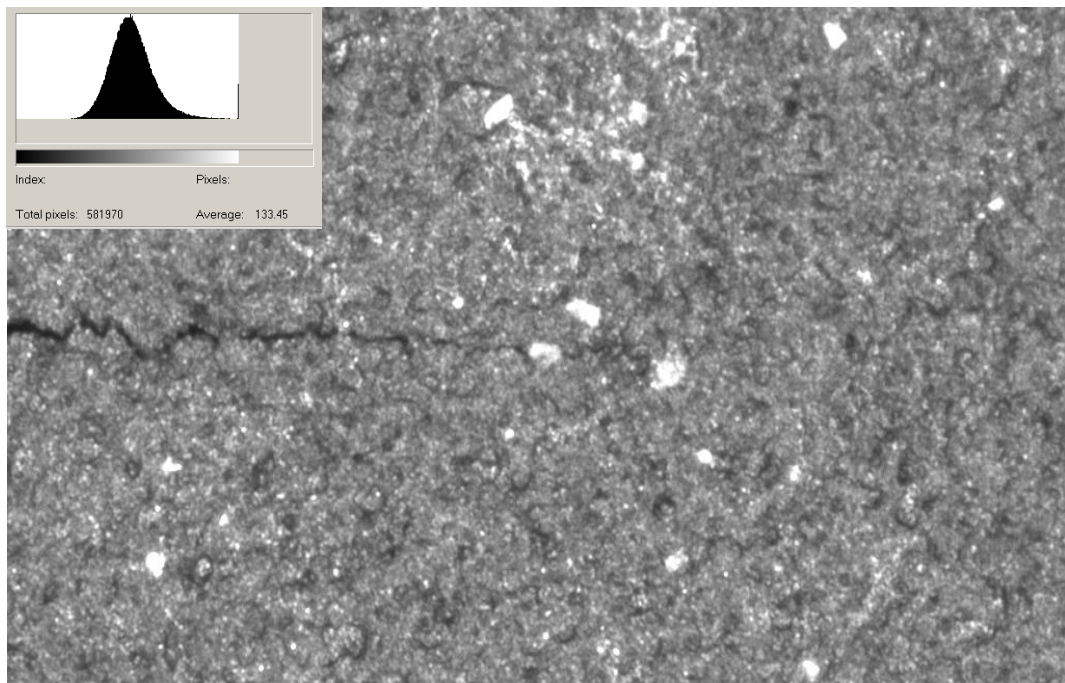
(c) Black pattern in gray scale at 50 X

Figure 3.5 Various speckle patterns used for DIC

3.6 Determination of Material Properties of Unidirectional Carbon Fiber Laminate

Linear Elastic Fracture Mechanics (LEFM) theory has been assumed to be true for the experimental characterization of mixed mode bending and this required us to determine the transversely isotropic elastic properties of the specimen under consideration. Although these properties are available in the literature for the given matrix and carbon fibers [24, 25,15] and also reported in the preceding research involving similar specimen [8], it is a good practice to verify the validity of these values for consistency. These values were calculated using the *WinTest* test program provided with the *Bose ElectroForce 3330* load frame under 4 point bend. These were also compared with specimens tested under 3 point bend test, and theoretical calculations were done on the data from these tests to obtain the material properties.
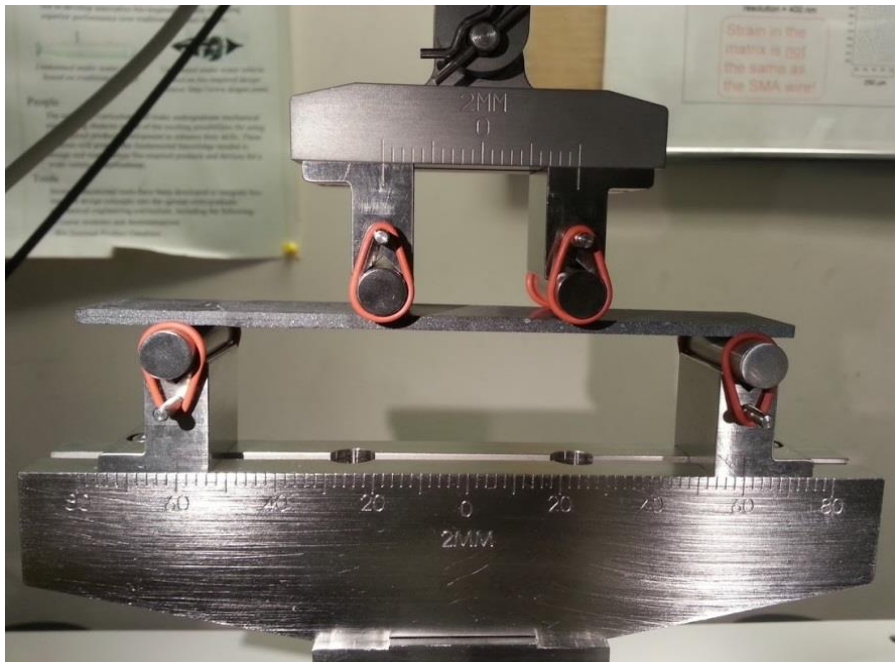
Figure 3.6: The Carbon fiber laminate specimen in the 4 point bend fixture testing

the modulus in longitudinal direction

In order to test the specimens under longitudinal and transverse loading, two different samples were used which could adapt to the 3 point and 4 point fixtures available during the research. The specifications of these samples are given in *Table 3.2*. The load displacement plots of the tests performed on these specimens are shown in *Figure 3.7*.

	Longitudinal direction	Transverse direction
Thickness (d)	3.41 mm	1.38 mm
Width (w)	24.90 mm	22.49 mm
Support Span (L)	120 mm	64 mm
Load Span	40 mm	20 mm

Table 3.2 Specifications of the samples to be tested for material properties
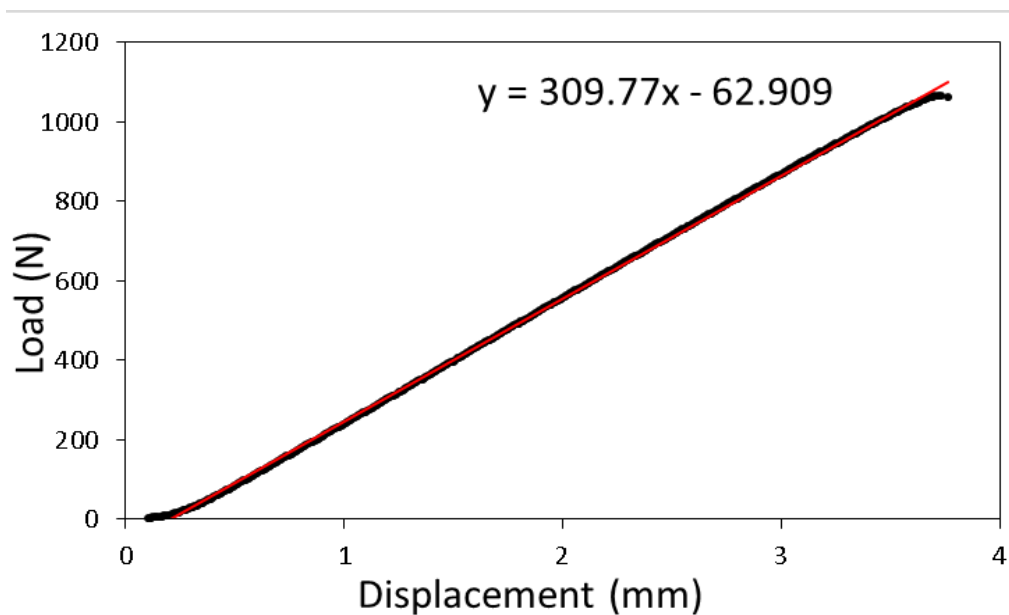
(a) Load Displacement plot in longitudinal direction of fiber

$y = 9.7995x - 0.0539$
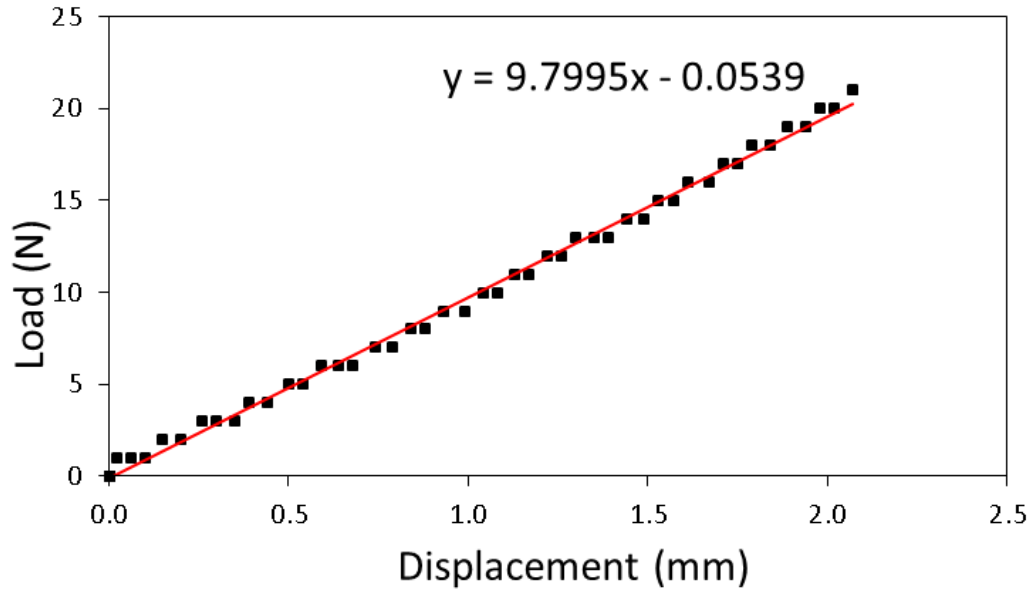
(b) Load Displacement plot in transverse direction of fiber

Figure 3.7 Load Displacement respnse for (a) Longitudinal (b) Transversely loaded

specimen

Equation (3.3) was used to calculate the young's modulus in the (E_{11}) longitudinal

and (E_{22}) transverse directions. Results can be seen in *Table 3.3*,

$$E = \frac{L^3}{4wd^3} * m \tag{3.3}$$

Where,

m is the slope of the load displacement curve.

E_1	Axial Stiffness	135.55 GPa
E_2	Transverse Stiffness	10.86 GPa
G_{12}	In Plane Shear Stiffness	5.9 GPa
v_{12}	Major Poisson's Ratio	0.3
v_{21}	Minor Poisson's Ratio	0.024

Table 3.3 Material Properties of Unidirectional Carbon Fiber Laminate

The elastic constant for transversely isotropic materials are defined as follows [39]:

$$\begin{bmatrix} \varepsilon_1 \\ \varepsilon_2 \\ \gamma_{12} \end{bmatrix} = \begin{bmatrix} S_{11} & S_{12} & 0 \\ S_{12} & S_{22} & 0 \\ 0 & 0 & S_{66} \end{bmatrix} * \begin{bmatrix} \sigma_1 \\ \sigma_2 \\ \tau_{12} \end{bmatrix} \tag{3.4}$$

where,

$$S_{11} = \frac{1}{E_1}$$

$$S_{12} = \frac{-\nu_{12}}{E_1} = \frac{-\nu_{21}}{E_2}$$

$$S_{22} = \frac{1}{E_2}$$

$$S_{66} = \frac{1}{G_{12}}$$

$$S_{ij} = \begin{bmatrix} 7.38E-06 & -2.21E-06 & 0 \\ -2.21E-06 & 9.71E-05 & 0 \\ 0 & 0 & 1.69E-04 \end{bmatrix} \tag{3.5}$$

These parameters are used in the full field DIC fit solutions discussed in Chapter 5.

3.7 Determination of Mode Mixity and Strain Energy Release Rate from Global Response

As mentioned before, the tests methods have been primarily divided into 3 parts depending on the mode mixity:

1. Mode I test: 0% Conducted using DCB specimen

2. Mixed Mode (I and II): 22%, 50% using WTF MMB-35 fixture

3. Mode II test: 100% using WTF MMB-35 fixture in 3 point bend configuration

The test requires the use of a fully calibrated test specimen. Strict adherence to the ASTM standard D6671/6671M is a good start at ensuring minimal disturbances in the successful

implementation of this test procedure. Calibration was carried out using an un-cracked Aluminum specimen having dimensions similar to the test specimen. The load displacement data for the calibration specimen was recorded for area before plastic deformation set in the aluminum specimen.

The experiments have been carried out at 0% mode mixity (Pure mode I), 22% mode mixity, 50% mode mixity and 100% mode mixity (Pure mode II). Pure mode I testing was done using the double cantilever beam specimen (DCB). Wyoming test fixture was can be used to vary the mode mixity between 22% and 100% due to the maximum possible lever length c limited to 96 mm. Due to the nature of the experiments there is a narrow range for which data may be acquired using high power microscopes and DIC.

In order to be comprehensive in the course of my study, pure mode I testing was necessary. *Figure 3.8* shows a DCB setup with a specimen with an insert ready for testing. This enables us to track a stable and consistent crack growth in the laminated composite.
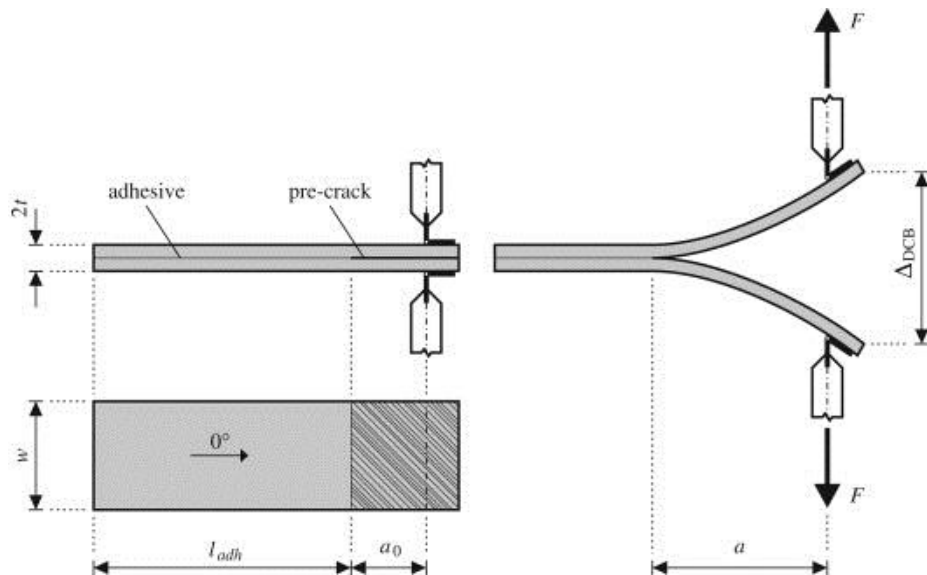
Figure 3.8 Schematic for DCB test [44]

The compliance of the DCB specimen is calculated as:

$$C = \frac{\delta}{P} = \frac{2a^2}{3E_{1f}I}$$ (3.6)

The global strain energy release rate, G, is only a function of G_I as G_{II} is 0 for a DCB test. Therefore G is given by:

$$G = \frac{P^2}{2w} \frac{dC}{da}$$ (3.7)

Equation (3.6) and (3.7) give:

$$G = \frac{P^2 a^2}{wE_{1f}I}$$ (3.8)

The change in G with respect to crack length must be negative for stable crack growth [26]. All other geometric relations are assumed to be similar to Mixed Mode Bending test as defined by ASTM D6671/D6671M. The specimens were processed similarly, and the output data collected consistently between various mode mixtures.

Due to the multi-scale nature of this research, different methods of calculating the global and local characteristics have been used through the extent of this research. The global conditions were calculated based on the ASTM standard D6671/D6671M [17], which requires accounting for the compliance of the testing fixture, the load frame and the hinges which transfer the load to the specimen. The tests conducted at global measurements along the full length of the test specimen accounted for the energy based mixed mode analysis using LEFM. On the other hand, the data accrued using DIC was collected directly from the specimen and no compliance correction was necessary for the displacement. Therefore, in order to account for the data collected directly from the load frame where, crosshead displacement is to be used for the load point displacement, a calibration specimen of known

modulus was first tested in the MMB fixture under quasi-static loading. The system was recalibrated every time the setup (mode mixity) was changed. For this purpose, an aluminum specimen with similar dimensions and Elastic modulus of 70 GPa was used. The specimen was prepared for a test similar to the carbon fiber epoxy specimens with the loading tabs attached at the ends. The test is run until the aluminum specimen reaches the yield point or 75% of the estimated load for the delamination tests to be performed [17]. Aluminum was chosen as the material for calibration specimen as it is homogeneous and isotropic with a known modulus. The compliance is calculated using the following equation [17]:

$$C_{cal} = \frac{2L(c+L)^2}{E_{cal}b_{cal}t^3} \tag{3.9}$$

$$C_{sys} = \frac{1}{m_{cal}} - C_{cal} \tag{3.10}$$

Where:

b_{cal} = width of calibration specimen, mm [in.],

C_{cal} = compliance of calibration specimen, d/P, mm/N [in./lbf],

E_{cal} = modulus of the calibration bar (published value), Mpa [psi], and

t = thickness of the calibration specimen, mm [in.]

m_{cal} = slope of the calibration curve, P/d, N/mm [lbf/in.], and

C_{sys} = system compliance, d/P, mm/N [in./lbf]

The compliance of the MMB loading system must be determined at each setting of lever length, c, to be used. The load is introduced at a constant rate of 0.5 mm/min. The data recorded for the calibration test should be load-displacement data at the crosshead of

the load frame. This information is collected for all subsequent tests and is not limited to the calibration tests.

Mode mixity of the test specimen is determined from the geometry of the fixture. The position of the saddle and the effective length of the loading tab from the saddle is represented by ' c '. Varying the length c from one end to the other can change the mode mixity by altering the geometry of the test fixture. Maximum lever length c = 96 mm leads to a high mode I mixture with mixity around 22% and by reducing the length c to about 20 mm, the specimen is loaded in pure 3 point bending, resulting in pure mode II.

The load-displacement data recorded from the loading cycles is used to measure the slope of the linear elastic region of the load- displacement, the geometric properties and the change in compliance of the system. The stiffness of the laminate, E_{1f} over the duration of the test is calculated using the following equation [17]:

$$E_{1f} = \frac{8(a_o + \chi h)^3 (3c - L)^2 + [6(a_o + 0.42\chi h)^3 + 4L^3](c + L)^2}{16L^2 bh^3 \left(\dfrac{1}{m} - C_{sys} \right)}$$
(3.11)

Where:

E_{1f} = modulus of elasticity in the fiber direction measured in flexure, Mpa [psi]

a_o = initial delamination length, mm [in.], and

m = slope of the load displacement curve, N/mm [lbf/in.]

The value of E_{1f} changes as the crack grows over time and compliance of the system, C_{sys} changes but if the change is found to be small, it is neglected and we assume a constant elastic modulus for the duration of the test. Care should be taken to keep the displacement to a minimum in order to avoid geometric nonlinear errors and in keeping it

consistent with the assumptions of LEFM. The strain energy release rate at any load and number of cycles can be determined using the following equations. These equations rely on delamination length corrections [40, 41, 42] for laminate rotation at the delamination front which also agrees well with finite element analysis [43].

The Mode I component of the strain energy release rate in [kJ/m^2] is given by:

$$G_I = \frac{12P^2(3c-L)^2}{16b^2h^3L^2E_{1f}}(a+\chi h)^2$$

(3.12)

The Mode II component of the strain energy release rate in [kJ/m^2] is given by:

$$G_{II} = \frac{9P^2(c+L)^2}{16b^2h^3L^2E_{1f}}(a+0.42\chi h)^2$$

(3.13)

Total mixed mode strain energy, G is given by the sum of G_I and G_{II}, and the mode mixture is defined here as the percent of the total strain energy release rate that is mode I:

$$\frac{G_I}{G} = \frac{G_I}{G_I+G_{II}}$$

(3.14)

These aforementioned theoretical calculations are able to predict strain energy release rate, and even shear fracture toughness for a specimen at various load levels with a known load displacement curve and crack geometry. This LEFM analysis combined with other more specific local characterization of fracture parameters is important for an accurate determination of composite laminate material failure. A more enhanced understanding of these state of the art materials is required for their successful widespread implementation [8].

4 Application of Digital Image Correlation for Fatigue Fracture Characterization

The present chapter discusses the application of Digital Image Correlation in the characterization of fatigue fracture of carbon fiber laminates. Using optical imaging of the specimen surface at different magnifications, it was possible to identify the deformation fields around the crack tip and features like fiber bridging behind the crack tip.

As mentioned earlier, an important aspect of this research is to utilize DIC to track crack growth and characterize the mechanical properties of the composite specimen. In order to use DIC it is important to have a very good speckle pattern, and some of the patterns used during this study have been discussed in the section 3.5.

The images for DIC were taken using a 1.3 MP camera (Model: FL2G-13S2M-C, Make: Point Grey) attached to a travelling microscope from obtained from Edmund Optics. The image resolution was set to 1280 x 960 Pixels which give an approximate scale of 630 Pixel/mm at 25 X magnification. This scale will prove helpful later during the calculations involving the strain energy release rate from the data extracted from DIC.

4.1 Preliminary Identification of Crack Tip Induced by Insert

Once the imaging setup and the testing fixture are in place and calibrated, the test may be started. The tests have been carried out under both load control as well as displacement control. The initial tests were carried out on the IMADA MX-500 load frame under displacement control. The load displacement data was directly recorded from the load frame and is instrumental in determining the LEFM parameters for the samples. For the low cycle fatigue tests (up to 2000 cycles), this data was recorded non-stop for the entire

duration of the test to record any changes in the compliance of the specimen. For high cycle fatigue tests (up to 30000 cycles), the load displacement data was recorded every 500 cycles to record any considerable change in the compliance.

The specimen were pre-cracked using a 13 μm Teflon insert extending to about 2" from one end of the specimen. These specimens were then preloaded and cycled for about 100 cycles at 70%-80% of the maximum load to eliminate any doubts about the crack growing from the Teflon insert tip instead of natural fatigue crack growth. In order to characterize the composite specimen properly, it is necessary to capture the near field region close to the crack tip closely, and provide a reasonable amount of area for crack propagation to occur [8]. The crack tip was placed about ¼ the total length of the image from one end so that considerable crack growth could be captured in the images without having to adjust the microscope during the test. The images were taken in such a manner so that the crack grew from left to right.

It has been discussed previously in the literature that the visible location of the crack tip may not be the same as the true location of the crack tip [8, 45]. This also results in failing to gauge the correct crack length. This is primarily due to the fact that the visually observed tip of the delamination on the edge of the specimen is operator dependent, even if a travelling microscope is used. The crack growth on the edge of the laminated composite is different than what was observed after the completion of the test, when the specimens were pried open. One method that was implemented to corroborate the visual observation was based on a measurement of the flexural modulus of the specimen and then calculating the crack length from the change in compliance as discussed by Brunner et al. [46] and in the

ASTM standard D5528-13 [47]. This was used to calibrate the visually observed crack length to be used as the effective crack length 'a'.

4.2 Microscopy and Deformation Measurement

Once the crack tip has been located, it needs to be ensured that the frame of reference does not move during the duration of the test as this is a prerequisite for image correlation. The first image is taken at the minimum load which serves as the reference image for correlation. In case the crack tip grows past the frame of reference, a new frame of reference is chosen with a new reference image at minimum load/ displacement depending on the type of test.

In order to keep the frame of reference stationary during the test, three to four large speckles above and below the crack are outlined and marked on the computer monitor. As the specimen displaces and deforms during the test, the microscope can be adjusted to ensure that the marks on the monitor always align with the unique speckles. The encircled speckles in *Figure 4.1* indicate good features to use as reference speckles. As load is applied to the test fixture, images are taken at the maximum load/ displacement over a number of cycles till the completion of the test. These images help in obtaining the data from post processing via DIC. Each test is different, but approximately 10-50 images are taken for every test at intervals varying between 100 cycles to 2000 cycles, depending on the total number of cycles and the mode mixity. Care is taken to keep the loading rate constant.
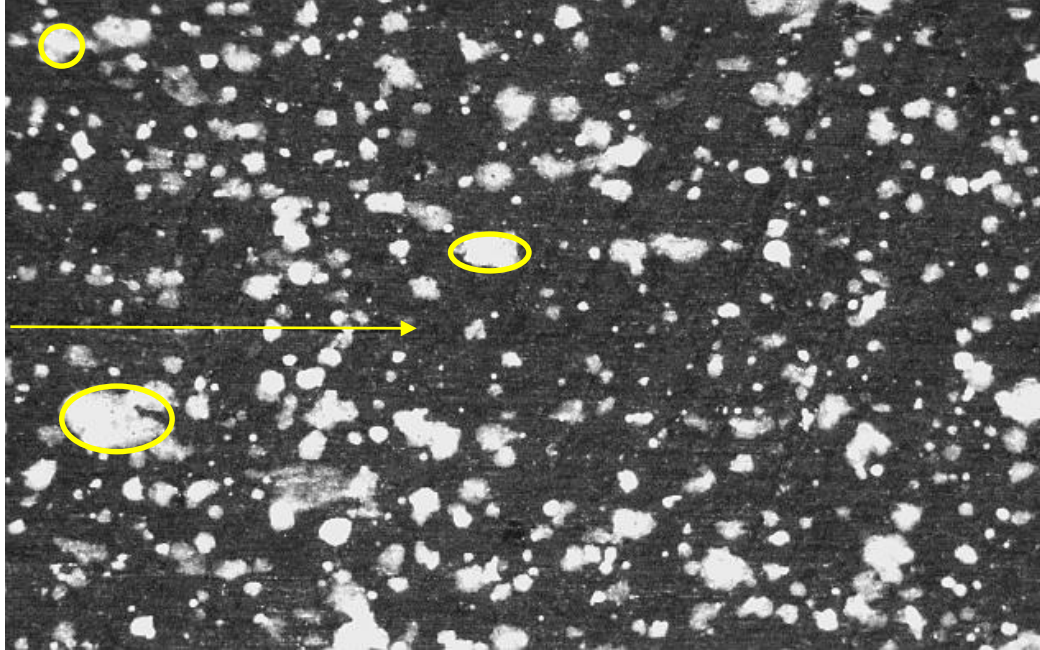
Figure 4.1 Image showing reference speckles and the crack

For the high cycle fatigue tests, it was found that the crack growth rate was much easier and convenient to track with visually determined delamination length increasing in set increments of 0.5 mm and noting the corresponding number of loading cycles completed. In order to do this, the imaged edge of the specimen was marked with lines at intervals of 0.5 mm to 1 mm using an exacter knife as shown in *Figure 4.2*. As the crack grew by a set amount, image was taken, and the number of cycles noted. This was done so that the human error involved in noting the visually observed crack length growth could be reduced.
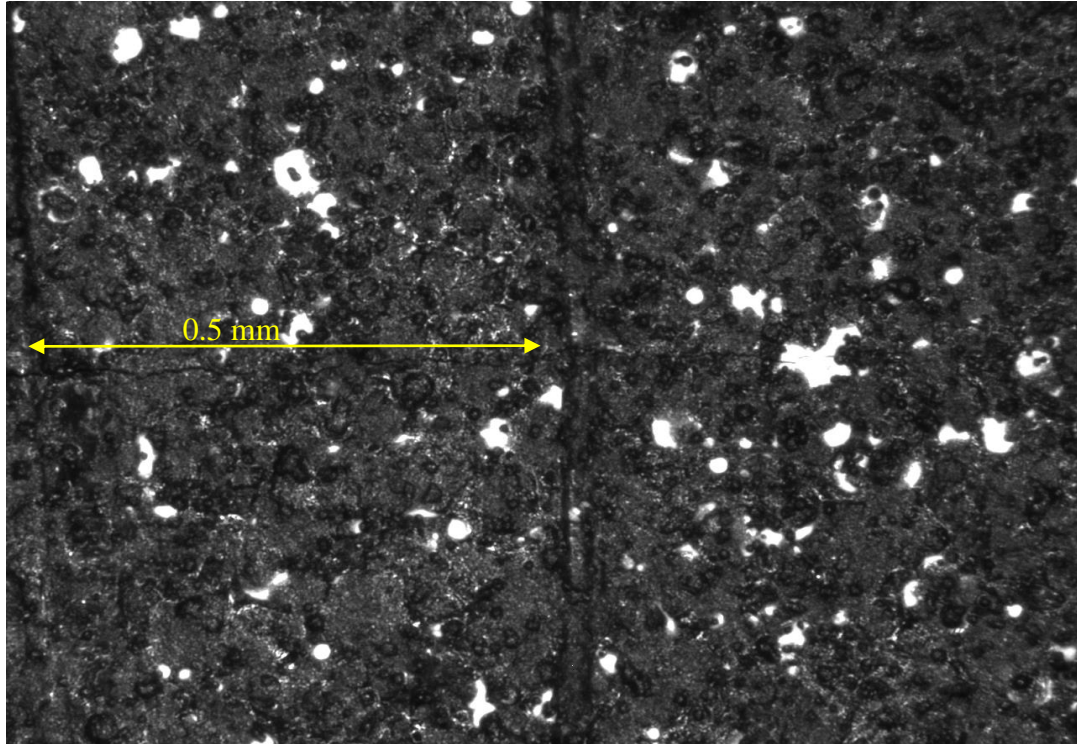
Figure 4.2 Image showing the crack length markings.

4.3   Digital Image Correlation

Once the test is completed and all the images are recorded along with the load displacement data for the cyclic tests, the ASTM standard D6671/6671M along with equations 14-16 can be used to calculate the strain energy release rates for the test configuration. The images are then loaded into DIC program Vic -2D by Correlated Solutions, Inc. for processing. It is very important to set the optimal parameters in Vic -2D for every test. The first step is to select the un-deformed specimen image at minimum load/displacement as the reference image. The area of interest is then selected with the crack at the center of this frame in the AOI Editor. The next step involves selecting the subset and the step size. The subset size controls the area of the image that is used to track

the displacement between images. The subset size has to be large enough to ensure that there is a sufficiently distinctive pattern contained in the area used for correlation [48].

The step size controls the spacing of the points that are analyzed during correlation. It is important to note that the analysis time varies inversely with the square of the step size; i.e., a step size of 1 takes 25 times longer to analyze than a step size of 5 [48]. For our tests, a subset between 25-31 depending on the type of the speckle pattern (23 for finer speckle and 31 for more coarse), and step size of 5 was chosen as this itself provided more than enough data required for calculating the fracture parameters.

Another important aspect of DIC is the Seed point. It refers to the point in the reference image where the correlation is started. The correlation algorithms use the results from the seed point to obtain an initial guess for the second point analyzed and continue in this manner until all points in the AOI are analyzed. Ideally, the seed point should be placed in the area of the image that underwent the smallest amount of motion during the test. An example is illustrated in the *Figure 4.3* below.
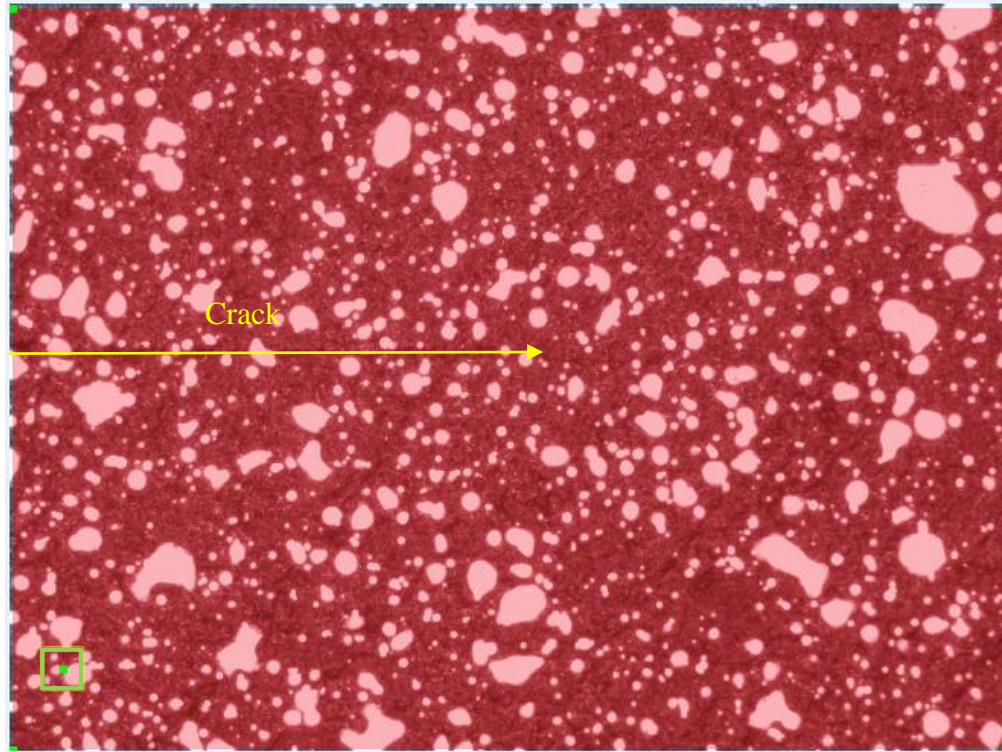
Figure 4.3 Seed point shown in the bottom left corner of the reference image with respect to the crack tip location

In this example, the seed point is placed on the top of the image away from the crack. This way, even as the test progresses and the specimen deforms the start location for the correlation experiences small motion.

This is followed by setting up the calibration scale so that the pixel scale in DIC can be directly converted to millimeters and the resulting strain and displacement data can be analyzed in real time directly from the contour plots. For this study, a scale of 304 pixels/mm was set for images taken at (640 x 480 resolution) at 25 X magnification level. The final step is running the correlation where again various parameters like method of interpolation, criterion and subset weights can be controlled to alter the processing time and power.

Once the correlation is complete, the X, Y location of the displaced pixels is reported, along with the U, V field displacements. This data is then exported in '.csv' files and fitting functions are applied in Microsoft Excel. The analytical displacements are calculated using u, v equations discussed in Section 4.6. The mean squared difference between the fit, and DIC data is then minimized with various parameters as variables using the Excel solver. Once the optimal fit is acquired, they may be plotted on contour plots to check consistency.

It is important to note here that the calculation of these displacement fields is dependent on the size of the field that is analyzed around the crack tip with G-dominance. This requires a good judgment and multiple runs of analysis before an approximate size of the field is chosen. As will be seen in section 5.4.2, the strain energy values show fluctuation and can be erroneous if the size of the field is too small or large. A smaller sized field would ignore a lot of data in the G-dominance region and report incorrect values of strain energy release rate that might differ from the global values by a significant factor.

4.4 Theoretical Framework for Full-Field Analysis- Linear Elastic Fracture Mechanics (LEFM)

As seen with the previous research [8], crack tip displacement analysis of composite specimens under mixed mode loading is accompanied by significant errors. Firstly, it is difficult to locate the exact location of the crack tip even under high magnification.
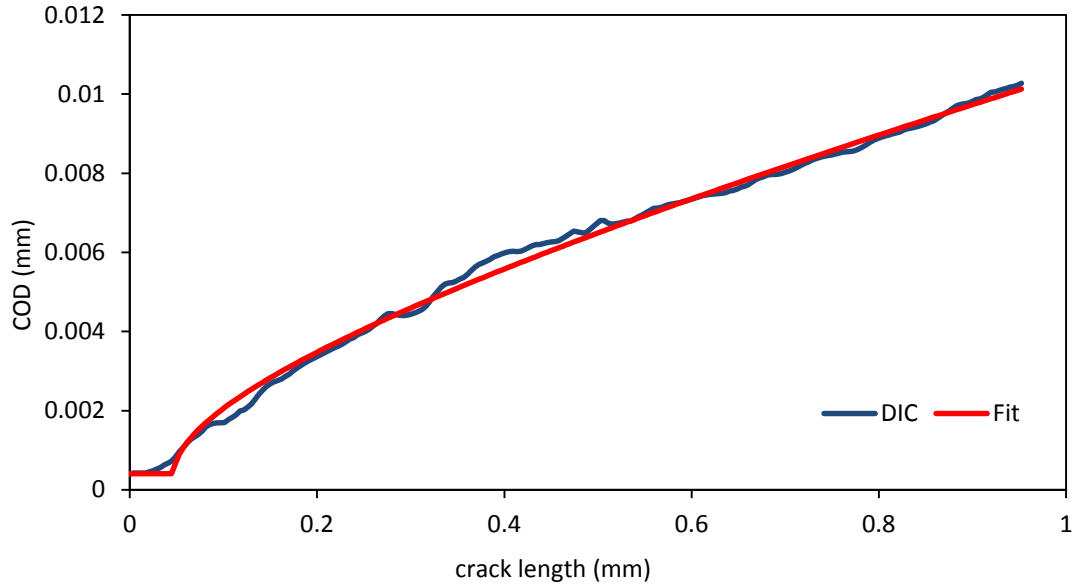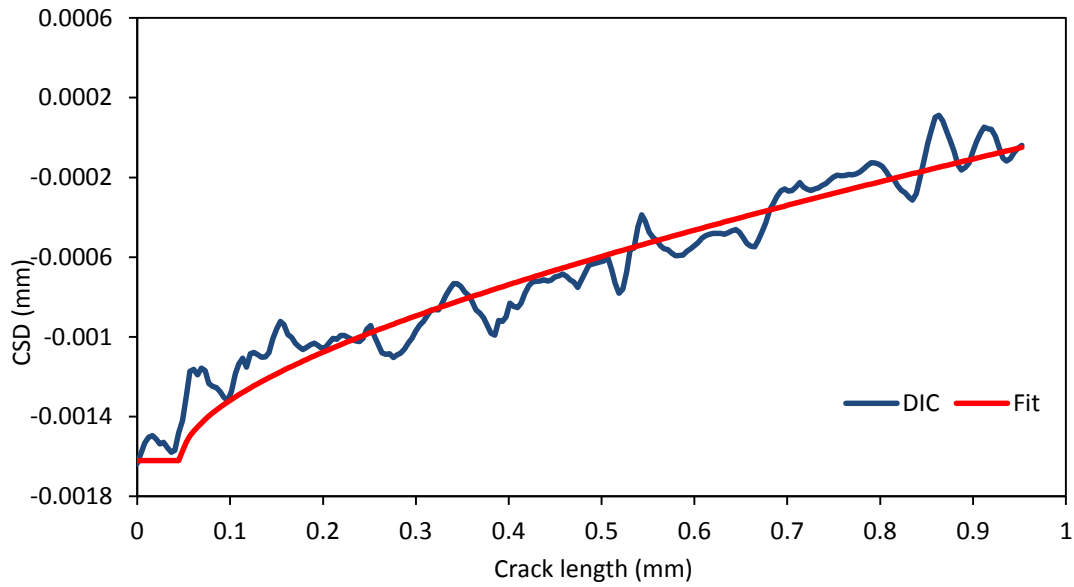
Figure 4.4 (a) Crack Opening Displacement (b) Crack Shear Displacement in mixed

mode analysis

Secondly, the crack opening displacement tool used in DIC is very sensitive to noise. As

a result, data extraction and displacement analysis become the primary issues limiting the

extraction of data using crack tip displacement theory. Comparison between the CSD and

COD fits clearly shows that higher order terms are very dominant in crack opening

displacement analysis, even when the far field solution is negated as is the case for the crack opening displacement. The reason is the specimen geometry under loading conditions. During loading, there are significant bending displacements; for crack shear displacement conditions, the bending displacements manifest themselves as higher order terms.

Global		Full Field DIC		CTD	
$G_I(J/m^2)$	$G_{II}(J/m^2)$	$G_I(J/m^2)$	$G_{II}(J/m^2)$	$G_I(J/m^2)$	$G_{II}(J/m^2)$
270.58	269.41	275.74	283.05	83.69	11.67

Table 4.1 G values at 218 N, 4400 cycles for 50 % mixity

For the 50 % mixity case the data was optimized using the r-squared (RSQ) function in Excel unlike the least squares sum used previously for 22 % mixity case. This results in better fits as compared to the previous data. However, the local G-values reported by the CTD fits near the crack tip are still considerably lower as seen in the Table 4.1. This gave rise to the need for analyzing the full field displacement of the specimens.

4.5 Deformation Fields around Crack Tip

The idea behind using full field displacement analysis is that increasing the number of data points to be analyzed with the fitting program will reduce the fracture parameters sensitivity to defects in the collected data. The raw data may be prescreened to remove excess and fallacious data, however the contours are represented in excel with files with over 100,000 data points. Manual deletion of erroneous data points would be a futile exercise. The use of Full field data analysis was implemented to negate many of the issues associated with crack tip displacement theory and generally improve the veracity of the

fracture parameters reported from DIC data extraction [8]. Full field analysis can also account for phenomena like fiber bridging which were previously neglected.

The complete expansion of the near tip deformation in homogeneous orthotropic solids was developed by Liu et al. [49] and Shukla et al. [50] for analyzing the stress intensity factor. The general equations for crack tip stress fields in anisotropic bodies were derived using complex variable approach by Sih et al. [33]. These were based on the discussion on displacement field near crack tip by Lekhnitskii et al. [32] in his book on *Theory of Elasticity of an Anisotropic Body*. Previously, Stress intensity factors alone represented the conditions for crack extension in orthotropic bodies but an attempt has been made to utilize these previous equations and combine them to account for the strain energy release rates in our transversely isotropic specimens. More recently, Mogadpalli et al. [38] used DIC to experimentally determine SIF for cracked orthotropic composites and fitted the theoretical displacement fields using the least squares method. He showed that the SIF was in good agreement with the theoretical results and demonstrated the applicability of the derived displacement fields and DIC technique for studying fracture in composites.

The detailed derivation of the full field equations may be found in reference [50]. The transversely isotropic elastic constants referred to in the following equations as a_{ij} are defined for unidirectional carbon fiber specimens used during this research. When an orthotropic material is aligned and loaded in the direction of the crack, parallel to the fiber direction, strain components can be assumed to be [32, 33, 38, 50]

$$\varepsilon_{xx} = \frac{\alpha - \beta}{2\alpha} \left\{ a_{12} - a_{11}(\alpha + \beta)^2 \right\} ReZ_1 + \frac{\alpha + \beta}{2\alpha} \left\{ a_{12} - a_{11}(\beta - \alpha)^2 \right\} ReZ_2$$
$$+ \frac{\beta}{2\alpha} \left\{ a_{11}(\alpha + \beta)^2 - a_{12} \right\} ReY_1 + \frac{\beta}{2\alpha} \left\{ a_{12} - a_{11}(\beta - \alpha)^2 \right\} ReY_2$$

(4.1)

$$\varepsilon_{yy} = \frac{\alpha - \beta}{2\alpha}\left\{a_{22} - a_{12}\left(\alpha + \beta\right)^2\right\}ReZ_1 + \frac{\alpha + \beta}{2\alpha}\left\{a_{22} - a_{12}\left(\beta - \alpha\right)^2\right\}ReZ_2$$ (4.2)

$$+ \frac{\beta}{2\alpha}\left\{a_{12}\left(\alpha + \beta\right)^2 - a_{22}\right\}ReY_1 + \frac{\beta}{2\alpha}\left\{a_{22} - a_{12}\left(\beta - \alpha\right)^2\right\}ReY_2$$

$$\gamma_{xy} = \frac{a_{66}}{2\alpha}\left(\alpha^2 - \beta^2\right)\left\{ImZ_1 - ImZ_2\right\} - \frac{a_{66}\beta}{2\alpha}\left\{\left(\beta + \alpha\right)ImY_1 - \left(\beta - \alpha\right)ImY_2\right\}$$ (4.3)

Where α and β are defined as follows:

$$2\alpha^2 = \frac{a_{66} + a_{12}}{2a_{11}} - \sqrt{\frac{a_{22}}{a_{11}}};$$

$$2\beta^2 = \frac{a_{66} + a_{12}}{2a_{11}} + \sqrt{\frac{a_{22}}{a_{11}}}$$

For a finite plate with an edge crack, the complex functions Z_1, Z_2, Y_1, Y_2 are defined as

follows [38, 50]:

$$Z_1\left(z_1\right) = \sum_{n=0}^{N}A_nZ_1^{n-1/2} \text{ and } Z_2\left(z_2\right) = \sum_{n=0}^{N}A_nZ_2^{n-1/2}$$ (4.4)

$$Y_1\left(z_1\right) = \sum_{m=0}^{M}B_mZ_1^{m} \text{ and } Y_2\left(z_2\right) = \sum_{m=0}^{M}B_mZ_2^{m}$$ (4.5)

Where:

N, M are the number of terms required for a good fit.

$$z_1 = x + i\left(\beta + \alpha\right)y = r_1e^{i\theta}$$
$$z_2 = x + i\left(\beta - \alpha\right)y = r_2e^{i\theta}$$
$$i = \sqrt{-1}$$

It should be noted that the x and y coordinate system has its origin coinciding with the

crack tip, with the x axis aligned along the direction of the crack. The strains are related to

the u and v displacement fields as follows:

$$\varepsilon_{xx} = \frac{\partial u}{\partial x}$$

$$\varepsilon_{yy} = \frac{\partial v}{\partial y}$$

$$\gamma_{xy} = \frac{\partial u}{\partial y} + \frac{\partial v}{\partial x}$$

<div align="right">(4.6)</div>

The integration of the equations (4.1), (4.2), (4.3) with respect to x and y yields the full field displacement components for u and v.

$$
\begin{aligned}
\mathrm{u} = {}& \frac{\alpha-\beta}{2\alpha}\left\{a_{12}-a_{11}(\alpha+\beta)^2\right\}Re\bar{Z}_1 + \frac{\alpha+\beta}{2\alpha}\left\{a_{12}-a_{11}(\beta-\alpha)^2\right\}Re\bar{Z}_2 \\
& + \frac{\beta}{2\alpha}\left\{a_{11}(\alpha+\beta)^2-a_{12}\right\}Re\bar{Y}_1 + \frac{\beta}{2\alpha}\left\{a_{12}-a_{11}(\beta-\alpha)^2\right\}Re\bar{Y}_2 \\
& + g(y)
\end{aligned}
$$

<div align="right">(4.7)</div>

$$
\begin{aligned}
v = {}& \frac{\alpha-\beta}{2\alpha}\left\{a_{22}-a_{12}(\alpha+\beta)^2\right\}\frac{Im\bar{Z}_1}{\beta+\alpha} + \frac{\alpha+\beta}{2\alpha}\left\{a_{22}-a_{12}(\beta-\alpha)^2\right\}\frac{Im\bar{Z}_2}{\beta-\alpha} \\
& + \frac{\beta}{2\alpha}\left\{a_{12}(\alpha+\beta)^2-a_{22}\right\}\frac{Im\bar{Y}_1}{\beta+\alpha} + \frac{\beta}{2\alpha}\left\{a_{22}-a_{12}(\beta-\alpha)^2\right\}\frac{Im\bar{Y}_2}{\beta-\alpha} \\
& + f(x)
\end{aligned}
$$

<div align="right">(4.8)</div>

$$\bar{Z}_1(z_1) = \sum_{n=0}^{N}\frac{2}{2n+1}A_n Z_1^{n+1/2} \quad \text{and} \quad \bar{Z}_2(z_2) = \sum_{n=0}^{N}\frac{2}{2n+1}A_n Z_2^{n+1/2}$$

$$\bar{Y}_1(z_1) = \sum_{m=0}^{M}\frac{1}{m+1}B_m Z_1^{m+1} \quad \text{and} \quad \bar{Y}_2(z_2) = \sum_{m=0}^{M}\frac{1}{m+1}B_m Z_2^{m+1}$$

Here, g(y) and f(x) in equations (4.7), (4.8) were found to be the rigid body translation in the x and y direction, as well as the rigid body rotation in the x-y plane. These values are unknown in the full field analysis and had to be estimated during the fitting calculations.

4.6 Determination of Strain Energy from DIC measurement and LEFM Theory

These displacement equations were refined further to account for rotations, displacements, and corrected to list pixel location based on its relative location to the crack tip during the previous research by Puishys et al. [8]. These equations are based on Poursartip's estimation of the crack tip displacement fields [30]. These have been discussed here and used to characterize the fracture parameters under cyclic loading. Some factors that need to be kept in mind before calculating these fracture parameters include correcting the data for rotation and translation, estimating the x, y location of the crack tip as well as the fracture parameters. The Microsoft Excel Solver can then be used until the difference between the analytical displacements and theoretical displacements, or the mean squares sum of the fit and the recorded displacement is at a minimum. The modified equations used in the fitting program are as follows:

$$u = (\sqrt{G_I} A_1 \sqrt{r} \left(k * \cos\left(\frac{\theta}{2}\right) - 0.5 * \cos(-1.5 * \theta) - 0.5 * \cos\left(\frac{\theta}{2}\right) \right) \tag{4.9}$$

$$+ \sqrt{G_{II}} A_2 \sqrt{r} \left(k * \sin\left(\frac{\theta}{2}\right) - 0.5 \sin(-1.5 * \theta) + 1.5 * \sin\left(\frac{\theta}{2}\right) \right) +$$

$$u_o + \frac{K_I}{2} A_1 r * \cos(\theta)(k+1) + \frac{K_{II}}{2} A_2 r * \sin(\theta)(k+1) + \xi(x,y)$$

$$v = (\sqrt{G_I} A_1 \sqrt{r} \left(k * \sin\left(\frac{\theta}{2}\right) + 0.5 * \sin(-1.5 * \theta) + 0.5 * \sin\left(\frac{\theta}{2}\right) \right) \tag{4.10}$$

$$+ \sqrt{G_{II}} A_2 \sqrt{r} \left(-k * \cos\left(\frac{\theta}{2}\right) - 0.5 \cos(-1.5 * \theta) + 1.5 * \cos\left(\frac{\theta}{2}\right) \right)$$

$$+ v_o + \frac{K_I}{2} A_1 r * \sin(\theta)(k-3) + \frac{K_{II}}{2} A_2 r * \cos(\theta)(-k-1) + \zeta(x,y)$$

where,

$$r = \sqrt{x^2 + y^2} \ ,$$

$$k = \frac{3 - v}{1 + v} \ ,$$

$$A_1 = \frac{4}{\sqrt{\pi}} * (2)^{1/4} * \left(\frac{1}{E_{11}} * \frac{1}{E_{22}} \right)^{1/4} * \left(\frac{\left(2 * \left(-\frac{v_{21}}{E_{22}} \right) + \frac{1}{G_{12}} \right)}{\left(\frac{2}{E_{11}} \right)} + \sqrt{\frac{E_{11}}{E_{22}}} \right)^{1/4} \ ,$$

$$A_2 = \frac{4}{\sqrt{\pi}} * (2)^{1/4} * \sqrt{\frac{1}{E_{11}}} * \left(\frac{\left(2 * \left(-\frac{v_{21}}{E_{22}} \right) + \frac{1}{G_{12}} \right)}{\left(\frac{2}{E_{11}} \right)} + \sqrt{\frac{E_{11}}{E_{22}}} \right)^{1/4}$$

$\xi(x, y)$: Accounts for the linear variation and back bending in the u field displacement

$\zeta(x, y)$: Accounts for the back bending in the v field displacement and the location of the neutral axis.

All these values are estimated and have a small value so, do not significantly affect the u and v field displacements. This fitting program requires that the pixel to mm conversion be set according to the magnification level to adjust the data to the actual scale. For a resolution of 640*480, at 25X magnification level this was set to 304 pixels/mm.
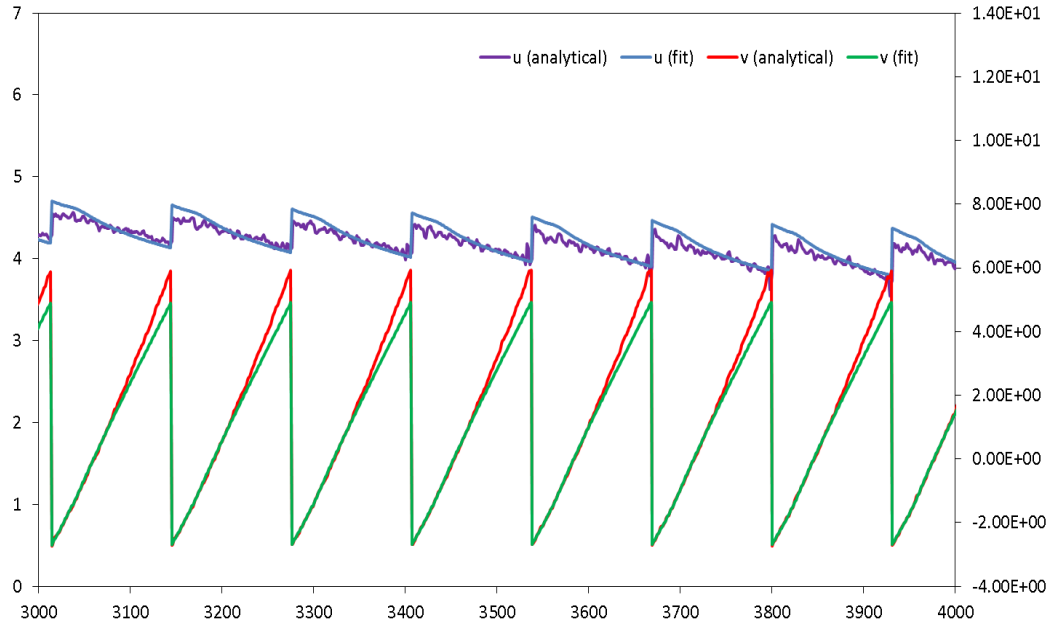
Figure 4.5 Full Field DIC measurements and fit functions showing a good fit for a 22%

mode mixity test near the crack tip.

The fitting functions for full field analysis on the data extracted from DIC have several parameters that need to be solved for. These include G_I, the Mode I strain energy release rate; G_{II}, Mode II strain energy release rate; K_I Mode I stress intensity factor; K_{II} Mode II stress intensity factor. Parameters such as the crack tip coordinates; u, v displacements relative to the crack tip location; crack and data rotation also need to be estimated during the fitting process and help in precisely gauging the fracture parameters. Higher order terms such as the front strain; u, v bending; higher order bending; location of the neutral axis; the linear variation in u field are also taken into account. A more accurate analysis may be conducted by reducing the size of the investigation area around the crack tip. This removes any bias from the far field solution and decrease the need for higher order terms. For further explanation of the steps involved in the process for fitting raw DIC data

to the full field displacement functions, and extracting fracture parameters, the author suggests referring to the previous research done by Puishys et al. [8].
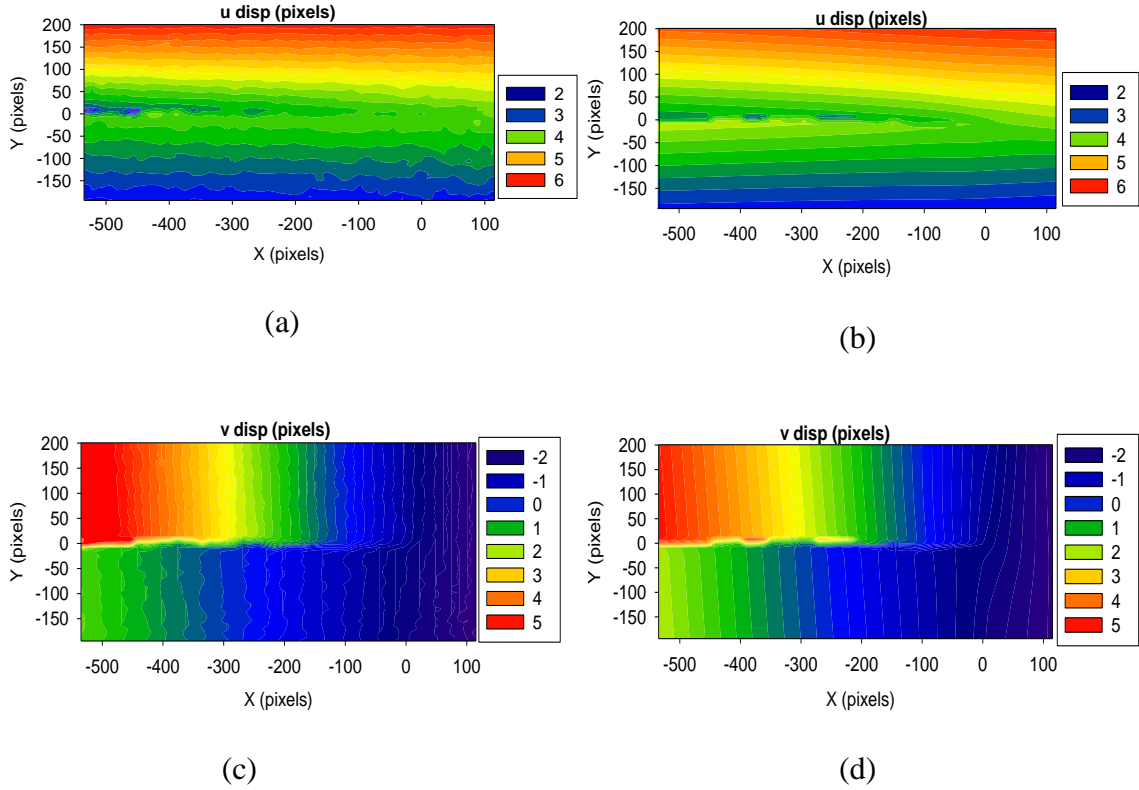
Figure 4.6 Full field displacements comparing u field displacement in DIC measurement (a) and fit data using LEFM theory (b); v field displacements in DIC measurement (c) and fit data using LEFM theory (d)

Figure 4.6 (a) to (d) shows a comparison between the analytical data and the fit data in a sigma plots. It is seen in *Figure 4.6 (a) and (c)* that the fit data is noisy, though it does show the correct location of the crack tip. The size of the area under investigation was taken as 200 pixels around the crack tip, hence, the data away from the crack tip is much noisier than it is near the crack tip. However, this data is good enough to extract the fracture parameters. The G_I and G_{II} values for this data extracted at 40N after 3135 cycles are 55.55 J/m^2 and 18.019 J/m^2 resp. This gives an overall mode mixity of about 24% with the crack

tip at (133.99, 225.72). A better and cleaner fit would require more iterations of the solver and more processing power, which is not necessary for the current data.

The subsequent chapters will discuss the results obtained experimentally and analytically using full field data under different mixities.

5 Experimental Results

5.1 Mixed Mode Crack Growth Criteria

The following reported data is for all the tests conducted consistently with the test protocols outlined in section 3.1, under various mode mixities and loading ratios. The following plots in *Figure 5.1* show the load-displacement response of the specimen under static loading. The critical strain energy release rates from the quasi-static loading were used to find the critical load and load levels for the cyclic fatigue tests. The maximum load levels were taken to be around 70% - 80% of the critical load determined from the quasi-static fracture tests. For tests performed under load control the loading ration was maintained at 0.1 to keep it consistent with the literature [7, 11, 45].

(a)
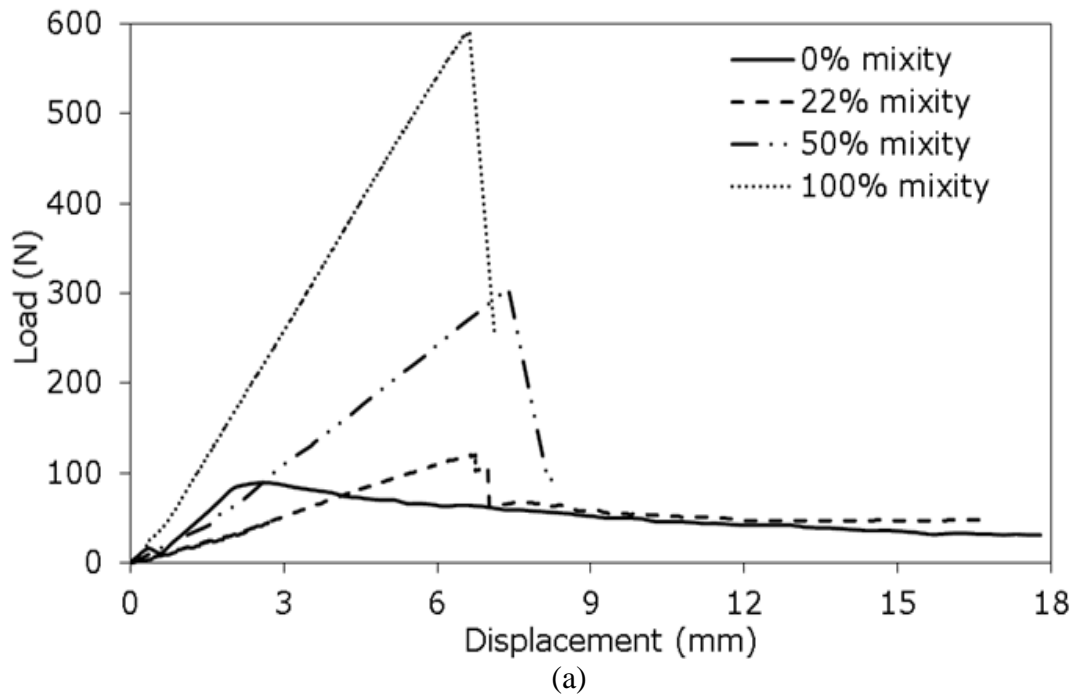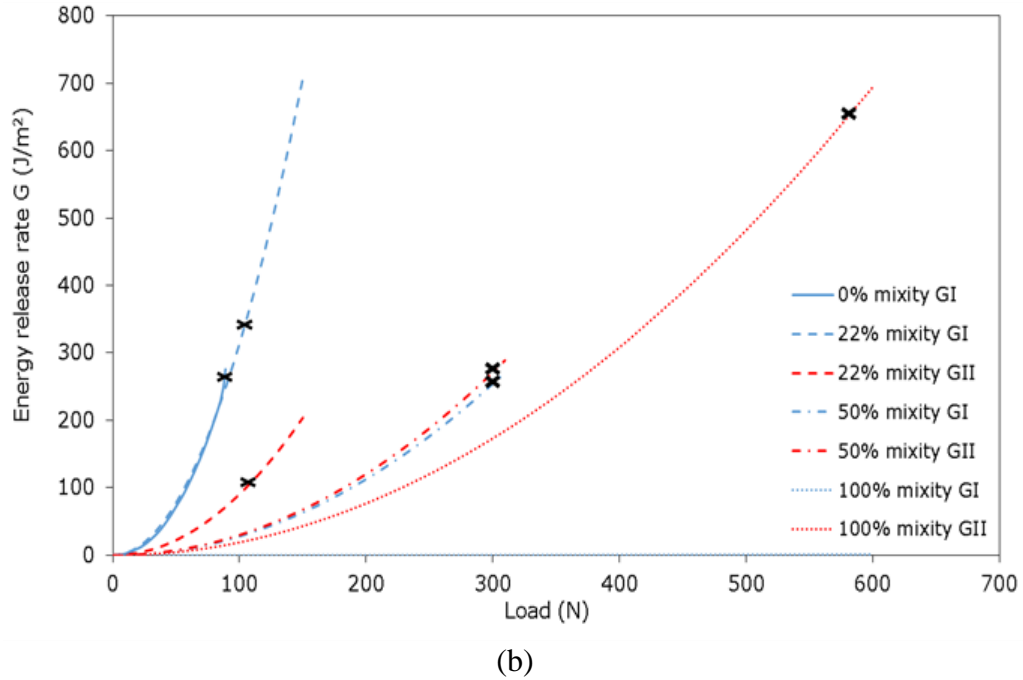
Figure 5.1 (a) Load-displacement response under static loading (b) Critical strain

energy release rates under static loading

Results published in the literature also indicate that whether the test is conducted in load

or displacement control does not affect the relationship between strain energy release rate

and the fatigue crack growth rate [11]. As such, tests were conducted under load control

and displacement control, and these will be mentioned clearly while discussing the results

from the tests. This resulted in a slight growth of the crack but this was not included in the

cyclic loading results and was accounted for as a pre-crack. The tests were then cycled until

the crack grew about 2 mm from the tip of the pre-crack. However, as loading under

different mode mixities is governed by different local micro-mechanisms, the number of

cycles required to reach this crack length varies significantly from a few hundred cycles

under Mode I to thousands of cycles under pure mode II. Images were taken at regular

intervals during the tests so that the strain energy release rate could be measured after the

test.

DIC was used to analyze the images taken during the test and the analytical strain energy values were calculated using the equations developed in Section4.6, and these values were then compared to the experimental data obtained from the modified ASTM fracture parameters. It was noted that the strain energy levels attained under cyclic loading were lower than that achieved under quasi-static loading primarily due to the slowing of crack growth rate.

Section 5.6, discusses the primary shielding mechanisms like micro-crack growth and fiber bridging. The variation in the strain energy release rates can be explained using the arresting conditions where secondary cracks and fiber bridging behind the crack may reduce G and slow down growth. Fiber bridging is not uniform (as will be explained later in the text) and this affects the growth curve differently depending on the context of the bridging mechanism. These observations have been reported previously by Miyajima and Sakai et al. [51].

5.2   Mode I Loading (0% mode mixity)

These tests were conducted using the Double cantilever beam specimens with an end notch originating from the Teflon insert on the Bose ElectroForce load frame. The test conditions can be seen in the Table 5.1. The cyclic data and the load –displacement curves for test 2 can be seen in the *Figure 5.2(a), (b)*. It is worth noting that the pure mode I tests were conducted under load control because it was much easier to gauge the damage at known load levels from the quasi-static tests. In order to avoid the large discontinuities or jumps during the initial loading cycle arising from the potential notch effect from the delamination insert, the samples were loaded slowly to the maximum load required for

cyclic loading. This resulted in the crack growing from a pure natural crack and not the pre-crack under cyclic loading.

5.2.1 Cyclic Loading Parameters

Typical cyclic load displacement data was collected for the duration of the test at regular intervals and can be seen in *Figure 5.2*. The crack growth was recorded directly from the images and was also calculated using the empirical compliance formula. This was used to correct the crack growth data and gives a much more accurate reading of the crack tip location. This crack length data was used to calculate the strain energy release rate analytically at various intervals during the test. These values were then compared with the data obtained from DIC.

(a)   (b)
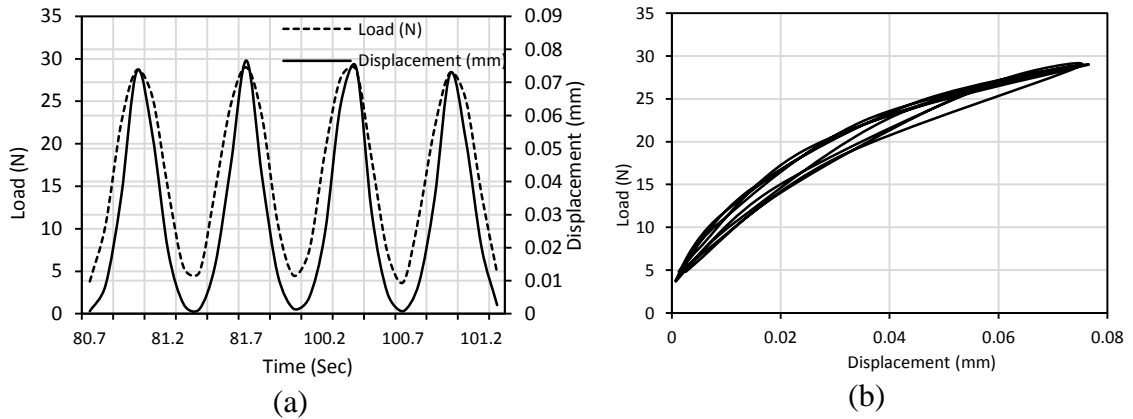
Figure 5.2 Mode I (a) load-displacement vs time (b) load time response for test under

load control

Test #	Frequency	Maximum Load	Load ratio (R)	Cycles
1	1 Hz	20N	0.10	3000
2	1.5 Hz	30 N	0.10	10000
3	5 Hz	30 N	0.10	30000

Table 5.1 Test Conditions for 0% mode mixity under load control

In Pure Mode I case, it is worth noting that the unloading cycle does not follow the same path as the loading cycle and some hysteresis is seen in the load displacement curves. This is probably due to the shielding effects like fiber bridging which are predominant during loading in pure mode I tests and do not play a role while unloading.

Using Equation (3.8), the strain energy release rate is calculated for pure Mode I. For 30 N load at 2400 cycles and a total crack length of 35 mm it results in a global strain energy release rate of 31.63 J/m^2 (G_I). The crack length was recorded directly from the images that were taken. The next section compares this global value to the analytically calculated strain energy release rates.

5.2.2 Experimental Results

Figure 5.3 shows the results for a pure mode I test conducted at 1.5Hz with a loading ratio of 0.01. *Figure 5.3(a), (b)* shows the initial deformation of the specimen loaded to 3N under static load. As the number of cycle progress the crack growth can be seen in the subsequent images at 300 cycles and 2400 cycles. Although this specimen was tested for 10000 cycles, only the deformation for 2400 cycles is shown here as the frame of reference needs to be changed as the crack tip grows out of the frame. In *Figure 4.6,* these displacements fields have been plotted in sigma plot to verify the accuracy of the location of the crack tip and hence have not been shown here again. The strain plots show the increasing damage with time in the crack tip region. A full field analysis of the DIC data at 300 cycles 30 N yields a strain energy release rate of 22.72 J/m^2 (G_I) and 0.051 J/m^2 (G_{II}) whereas, by restricting the area that is analyzed around the crack tip to 50 pixels yields

a near field strain energy release rate of 23.30 J/m^2 (G_I) and 0.051 J/m^2 (G_{II}) with an overall

mode mixity of 0.22 %.

No. of Cycles	Global GI [J/m^2]	Global GII [J/m^2]	Mixity [%]	Full field GI [J/m^2]	Full field GII [J/m^2]	Mixity [%]	GI (50 Pixels around crack tip) [J/m^2]	GII (50 Pixels around crack tip) [J/m^2]	Mixity [%]
300	23.31	0	0	22.72	0.051	0.22	23.30	0.051	0.22
600	30.62	0	0	12.77	1.06	7.69	12.76	1.06	7.67
2400	31.63	0	0	28.23	0	0	28.23	0	0

Table 5.2 Strain energy rates from DIC at full field and a reduced size field of 50 pixels compared to Global data from ASTM analysis

0.05   V mm   0.008

(a) 0 cycles 3N

0   E$_{yy}$ 0.02

(b) 0 cycles 3N

0.028   V mm   0.031   0 E_{yy} 0.02

(c) 300 cycles 30N   (d) 300 cycles 30N

0.0213   V mm   0.0247   0 E_{yy} 0.02

(e) 2400 cycles 30N   (f) 2400 cycles 30N
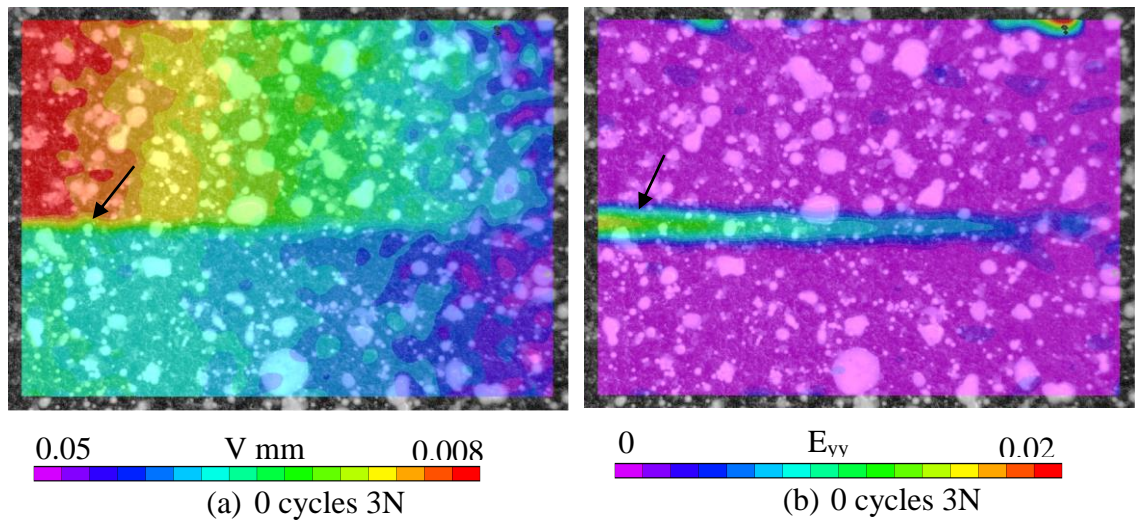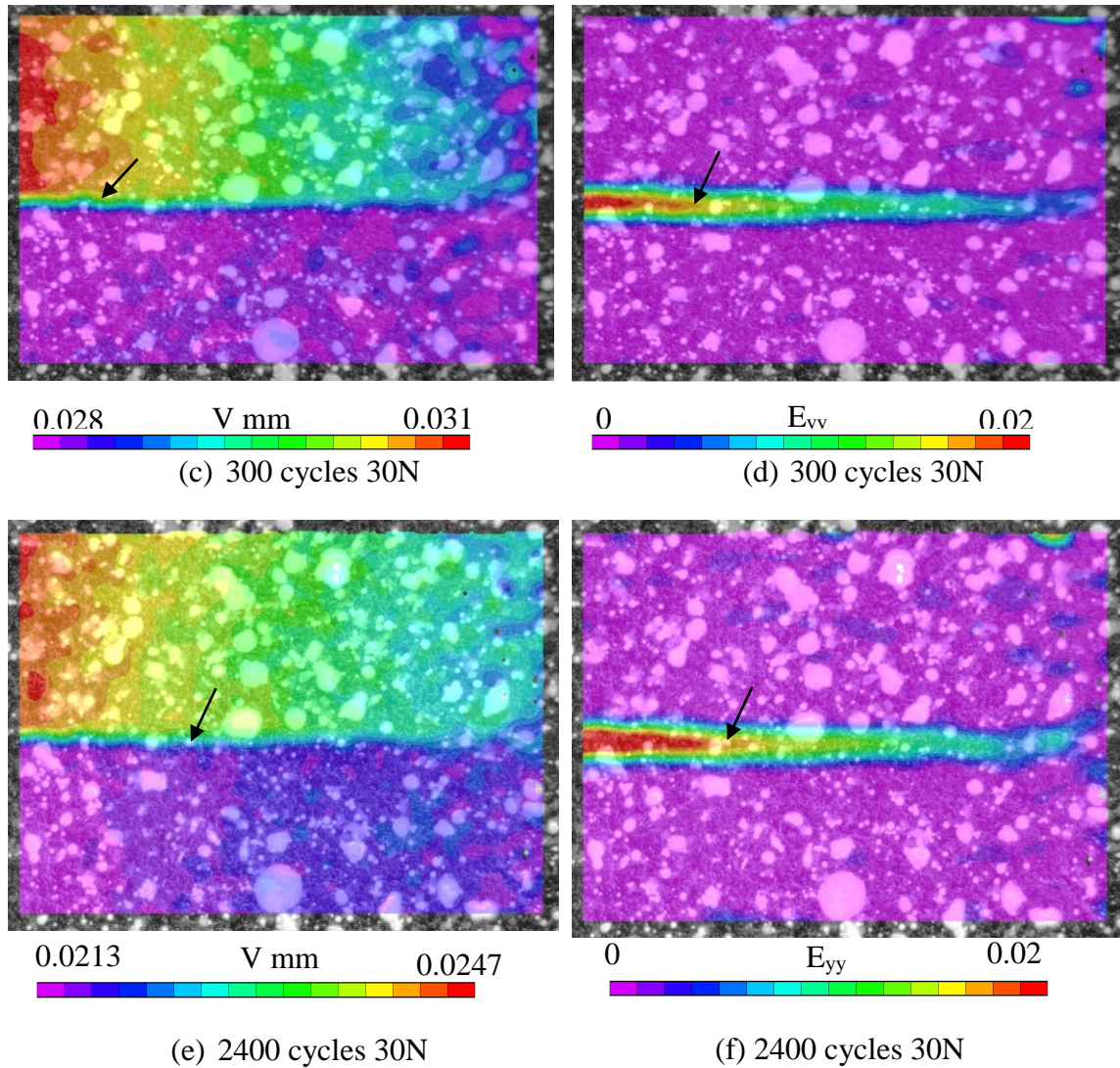
Figure 5.3 Change in v field displacement (mm) (a, c, e) and E_{yy} strain (b, d, f) for Mode I test illustrating crack growth and location of the crack tip

5.3   Mixed Mode Loading (22% mixity)

These tests were conducted with unidirectional carbon fiber specimen under displacement control. The lever arm length on the MMB fixture was adjusted to provide 22% mode mixture. Compared to the pure mode I case, 22 % mode mixity case has a mode II component as well. As result, shear micro-cracks develop in front of the crack tip which coalesce and result in the delamination growth. These micro-cracks can been seen in *Figure 5.9(a)*. Fiber bridging is also known to occur due to the slight misalignment in the fibers

63

that occurs during the fabrication stage. A DIC analysis performed on these captured images to show strain development near these micro-cracks has been discussed in Section 5.6.

5.3.1 Cycling Loading Parameters

As seen in *Figure 5.4 (b)*, the hysteresis in loading and unloading curves is due to the fiber bridging and friction components that become active during the loading and do not play a role in unloading. The load displacement data was recorded at regular intervals and was used to calculate the compliance and calibrate the correct crack length recorded from visual inspection. Unlike pure mode I, these tests were stopped after 1500 - 2000 cycles as enough crack growth and damage was observed. The global strain energy rates for this case were calculated using Equation (3.12), (3.13). The values of global strain energy change over cycles as a function of the crack growth. Due to the micro-mechanisms like fiber bridging and friction, the crack growth and as a result the change in strain energy release rate is small. These values can be seen as the solid line in *Figure 5.5(a), (b)*. The small bump in the G_I and G_{II} values around 155 cycles is due to a static crack growth.


(a)   (b)
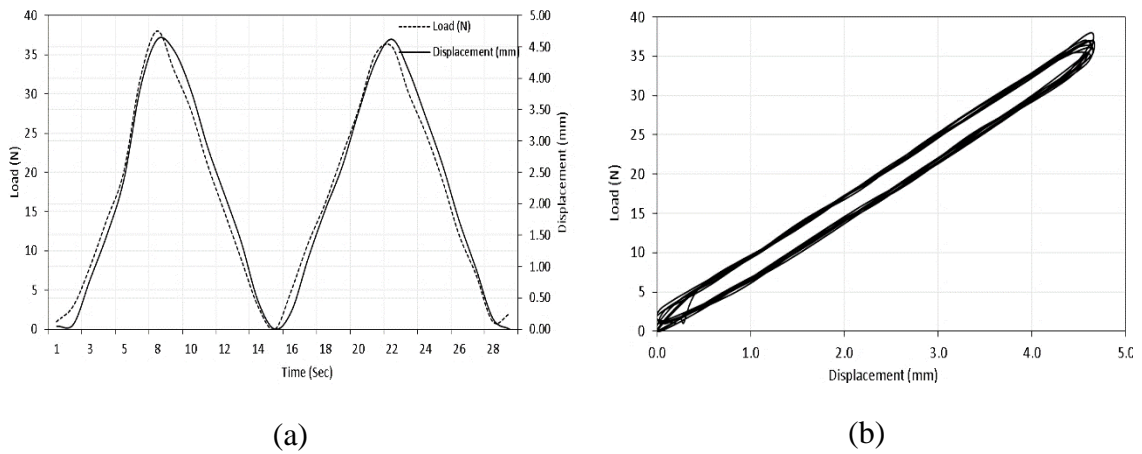
Figure 5.4 (a) Load/displacement vs time (b) Load- Displacement response for 22 %
Mode II under displacement control

Test #	Frequency	δ_{max}	Cycles
1	0.20 Hz	3.37 mm	1000
2	0.15 Hz	4.63 mm	1000
3	2 Hz	4.57 mm	2000

Table 5.3 Test conditions for 22% mode mixity under displacement control

5.3.2 Experimental Results

Figure 5.5 provides a comparison between the analytically calculated data for the

22% mode test and the global data obtained from the modified ASTM protocols used for

MMB fixture. It can be seen that the 90% confidence interval for the analytically calculated

strain energy release rates is significantly wide. Clearly, the global strain energy release

rates are much lower than the analytical values as they do not account for the local factors

affecting the crack growth and are based on crack length growth observed at the

macroscopic level and calibrated using the compliance. The analytical equations are

sensitive to the exact crack tip location and depend on the area analyzed around the crack

tip. Initially, these images are analyzed at 250 pixels which results in values closer to the

global values,   as a smaller area is analyzed(50-100 pixels) these values change

significantly which is evident in *Figure 5.5*. The dip in near field G_I and G_{II} before 155

cycles is due to the existence of multiple crack tips. The analytical calculations were used

to find the G values at different crack tips using the Excel solver which returns an optimum

value of $G_I = 119.24$ J/m^2 and $G_{II} = 50.32$ J/m^2 at a crack tip marked by large E_{yy} strain as

shown in *Figure 5.9 (b),* resulting in an overall mixity of 29.67%. The corresponding global

values are 100.27 J/m^2 and 30.77 J/m^2. This is followed by an increase in the strain energy

values due to the static crack growth which shows that the analytical calculations done on

the data from DIC using Excel are accurately responsive to the change in crack length.

(a)

(b)
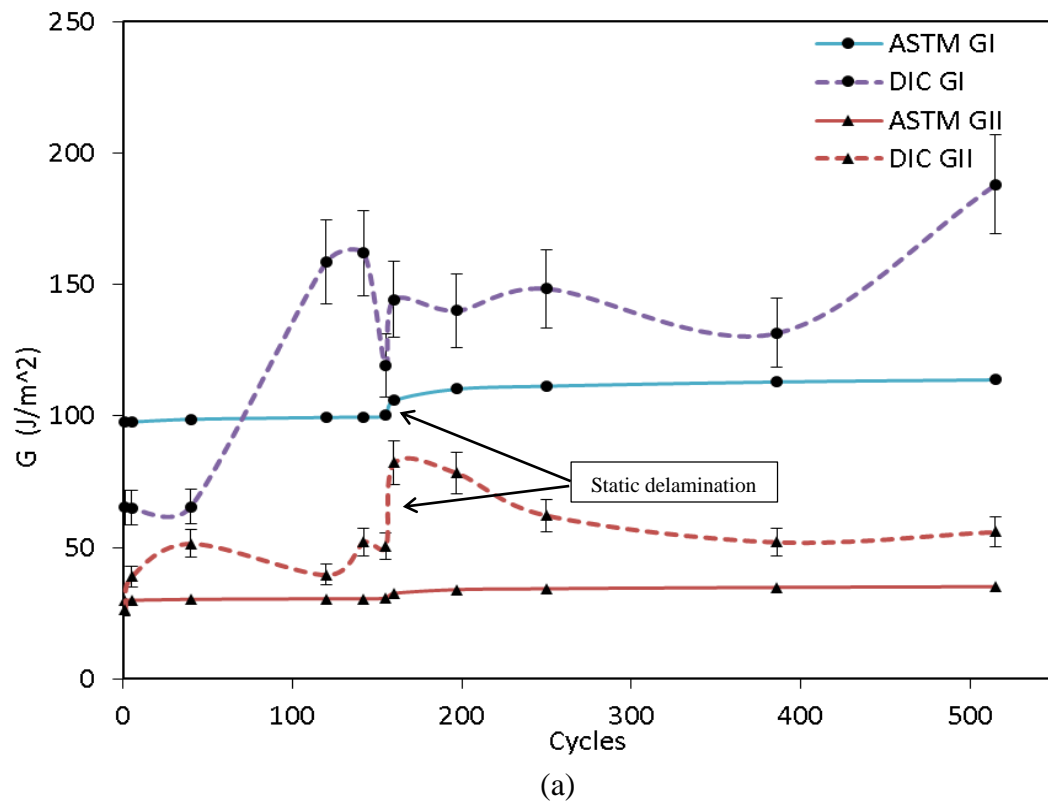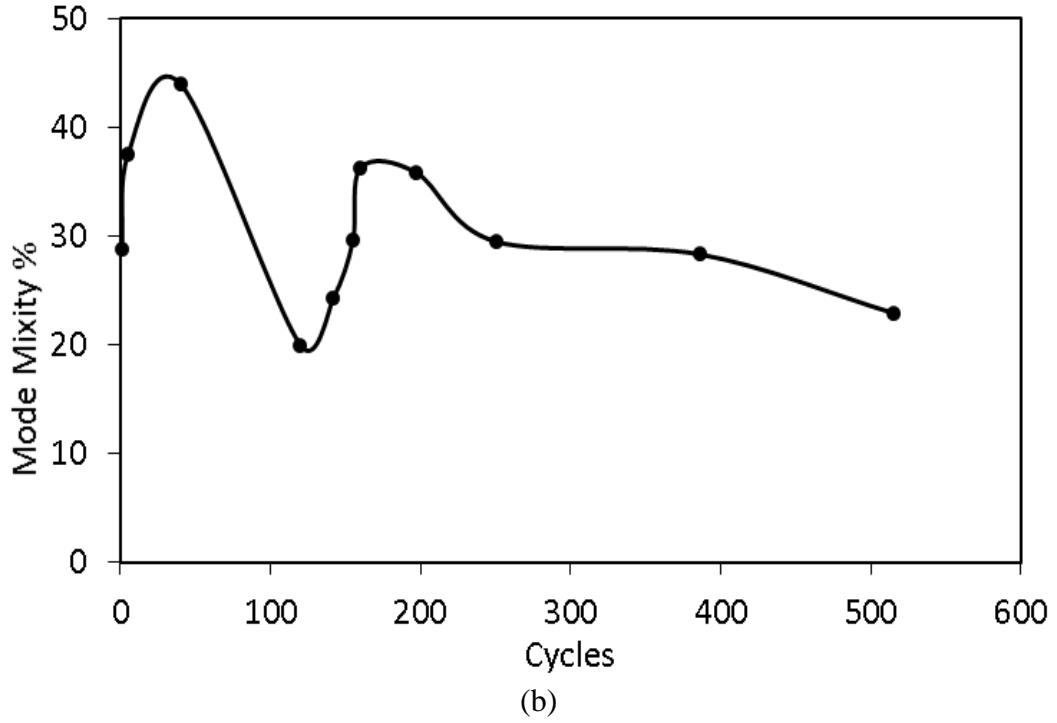
Figure 5.5 (a) Comparison of experimentally obtained(ASTM) and analytically derived(DIC) strain energy release rates under 22 % mode mixity with 90% confidence interval range (b) Change in mode mixity with number of cycles
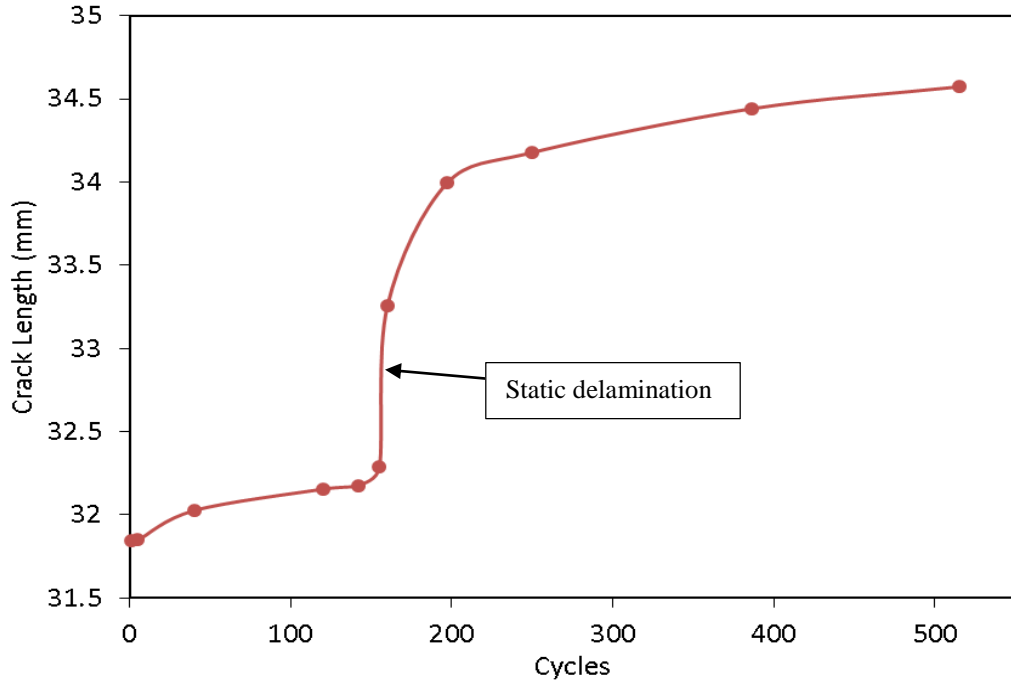

Figure 5.6 Total crack length growth vs number of cycles for 22 % mode mixity under load control

Contour plots generated from the raw u and v fields (*Figure 5.7 (a, c)*) which are extracted from DIC are compared to the analytically fit (*Figure 5.7 (b, d)*) u and v fields obtained from the optimized solution. This further supports that the developed Excel solution can locate the exact crack tip location and hence, accounts for the correct G values in near field. These contour plots developed in Sigma plot show the crack growth under cyclic loading at 5 cycles and then after 200 cycles. It is worth noting that in order for the solver to successfully converge to an optimized solution, it is necessary to remove the micro cracks from correlation and the crack tip should be positioned in the center of the frame. This is illustrated in *Figure 5.9 (b)*. This helps to accurately determine the actual crack tip which can then also be used to correct the visually observed crack tip.
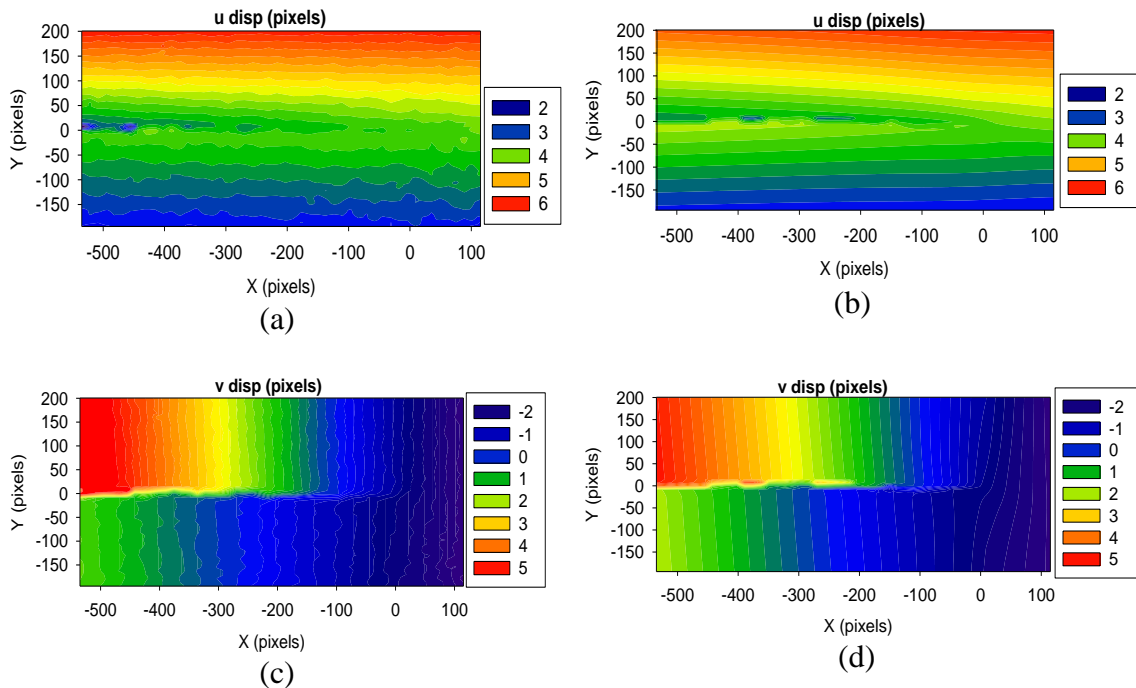
Figure 5.7 Full field displacements comparing DIC measurement (a,c) and fit using LEFM theory (b,d) u and v fields at 5 cycles showing the location of the crack tip

68
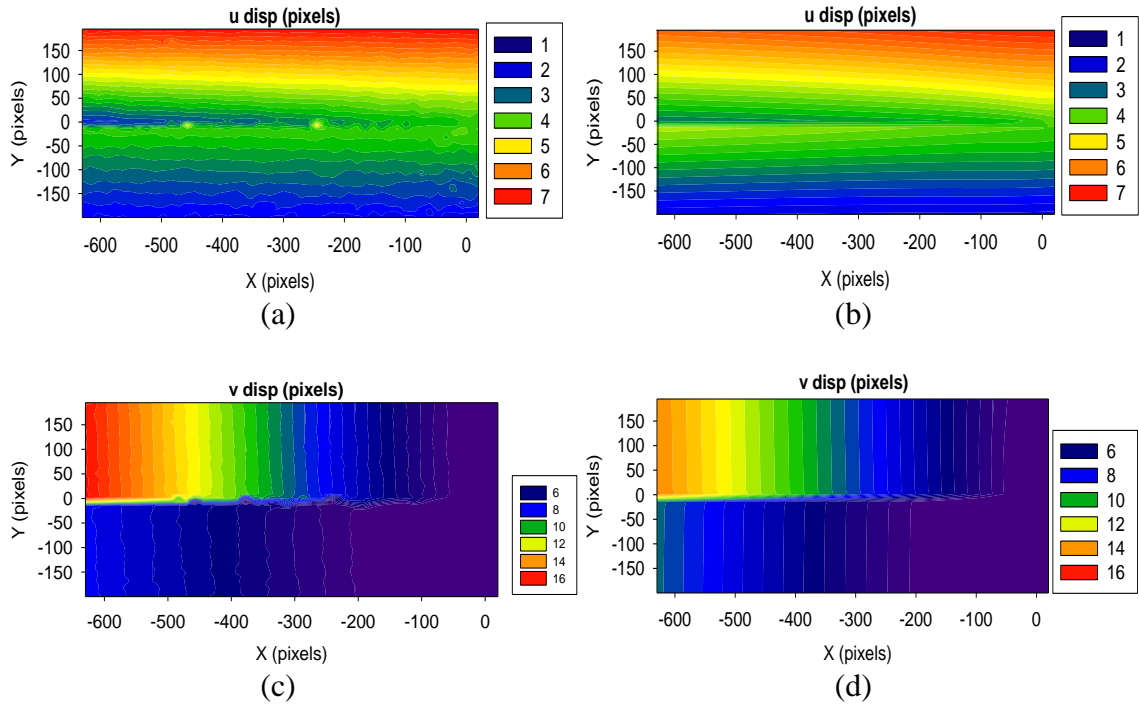
Figure 5.8 Full field dispalcements comparing DIC measurement (a,c) and fit using LEFM theory (b,d) u and v fields at 200 cycles showing the position of the crack tip

(a)
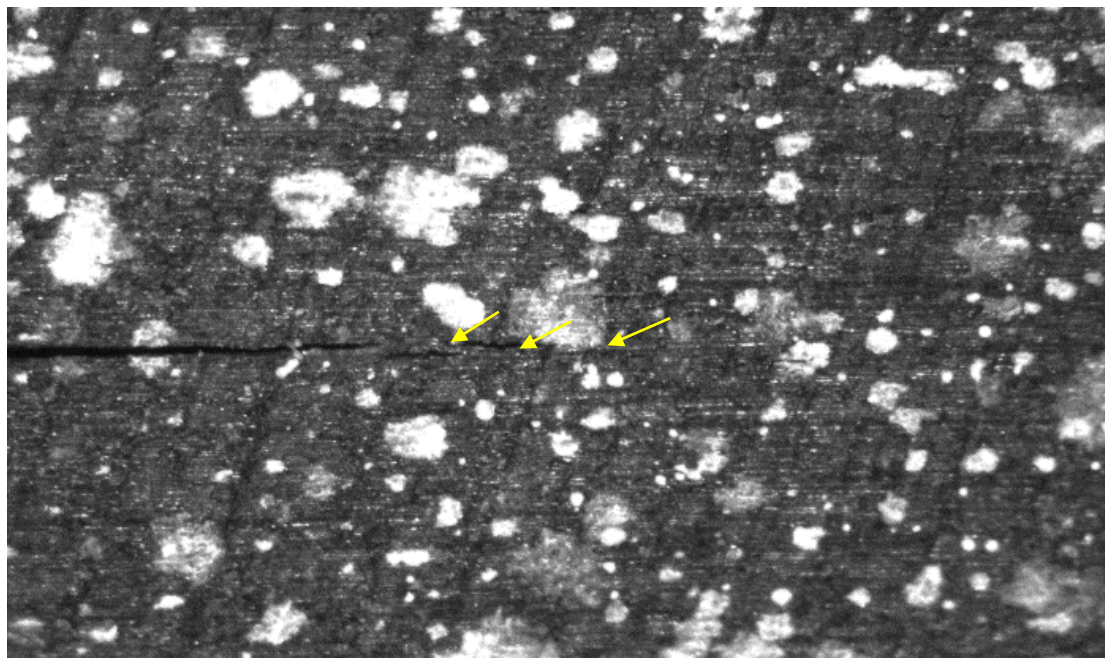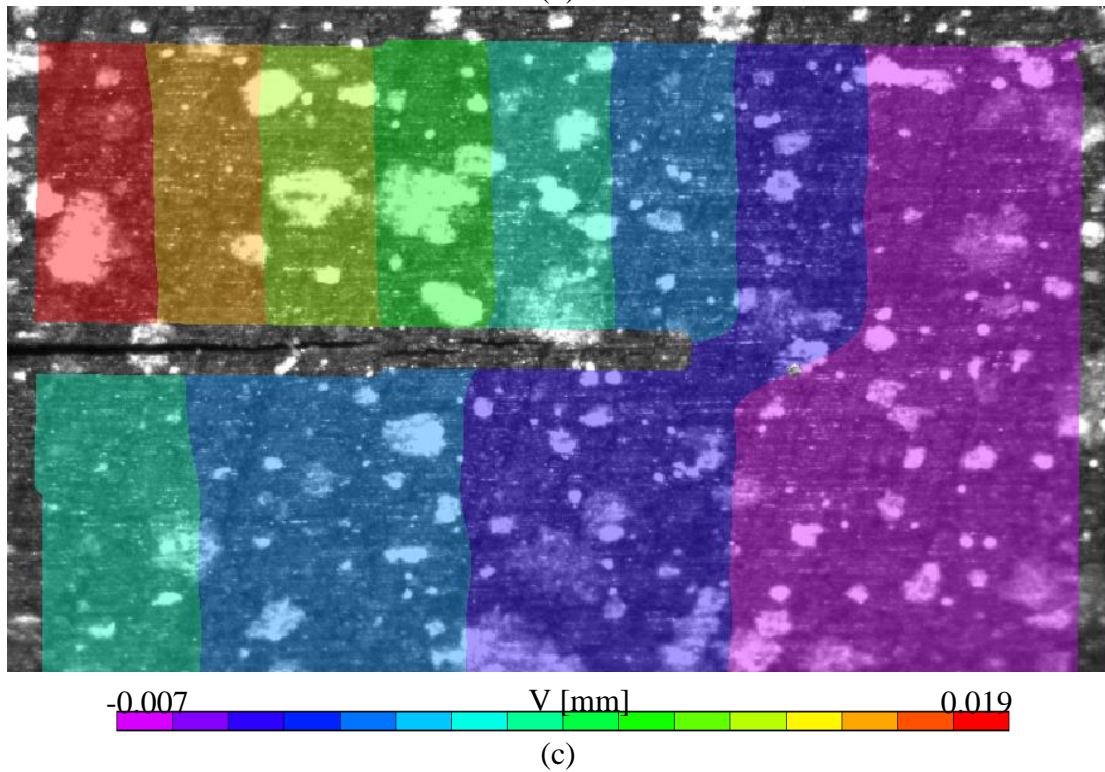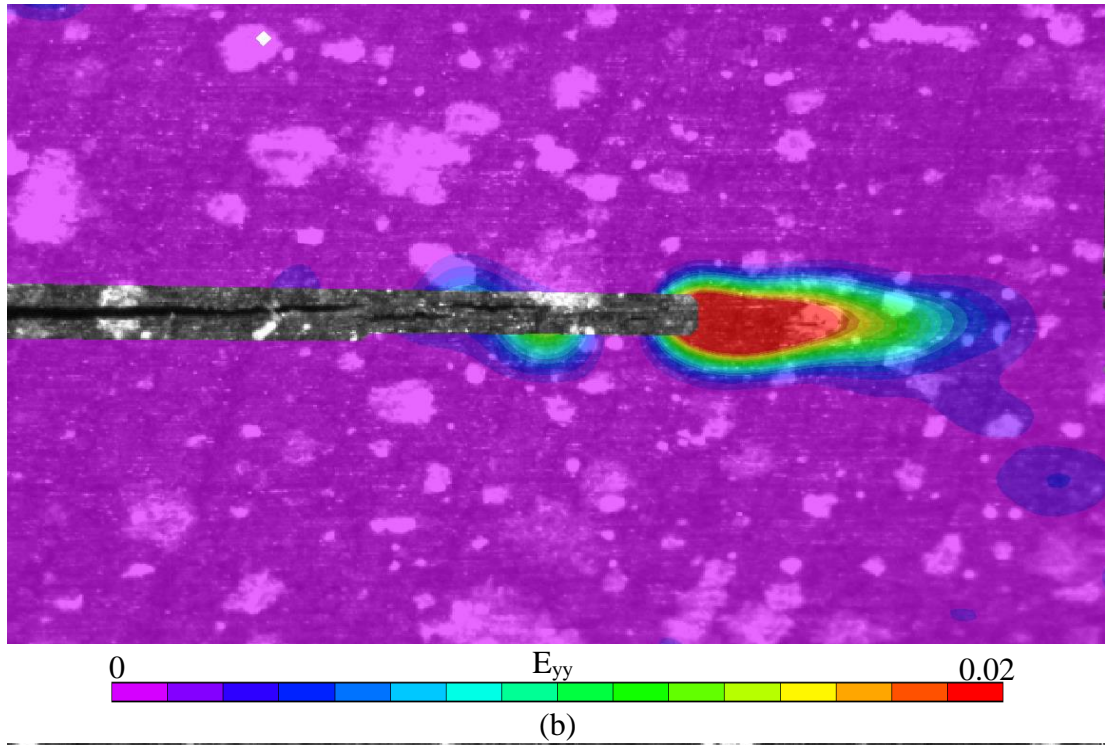
Figure 5.9 (a) Multiple crack tips originating infront of the primary crack tip, (b) E_{yy} strain infront of the primary crack tip with the area behind the crack tip excluded from correlation, (c) v (mm) field displacement of the specimen near the actual crack tip at 155 cycles

5.4   Mixed Mode Loading (50% mixity)

Similar to the 22 % mode II case, tests were conducted under 50 % mode mixity using the MMB-35 fixture. The lever length 'c' was set to 47 mm to set the fixture in 50 % mode mixity. To analyze the deformation fields, Digital Image Correlation is used, and requires a random speckle pattern to track displacements. A fine speckle pattern was generated on the edges of the specimen using white and black spray paint as shown in *Figure 5.10*. As the size of the Area of Interest (AOI) is reduced by increasing the magnification, finer speckles are needed and require more precise pattern generation approaches.
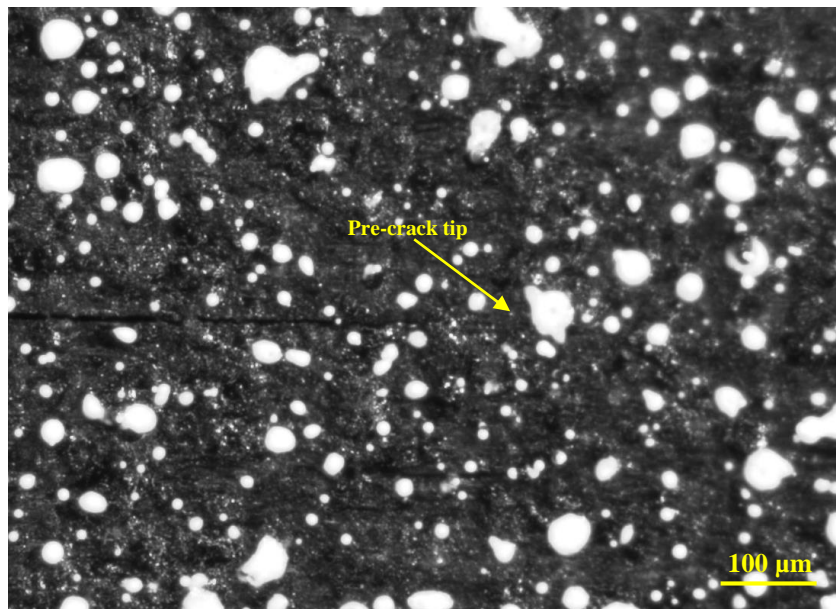
Figure 5.10 Speckle pattern on the specimen at 50X showing the pre-crack tip

The objective of these initial tests was to observe the material behavior near the crack tip where $\sqrt{r}$ and K field are dominant. In order to do this a high magnification of 50X (see scale) was used along with the external illumination. The images at such high magnification demand some adjustment to the settings in order to get the required sharpness and gain levels, so that the crack-tip can be seen clearly.

71

From previous fatigue tests at 22 % mode mixity and quasi-static tests done at 50 % mode mixity it was learnt that the crack propagates at a fairly high speed. In order to run DIC, a reference image was taken at minimum load with the crack tip near the left edge of the image as it grows towards the left. The new reference image (un-deformed) at minimum load was chosen every time the crack tip went out of the frame and a new frame was chosen.

5.4.1 Cyclic Loading Parameters

The shear component becomes more prominent in 50 % mode mixity as the hysteresis in the loading and unloading curves is considerably large.
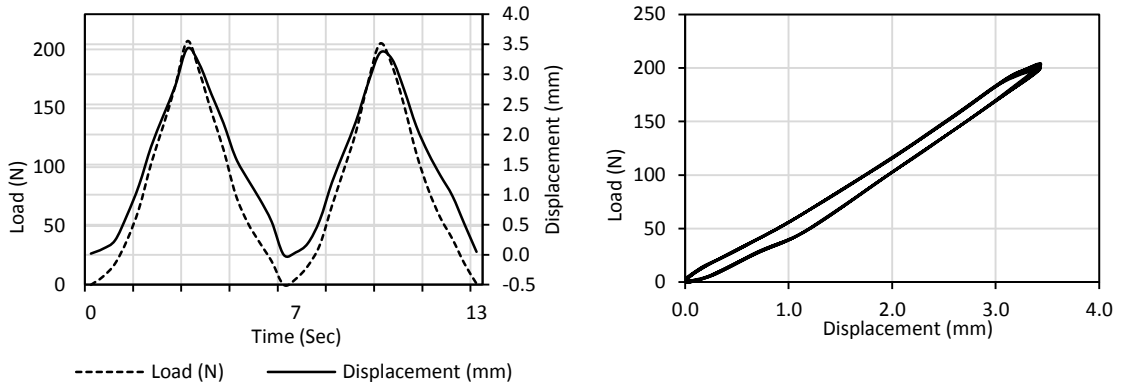
Figure 5.11 (a) Load/displacement vs time (b) Load- Displacement response for 50 %

Mode II under displacement control

Test #	Frequency	δ_{max}	Cycles
1	0.15 Hz	2.83 mm	800
2	0.17 Hz	3.43 mm	7000

Table 5.4 Test conditions for 50% mode mixity

5.4.2 Experimental Results

To monitor crack length, the DIC results were again used to identify the crack tip position, and then the visually observed location was refined to produce a more accurate value since it is not easy to visually observe the crack with the fiber structure of the test specimen aligned in the direction of the crack. As mentioned earlier, size of the field for DIC measurement strongly affects the fracture parameters. This is illustrated in a plot below that compares the variation of analytically strain energy values obtained from DIC with the global vaues at varying sizes of the field. It is seen that at about 600 pixels the analytical values correspond to full field values and are comparable to the global values.
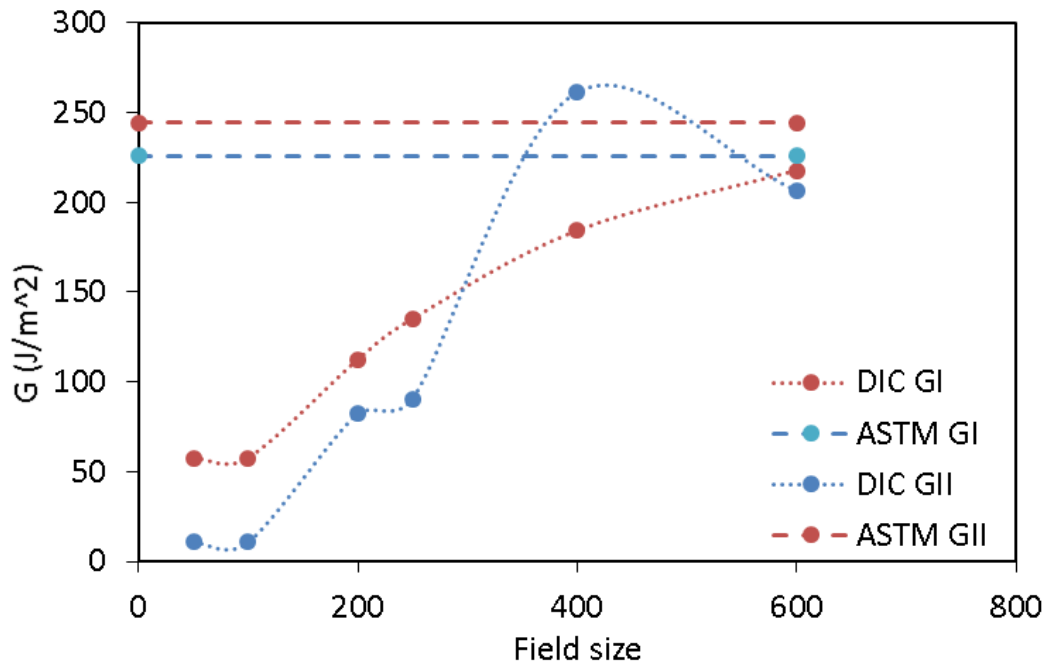
Figure 5.12 Dependence of strain enrgy relase rate on the size of the field for 50% mode mixty test at 900 cycles and 205 N load
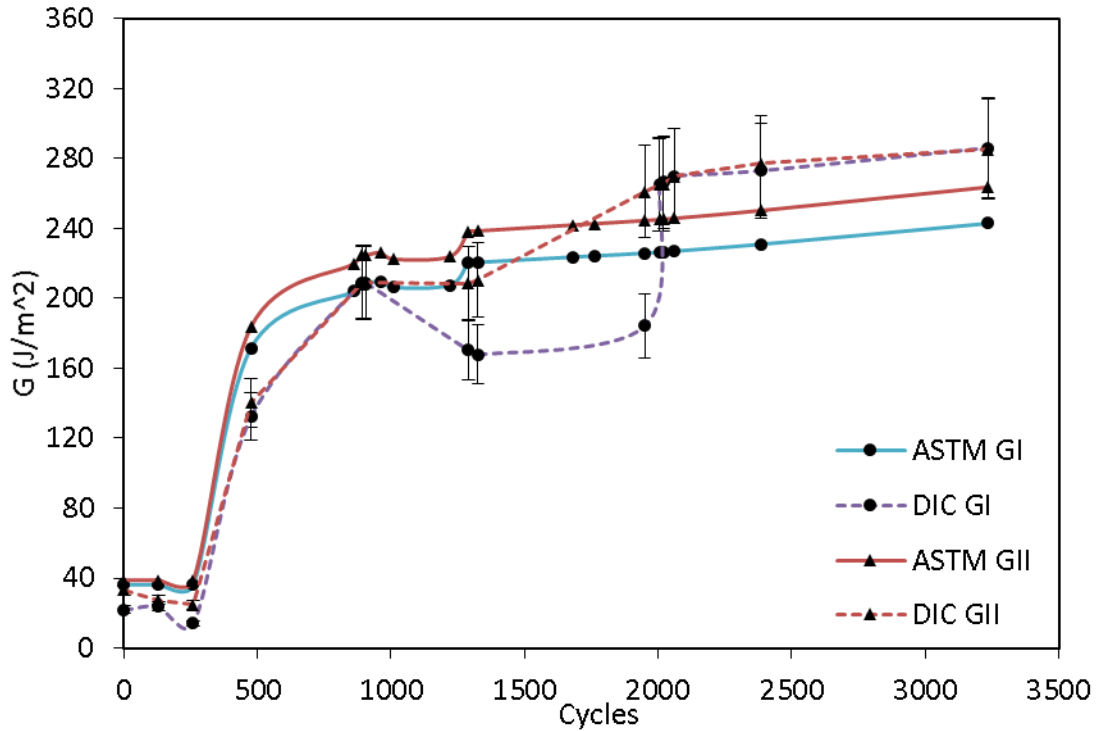
(a)
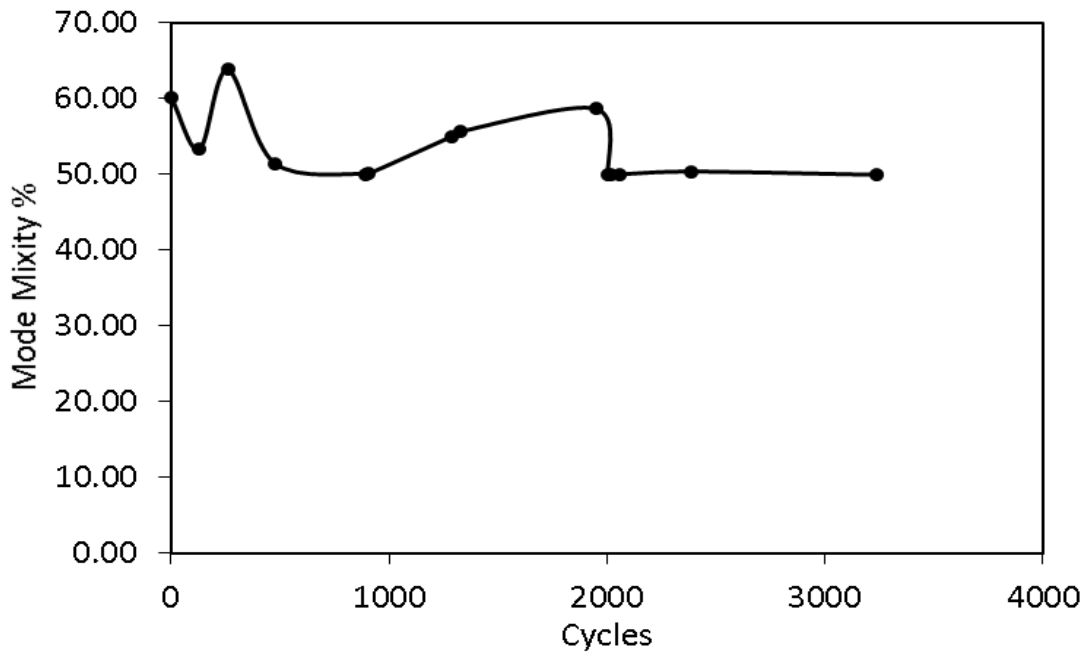
(b)

Figure 5.13 (a) Comparison of experimentally obtained(ASTM) and analytically
derived(DIC) strain energy release rates under 50 % mode mixity with 90% confidence
interval range (b) Change in mode mixity over number of cycles
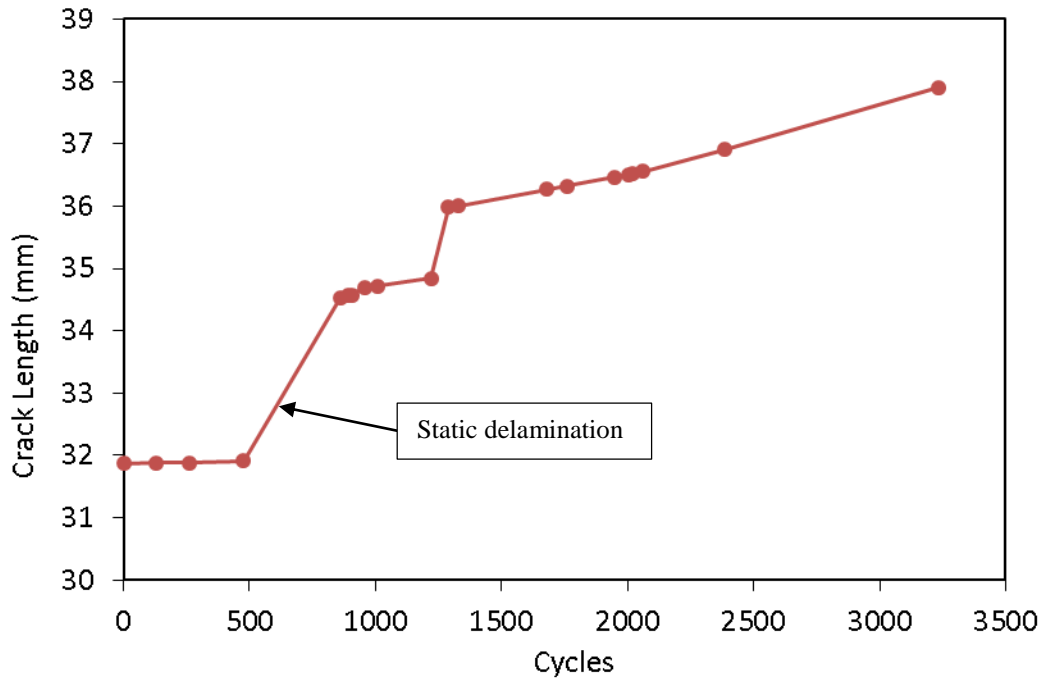
Figure 5.14 Total crack length growth vs number of cycles for 50 % mode mixity under load control
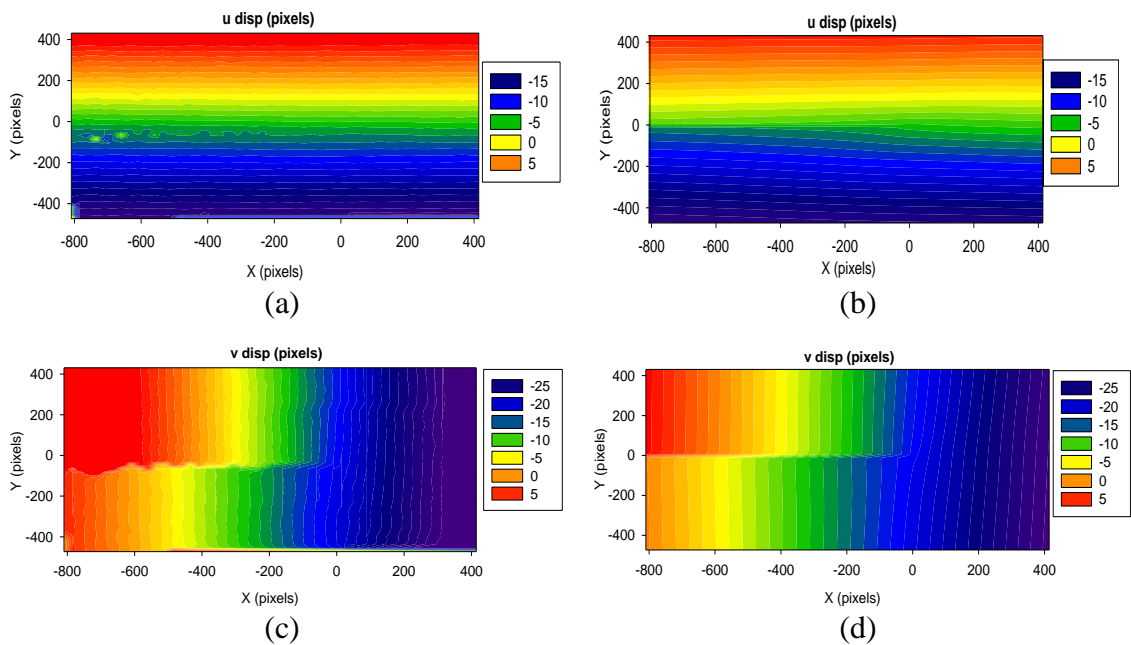
Figure 5.15 Full field displacements comparing DIC measurment (a,c) and fit using LEFM theory (b,d) u and v fields at 130 cycles

5.5 Mode II Loading (100% mode mixity)

Pure mode II test were carried out using the MMB-35 fixture by adjusting the lever length 'c' to 20 mm. This results in a mode mixity of 99% and this is the highest mixity that can be achieved using the MMB fixture. The reason for using the MMB fixture instead of a 3 point bend setup is that the slight mode I content helps in visible crack growth which is easier to analyze using DIC rather than 3 point bend which on the other hand, is accompanied by large bending and rotation of displacement fields. These tests were carried out under load control and displacement control. The specimens used a 2" Teflon insert as a starter crack. The images were taken at 25X magnification to track the damage around the crack tip. Next section describes the loading conditions for one of the tests conducted under load control to about 50000 cycles. During the analysis of this test, an attempt was also made to predict the fatigue life of the specimen using the Paris law which will be discussed in Section 6.1.

5.5.1 Cyclic Loading Parameters

Figure 5.16 shows the cyclic load displacement for a 100% mixity test conducted at 2 Hz under load control. It can be seen in *Figure 5.16 (b)* that there is no hysteresis in the curve which aptly suggest the absence of shielding effects like fiber bridging during loading and unloading which were prominent under mode I and mixed mode tests. The noise seen in the *Figure 5.16 (a)* is due to the data being collected at 1000 scan points every 10 seconds and can be ignored as the noise being detected by the Bose ElectroForce load frame.
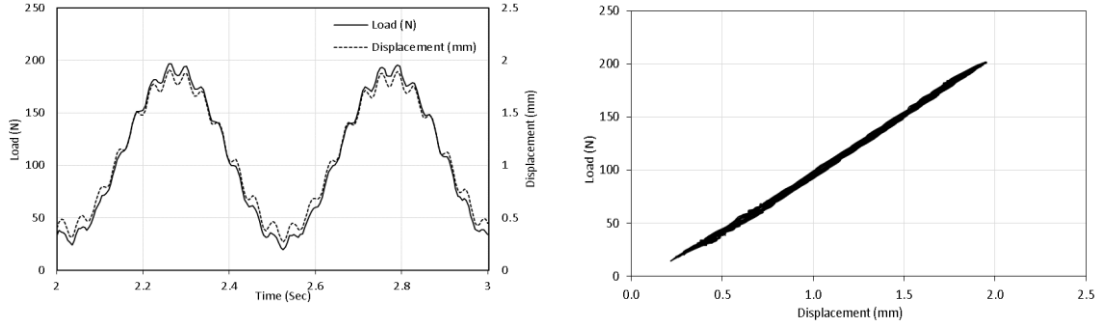
Figure 5.16 (a) Load/displacement vs time (b) Load- Displacement response for 100 %

Mode II under displacement control

Test #	Frequency	δ_{max} /R	Cycles
1	1 Hz	2.25 mm	5000
2	1 Hz	2.42 mm	4000
3	2 Hz	0.1	65000

Table 5.5 Test conditions for 100% mode mixity

5.5.2 Experimental Results

Figure 5.17 illustrates the variation of near field strain energy values calculated analytically

using DIC with the global strain energy values. It is observed that the mode mixity of the

test specimen changes under localized effects, the analytical values being calculated for

full field area around the crack tip. The global strain energy rates are outside the 90%

confidence interval of the full field analytical values. This phenomenon is not observed

under quasi-static loading and suggests that the localized effects might be affecting the

mixity under fatigue loading.

(a)

(b)
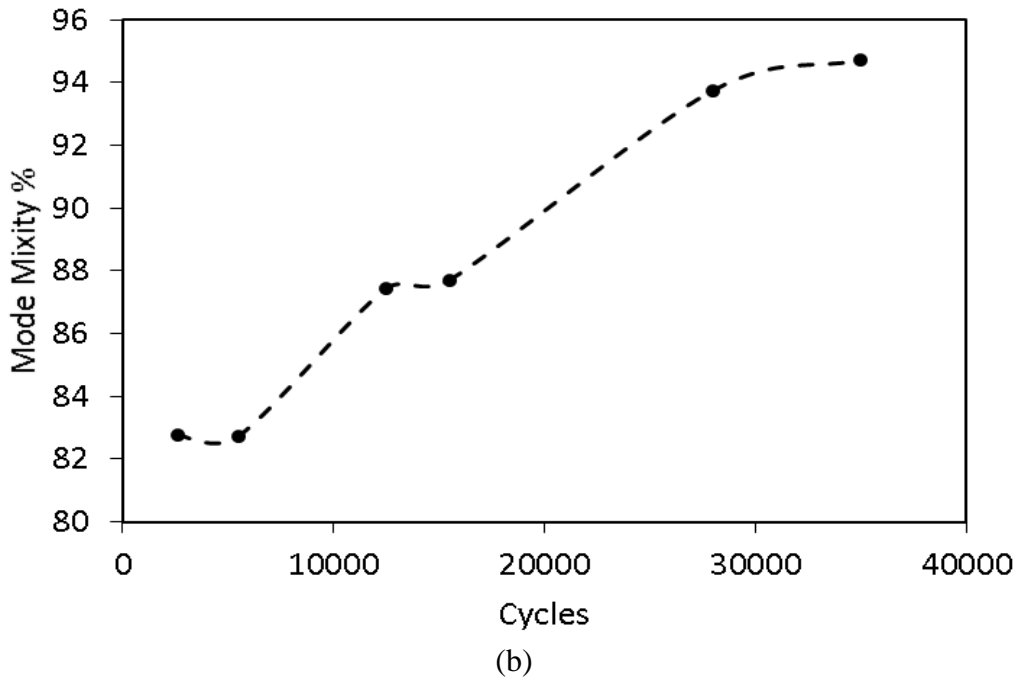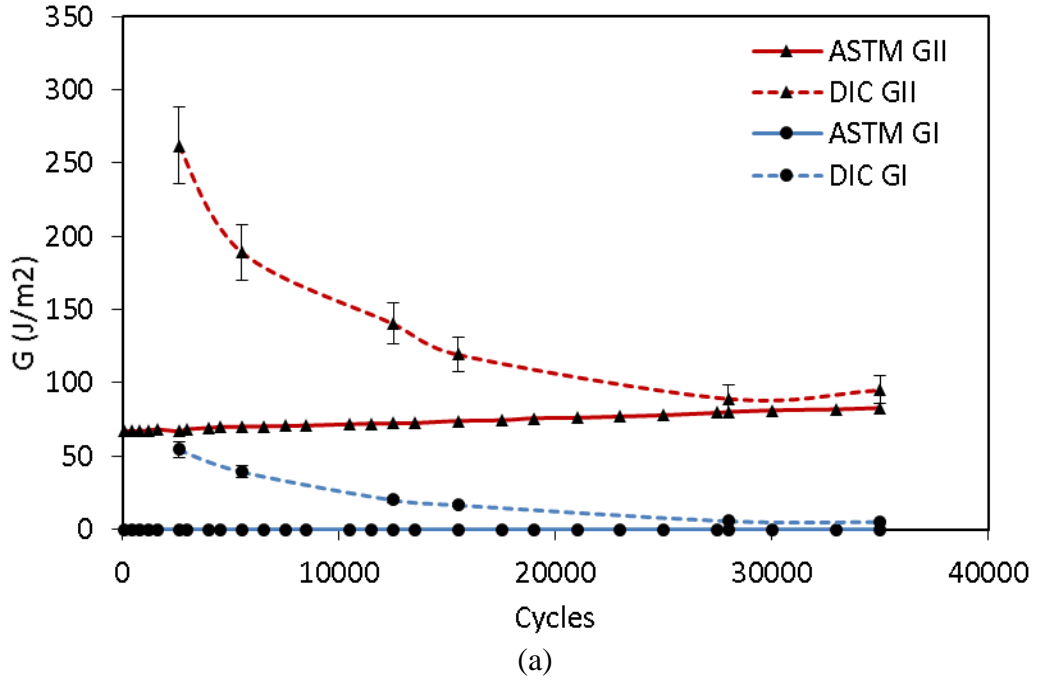
Figure 5.17 (a) Comparison of experimentally obtained(ASTM) and analytically derived(DIC) strain energy release rates under 100 % mode mixity with 90% confidence interval range (b) Change in mode mixity with number of cycles
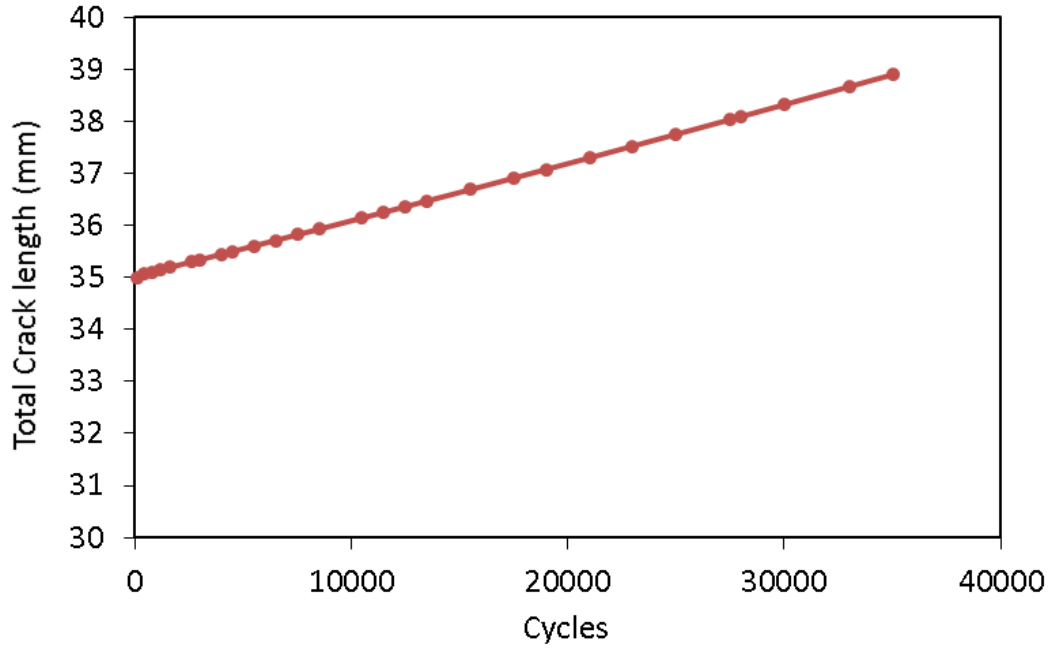
Figure 5.18 Total crack length growth vs number of cycles for 100 % mode mixity under load control
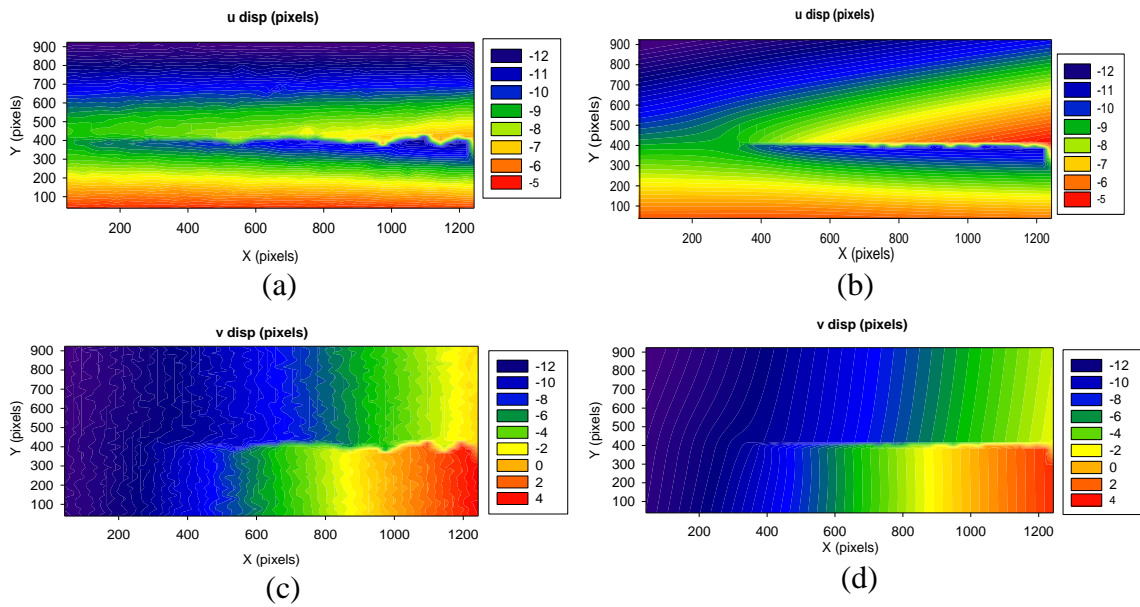

Figure 5.19 Full field displacements comparing DIC measurement (a,c) and fit using LEFM theory (b,d) u and v fields at 5500 cycles
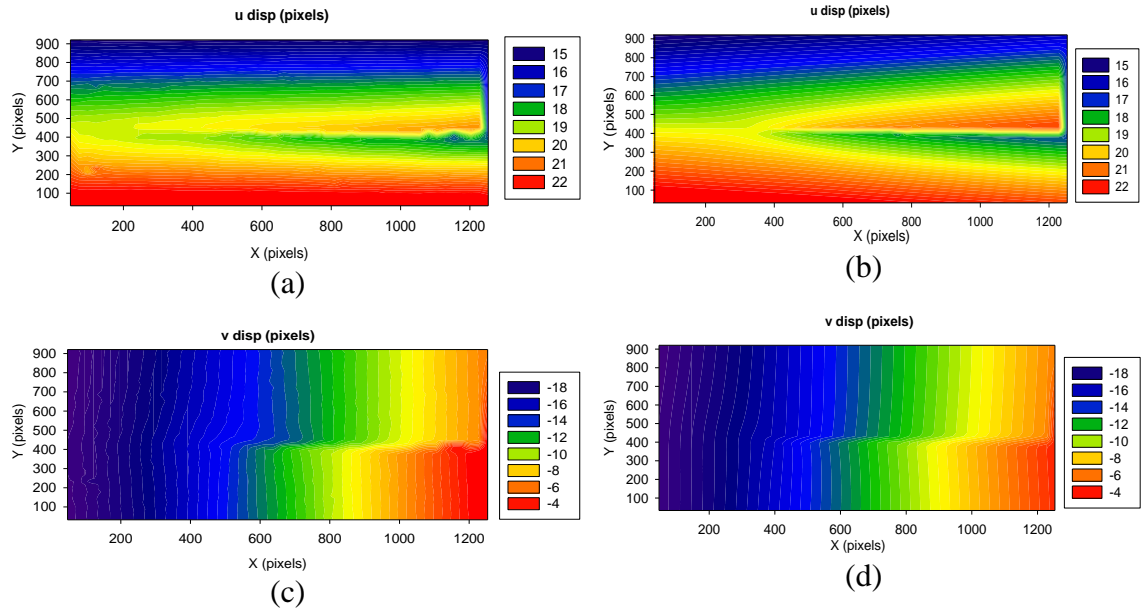
Figure 5.20 Full field displacements comparing DIC measurement (a,c) and fit using LEFM theory (b,d) u and v fields at 8500 cycles
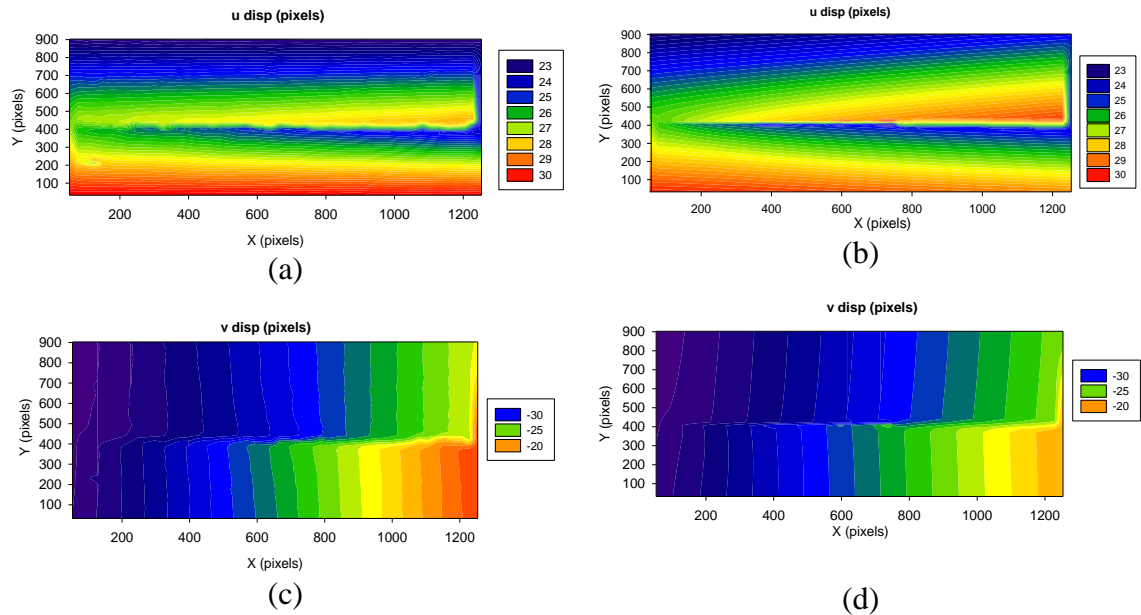
Figure 5.21 Full field displacements comparing DIC measurement (a,c) and fit using LEFM theory (b,d) u and v fields at 15500 cycles
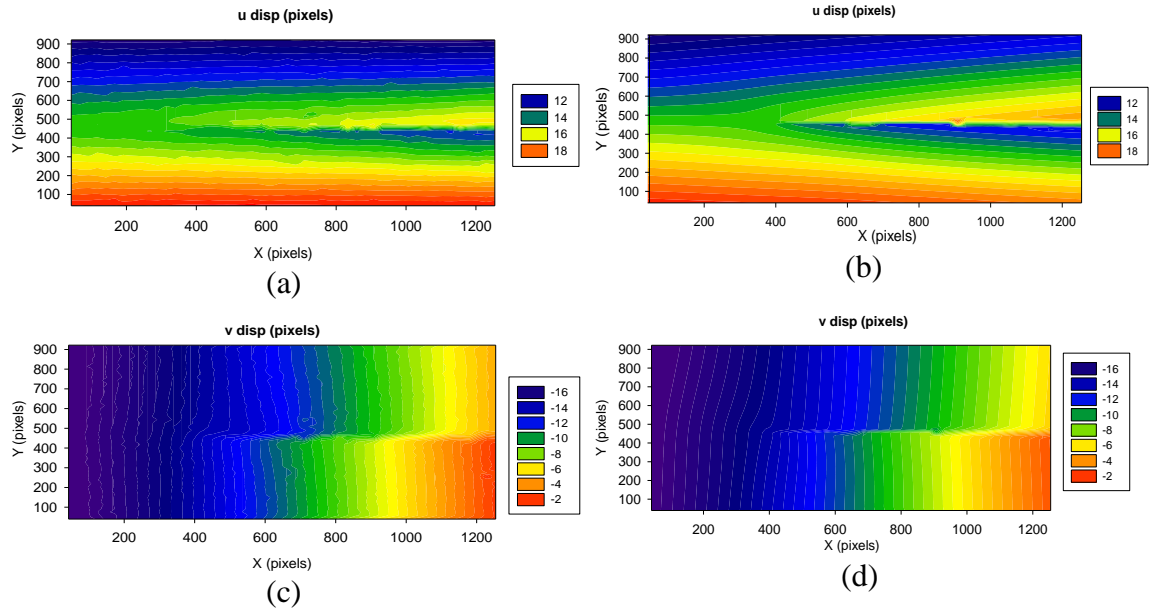
Figure 5.22 Full field displacements comparing DIC measurement (a,c) and fit using
LEFM theory (b,d) u and v fields at 35000 cycles

5.6 Mechanisms - Fiber Bridging and Crack Shielding

Fiber bridging was observed behind the crack tip at higher magnification images of the

crack propagation under cyclic loading in contrast to quasi-static monotonic loading (see

Figure 5.23 (a)). The fiber bridging at the crack face as shown in *Figure 5.23 (b)* was

observed for a specimen under 22 % mode mixture loading at around 1200 cycles

corresponding to around 66 N load. On the contrary, the deformation field used to

determine the energy release rates is based on LEFM ignoring any fiber bridging

mechanism. In the present experiment, the effects of the fiber bridging phenomenon on the

strain field can be seen in *Figure 5.23 (c).* From preliminary analysis it can be seen that

fibers have accumulated some strain energy and they do have effect on the crack growth.

Hence, fiber bridging cannot be ignored while analyzing the deformation fields. The crack

growth is halted by the reinforcing fibers, and secondly because the strength of the fiber is

too high for it to fail about the crack tip stress concentration. Increasing the applied load causes the shear stress developed at the interface to exceed the interface shear strength, resulting in local interface debonding.

(a)

(b)

Bundle of fibers
bridging crack

-0.02 E_{xy} 0.016

(c)
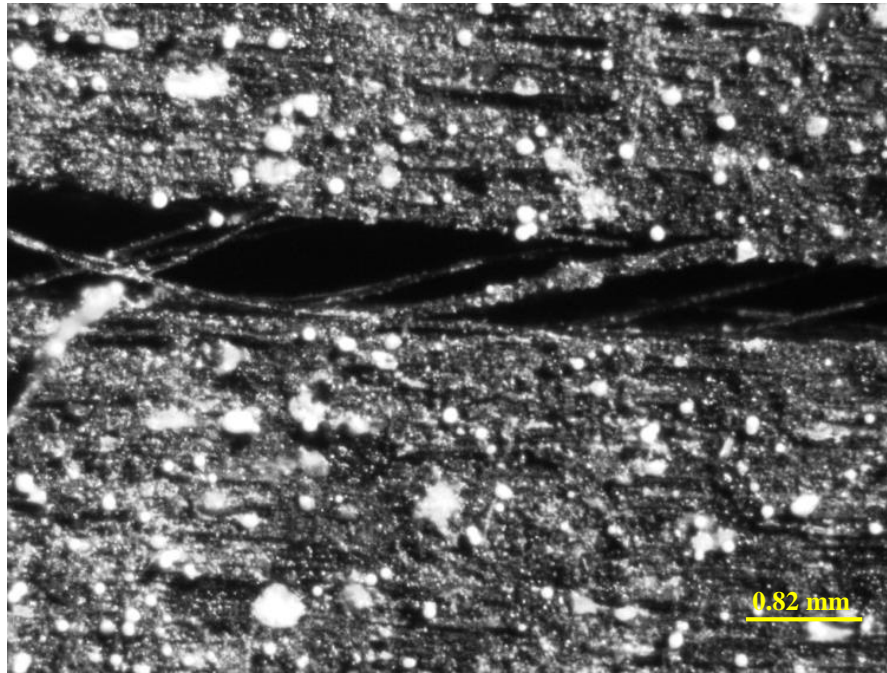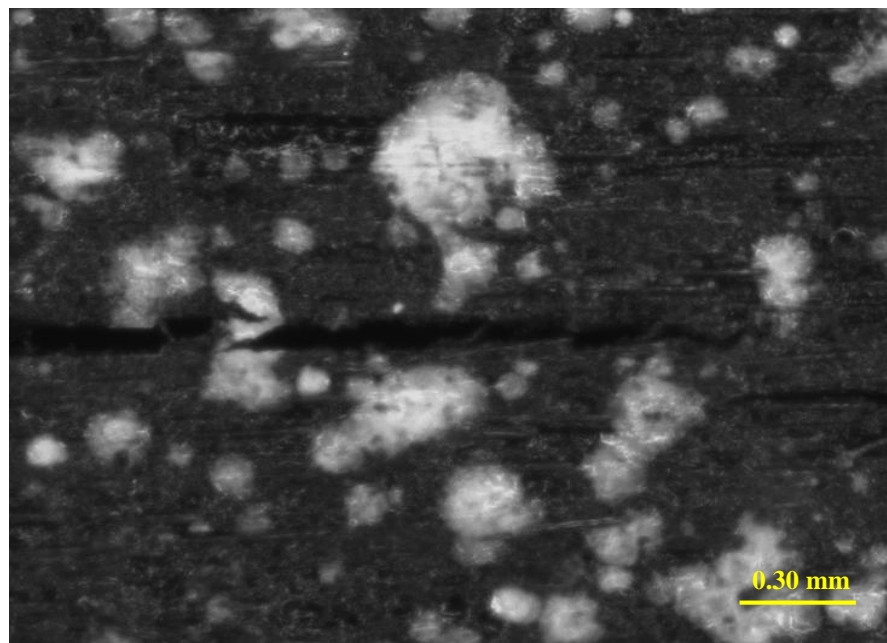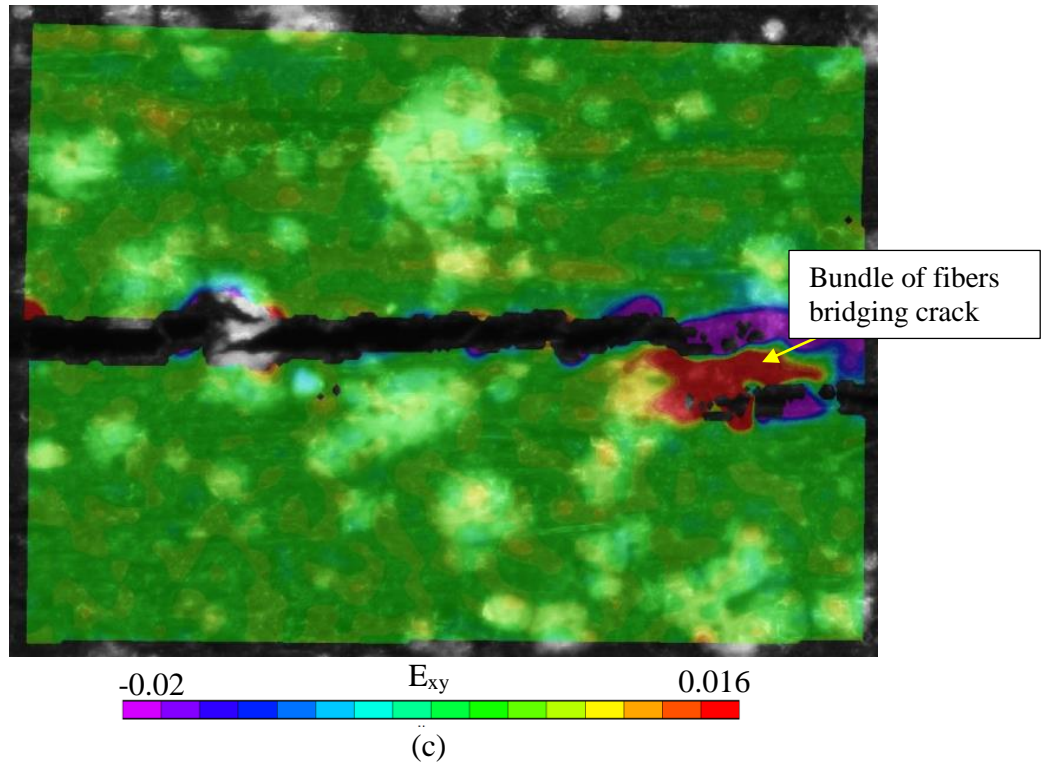
Figure 5.23 Fiber bridging in 22% mixity specimen at (a) 40 X magnification, (b) 70 X magnification (c) ϵ_{xy} strain field behind the crack tip after 1200 cycles at 66 N load

6 Future Work

In this chapter, future directions of the present research that can be carried out towards further understanding of the fatigue fracture behavior of laminated composite structures are identified and outlined. The scope for further exploration are:

6.1 Characterization of Fiber Bridging and its Effects on Cyclic Loading Parameters

In the present study, fiber bridging and secondary cracks have been observed to be dominant under the fatigue loading *Figure 6.1*. The secondary cracks absorb strain energy at the tips manifesting higher energy release rate through the global load displacement response and fiber bridging enhances the crack propagation resistance. Therefore, analyzing shielding mechanisms like fiber bridging and interlaminar surface friction under cyclic loading will further enhance the accurate identification of strain energy absorption mechanisms and hence, energy release rate. The characterization of secondary crack is necessary to develop a more accurate method of analyzing fracture parameters in laminated composite materials. Several publications are available [51, 52, 53] that discuss the dependence of resistance to delamination on fiber crossover bridging and the specimen geometry in pure mode I loading. Although DIC has been utilized to study fiber bridging in this study, higher magnification analysis on artificially induced fiber bridging between the laminates is required. Current resources restrict this to the edges of the specimen which may or may not be present within the specimen between the laminates. Furthermore, this analysis needs to be extended to mixed mode loading where fiber bridging is accompanied by surface friction as well.
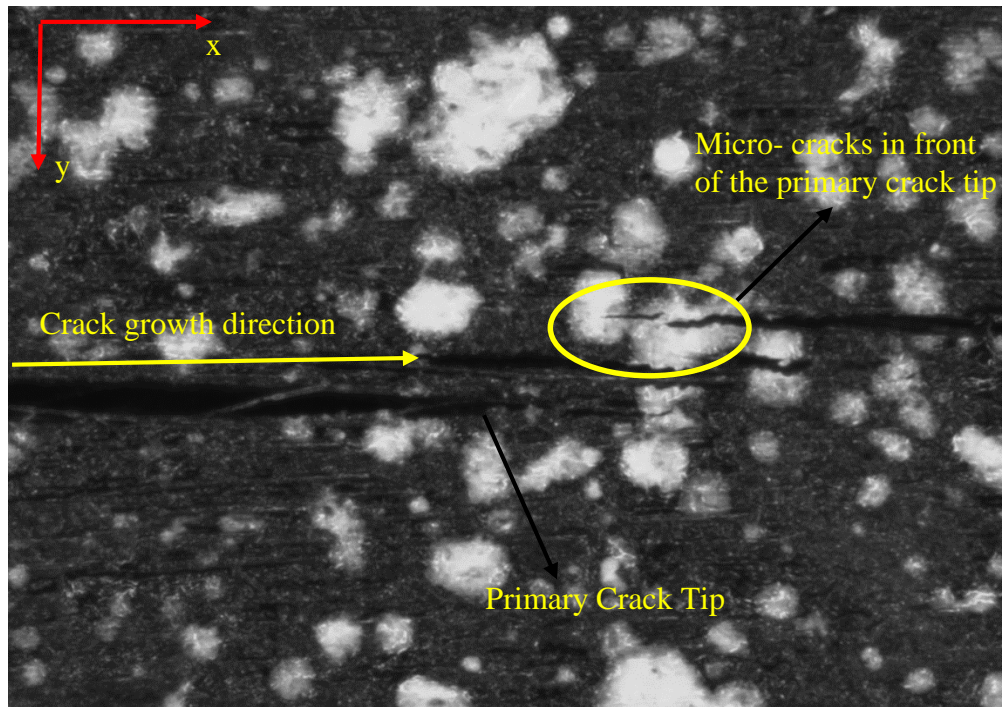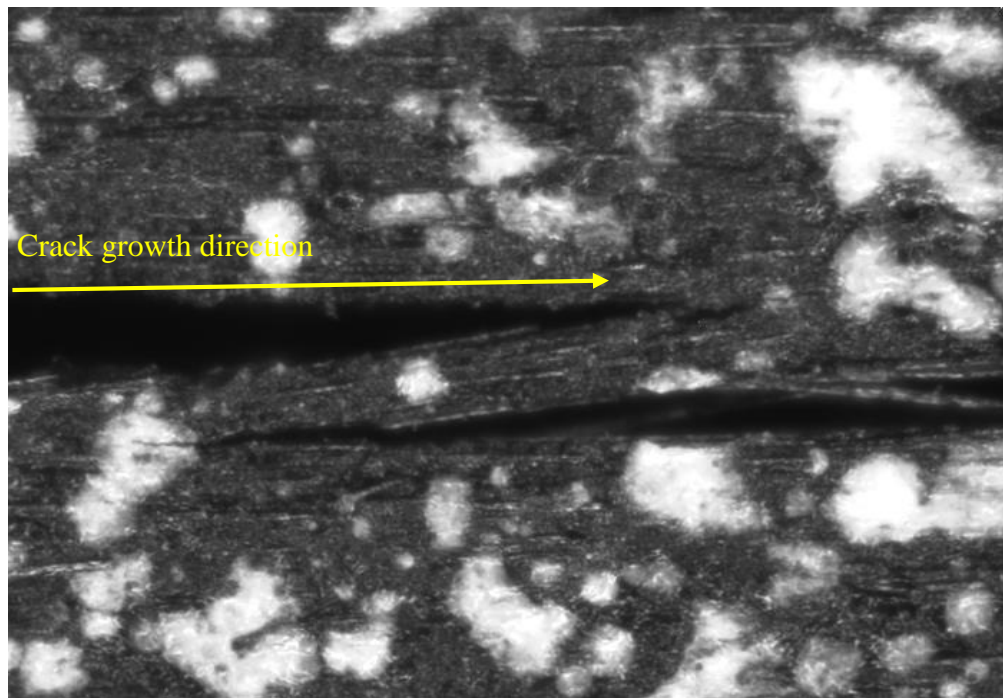
Figure 6.1 (a) Image taken at 40X magnification (b) Image taken at 60X magnification showing extensive fiber bridging behind the crack tip and secondary crack growth in front of the crack tip

6.2 Integration with Paris Law for Fatigue Life Prediction

The present characterization method of energy release rate and identification of crack length using DIC can be used in combination with Paris Law for life prediction of the laminates. Paris law is the standard empirical relation between the amplitude of strain energy release rate and the mode ratio. It is given by:

$$\frac{\delta a}{\delta N} = C\left(\frac{\Delta G}{G_c}\right)^m \qquad (6.1)$$

where,

a is the crack length, N is the number of cycles, ΔG is the change in strain energy release rate, parameters C and m are determined experimentally. The damage mechanics described by CZM when applied to cyclic loading conditions must reproduce the fatigue growth rate as described by Paris law [54]. A preliminary model was developed by fitting a curve to the data obtained from 100 % mode mixity test over 65000 cycles. *Figure 6.2* shows the power curve fitted to the experimental strain energy data obtained from 100 % mode mixity. At this stage, it was not possible to fit the Paris law model to the far field strain energy values as it is a tedious process which requires a large number of data points to be calculated using the Excel function over entire duration of the test. For clarity, the values of the energy release rate range on the horizontal axis have been normalized by the critical energy release rate obtained from the quasi-static tests. The material parameters were found to be *C= 3E-04* and *m= 0.4557* from the fitting curve.

$$y = 0.0003x^{0.4557}$$
$$R^2 = 0.995$$
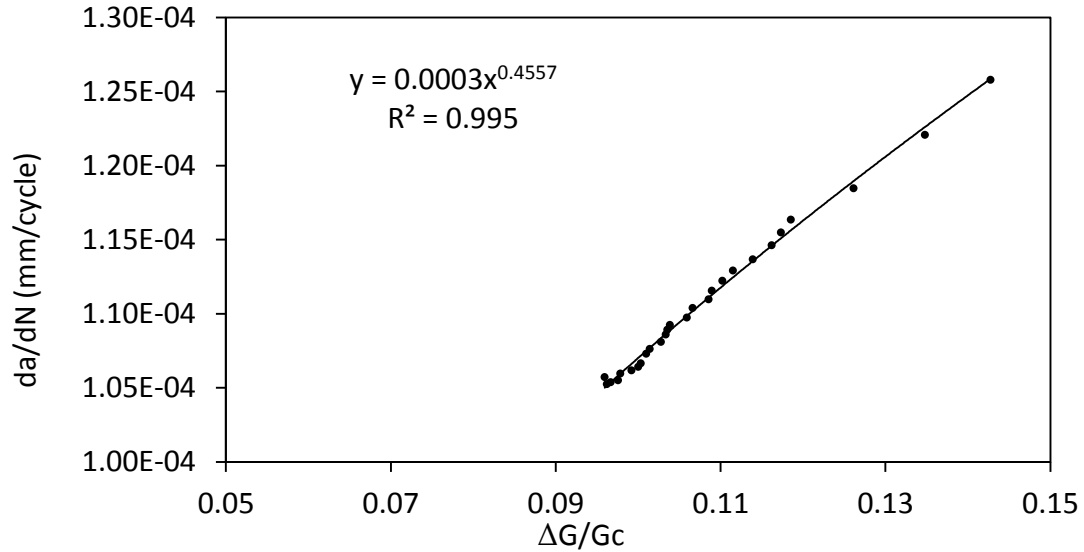
Figure 6.2 Experimental fatigue propagation rates for 100 % mode mixity

6.3 Computational Modeling Accounting for Local Mechanisms

Detailed computational modeling of the fatigue fracture behavior is required to understand the failure mechanisms under cyclic loading better and faster using techniques like Finite Element Analysis (FEA). Cohesive Zone Modelling (CZM) implemented with FEM serves as a good methodology to simulate damage in realistic composite geometries. The CZM technique is a unique combination of the concept of strain energy release rate as a criterion used in fracture mechanics for crack propagation and the damage mechanics of a non-linear process zone ahead of the crack tip described in terms of stiffness degradation [54]. Thus, analysis at higher magnifications is necessary to reliably measure crack tip fields and the process zone. As fracture mechanics based approach requires the determination of the initial flaw (crack) which can be difficult to locate a priori in the structure, crack propagation can be modeled using Cohesive Zone Modelling (CZM). The CZM model would allow us to perform a damage progressive analysis and include the effects of an eventual non-negligible fracture process zone at the crack tip, thus not being

87

restricted to linear elastic fracture mechanics assumptions [29]. The damage parameter in CZM can be integrated into a fatigue law to simulate delamination of composites under fatigue loading. Using the present methodology, CZM parameters can be identified for a crack tip. Therefore, the present approach of experimental determination of energy release rate and crack tip features will compliment more data-enriched and accurate modeling.

A study has been undertaken at UMD by Virakhti et al. [54] to simulate crack propagation under fatigue loading. The goal of the study is to develop a numerical fatigue damage model that can be incorporated in a finite element model to simulate composite laminate failure under cyclic loading.

7 Conclusions

This chapter will present the intellectual and the technical contributions resulting from this research.

7.1 Intellectual Contributions

The research work reported in this thesis is expected to yield contributions to the field of characterization of laminated composites and understanding the micro-mechanical principles for strain energy dissipation in these composites. Attempt has been made to utilize a non-contact optical technique, DIC to estimate the fracture parameters accounting for the deformations around crack tip. The present work has been established extending the previous work by Puishys et al. [8] that characterized mixed mode fracture under quasi-static loading. The most important and potentially useful contributions are: (1) understanding fracture mechanics under fatigue loading via strain energy release rate and failure mechanisms in the laminated composite structures; (2) Use of ASTM standards to develop a protocol for characterizing damage under cyclic loading using DIC; A new test protocol was developed for testing laminated composites under cyclic mixed mode loading using the Mixed Mode Bending (MMB) fixture to obtain mode-mixity in loading and DIC for measuring crack tip displacement fields.

7.1.1 Application of DIC for Energy Release Rate measurement under Cyclic Load

DIC was used to determine the energy release rate of carbon fiber laminated composites under cyclic loading. The deformation fields measured by DIC was analyzed using LEFM to obtain the energy release rate. With the use of displacement field equations

it was possible to calculate mode I and II component of strain energy release rate more accurately, which was found to be sensitive to the exact crack tip location. A comparison of mixed mode energy release rates obtained from global load response and that obtained from full field deformation measurement by DIC was made. The methodology relying on the imaging of crack tip fields helps elucidating the mechanisms that take place near the crack tip and affect the dissipation of energy during crack growth. It was also found that strain energy release rate and mode mixity behave differently near the crack tip and are not necessarily similar to that determined from the global applied mixity in load condition or load response. The following tables provide summary of the results for various mode mixities.

No. of Cycles	Global GI [J/m^2]	Global GII [J/m^2]	Mixity [%]	Full field GI [J/m^2]	Full field GII [J/m^2]	Mixity [%]	GI (50 Pixels around crack tip) [J/m^2]	GII (50 Pixels around crack tip) [J/m^2]	Mixity [%]
300	23.31	0.051	0.22	22.72	0.051	0.22	23.30	0.051	0.22
600	30.62	0	0	12.77	1.06	7.69	12.76	1.06	7.67
2400	31.63	0	0	28.23	0	0	28.23	0	0

Table 7.1 Summary of strain energy release rate variation with number of cycles at 30 N under Pure mode I (0% mixity) comparing the global values with full field and small field data

No. of Cycles	Global GI [J/m^2]	Global GII [J/m^2]	Mixity [%]	Full field GI [J/m^2]	Full field GII [J/m^2]	Mixity [%]	GI (100 Pixels around crack tip) [J/m^2]	GII (100 Pixels around crack tip) [J/m^2]	Mixity [%]
5	97.76	29.97	23.46	65.21	39.02	37.48	35.17	25.14	42.68
40	98.79	30.30	23.47	65.57	51.5	43.99	54.75	51.95	48.68
386	113.01	34.87	23.58	131.63	52.05	28.34	108.81	79.763	42.30
515	113.813	35.14	23.59	188.17	55.99	22.93	128.92	76.68	37.30

Table 7.2 Summary of strain energy release rate variation with number of cycles at 79 N under mixed mode (22% mixity) comparing the global values with full field and small field data

No. of Cycles	Global GI [J/m²]	Global GII [J/m²]	Mixity [%]	Full field GI [J/m²]	Full field GII [J/m²]	Mixity [%]	GI (100 Pixels around crack tip) [J/m²]	GII (100 Pixels around crack tip) [J/m²]	Mixity [%]
130	36.31	38.87	51.70	24.11	27.49	53.28	23.92	27.55	53.50
905	208.29	224.51	51.87	208.99	209.17	50.02	58.72	23.14	28.27
1290	220.27	238.19	51.95	170.30	208.38	55.64	170.30	208.38	55
1950	225.80	244.43	51.98	184.14	261.05	58.64	57.60	10.73	15.70
3235	242.76	263.56	52.05	285.88	285.20	49.94	285.90	285.09	49.94

Table 7.3 Summary of strain energy release rate variation with number of cycles at 220 N under mixed mode (50% mixity) comparing the global values with full field and small field data

No. of Cycles	Global GI [J/m²]	Global GII [J/m²]	Mixity [%]	Full field GI [J/m²]	Full field GII [J/m²]	Mixity [%]
2600	0.06	67.09	99.91	54.47	261.93	82.78
5500	0.07	70.17	99.91	39.48	189.19	82.74
12500	0.07	72.41	99.91	20.15	140.25	87.44
15500	0.07	74.08	99.91	16.73	119.37	87.81
28000	0.08	80.21	99.91	5.95	89.27	93.75
35000	0.08	82.89	99.91	5.31	95.15	94.71

Table 7.4 Summary of strain energy release rate variation with number of cycles at 150 N under pure mode II (100% mixity) comparing the global values with full field data

The results from 100% mode mixity do not show the near field data as it did not change and was similar to the full field data obtained from DIC.

DIC offers several advantages over traditional methods of data extraction. There is no need for calibration specimens, no need for compliance correction of the fixture, and no uncertainty from material properties. DIC being a non-contact visual inspection technique compares an undeformed reference image with a deformed image of the specimen. The relative change in u and v field displacements can then be used to calculate the local strain

91

energy values around the crack tip. Furthermore, in order to account for local damage mechanisms, higher magnification images are required. Higher magnification reduces the field of view (FOV) and it becomes difficult to focus on a smaller area with much accuracy. Thus, simultaneous comparison between near field data and far field data becomes difficult and requires constant adjustment to the frame of reference. However, these problems can be overcome by using different lenses to capture the field of views of different size and correlating the measurements obtained from them.

By limiting the area that is analyzed around the crack tip to fit to the theoretical deformation field obtained from LEFM, the validity and size of the K, G-dominance fields can be verified. Experimental measurements show that the mode mixity determined from the full field deformation measured by DIC depends on the field size. Therefore, a wise judgment is required to determine the size of field of view that will capture the material response accurately. This is illustrated in Table 7.5

	G_I (J/m^2)	G_{II} (J/m^2)	G_{total} (J/m^2)	Mixity %
Global data	225.80	224.42	470.23	51.98
Local data (250 pixels around crack tip)	184.14	261.05	445.19	58.64
Local data (50 pixels around crack tip)	57.6	10.73	68.33	15.70

Table 7.5 Comparison of strain energy release rate from global, far field and near field data for 50 % mode mixity test at 1950 cycles 218N load.

7.1.2 Fatigue Fracture Characterization of Carbon Fiber Laminate

ASTM standards were used to fabricate carbon fiber laminates from unidirectional pre-preg plies and characterize their fracture behavior under mixed mode cyclic loading. The

global load response was obtained from the load frame and deformation was measured by DIC. The data collected from analyzing these global load response were compared to full field data obtained from DIC. Unlike quasi-static tests under mixed mode loading, cyclic tests take much longer to conduct and require careful preparation of the setup. The slow crack propagation introduced new challenges like occasional adjustment of the reference frame at un-deformed position in order to track the crack growth and to position the crack tip in the center of the field of view. It was necessary to maintain the crack tip at the center of the field of view in order to characterize damage in front and behind the crack tip. Cyclic loading resulted in a more stable crack growth under higher mode II cases. This was especially beneficial in 50% and 100% mode mixities where, it is difficult to record a stable crack growth and to find the critical strain energy release rates.

7.1.3 Identification of Micro- scale Mechanisms under Fatigue Loading

Digital Image Correlation (DIC) has been used for local deformation measurement around the crack tip and hence, can be used for developing a more data enriched computational model. Below is shown a local mechanism, e.g. fiber bridging that absorbs strain energy at micro-scale.
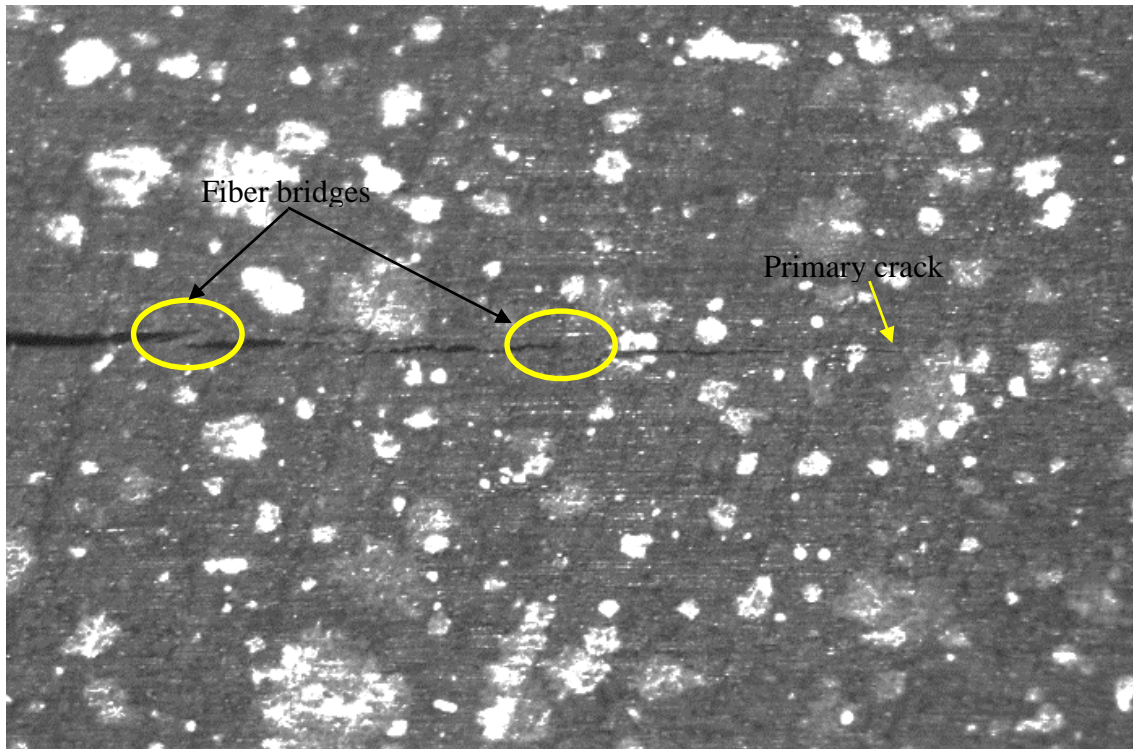
Figure 7.1 Fiber bridging and secondary crack growth behind the primary crack tip under 22% mode mixity

7.1 Anticipated Benefits

The results detailed in Chapter 5 characterize crack growth in unidirectional carbon fiber laminates under fatigue loading. The implementation of DIC has helped to observe near field and full field effects from global load response. The experimental measurements reported in this work will be used to compliment more data enriched numerical modeling of fatigue fracture of these materials using CZM at the University of Maryland. The goal of the CZM approach is to predict crack growth under fatigue loading and also take into consideration the crack shielding effects like fiber bridging and inter-laminar surface friction.

Bibliography

1.   Mouritz A.P.,Gellert E., Burchill P., Challis K. (2001) Review of advanced composite structures for naval ships and submarines, Composite Structures, 53: 21-41
2.   CFRP applications to aircraft (2013) The Japan Carbon Fiber Manufacturing Association
3.   Lacovara R. (2012) The Power of Statistics in a Growing Industry, Composites Manufacturing Online
4.   Jahn B., Karl D., (2012) Composites Market Report 2012- Market developments, trends, challenges and opportunities, AVK (Federation of Reinforced Plastics), 15/29
5.   Roberts A. (2011) The Carbon Fiber Industry Worldwide 2011-2020: An Evaluation of Current Markets and Future Supply and Demand, Materials Technology Publications
6.   Haldar S., Bruck H.A. (2014) Mechanics of Composite Sandwich Structures with Bioinspired Core, Composites Science and Technology, 95:67-74
7.   Rotem A., Nelson H.G. (1989) Failure of a Laminated Composite Under Tension-Compression Fatigue Loading, Composites Science and Technology 36:45-62
8.   Puishys J., Bruck H.A. (2012) Determination of Mixed Mode Energy Release Rates in Laminated Carbon Fiber Composite Structures using Digital Image Correlation, University of Maryland
9.   Mitrovic M., Hahn H. T., Carman G. P. (1999) Effect of loading parameters on the fatigue behavior of impact damaged composite laminates, Composites Science and Technology, 56: 2059-2078
10.   Pascoe J.A., Alderliesten R.C., Benedictus R. (2013) Methods for the Prediction of Fatigue Delamination Growth in Composites and Adhesives Bonds- A Critical Review, Engineering Fracture Mechanics, 112-113: 72-96
11.   Ashcroft I. A., Shaw S.J. (2002) Mode I fracture of epoxy bonded composite joints 2. Fatigue loading, International Journal of Adhesion & Adhesives, 22: 151-167
12.   O'Brien T. K., Johnston W. M., Toland G. J. (2010) Mode II Interlaminar Fracture Toughness and Fatigue Characterization of a Graphite Epoxy Composite Material, NASA, Langley Research Center, TM-2010-216838
13.   Blanco N., Gamstedt E.K., Asp L.E. (2004) Mixed Mode Delamination Growth in Carbon-fiber Composite Laminates under Cyclic Loading, International Journal of Solids and Structures, 41: 4219-4235
14.   Hojo M., Matsuda S., Fiedler B. (2002) Mode I and II Delamination Fatigue Crack Growth Behavior of Alumina Fiber/Epoxy Laminates in Liquid Nitrogen, International Journal of Fatigue, 24(2-4): 109-118
15.   Puishys J., Haldar S., Bruck H.A. (2014) Characterization of Mixed-Mode Energy Release Rates for Carbon Fiber/Epoxy Composites Using Digital Image Correlation, Proceedings of the 2013 Annual Conference on Experimental and Applied Mechanics, 6: 109-115
16.   ASTM Standard D6115-97 (2011) Standard Test Method for Mode I Fatigue Delamination Growth Onset of Unidirectional Fiber-Reinforced Polymer Matrix Composites

17. ASTM Standard D6671/D6671M (2006) Standard Test Method for Mixed Mode I-Mode-II Interlaminar Fracture Toughness of Unidirectional Fiber Reinforced Polymer Matrix Composites

18. Chapter 7: Advanced Composite Materials- Federal Aviation Administration regulations

19. Baral N., Guezenoc H. (2008) High modulus carbon fiber composites: Correlation between transverse tensile and mode I interlaminar fracture properties, Materials Letters, 62, 6-7:1096-1099

20. Pinho S.T., Robinson P. (2006) Fracture toughness of the tensile and compressive fiber failure modes in laminated composites, Composites Science and Technology, 66: 2069-2079

21. Nikbakht M., Choupani N. (2008) Fracture Toughness Characterization of Carbon-Epoxy Composite Using Arcan Specimen, World Academy of Science, Engineering and Technology, 41: 738-744

22. Faulstich de Paiva J. M., Mayer S. (2005) Evaluation of Mechanical Properties of Four different Carbon/Epoxy Composites used in Aeronautical Field, Materials Research, 8, 1: 91-97

23. Robinson R., Cracking dams, http://simscience.org/cracks/advanced/math1.html

24. Adams D. F., Carlsson L.A., Pipes R. B. (2003) Experimental Characterization of Advanced Composite Materials, 3rd Edition Boca Raton, FL: CRC Press 185-210

25. Carlsson L. A., Pipes R. B. (1987) Experimental Characterization of Advanced Composite Materials, Englewood Cliffs, NJ: Prentice Hall, Inc., 157-191

26. Haslach H. W., Armstrong R. W. (2004) Deformable Bodies and Their Material Behavior, Danvers, MA: John Wiley & Sons, Inc., 383-425

27. Tada H., Paris P.C., Irwin G.R. (2000) The Stress Analysis of Cracks Handbook(3ed), ASME

28. Priel E., Bussiba A., Gilad I. (2007) Mixed mode Failure Criteria for brittle elastic V-notched structures, International Journal of Fracture, 144: 247-265

29. Dias G. F., de Moura M.F.S.F. (2013) Cohesive laws of composite bonded joints under mode I Loading, Composite Structures, 106: 646-652

30. Poursartip A., Gambone A., Ferguson S. (1998) In-Situ Measurements of Crack Tip Displacements in Composite Laminates To Determine Local G in Mode I and II, Engineering Fracture Mechanics, 60: 173-185

31. Miyajima T., Sakai M. (1991) Fiber Bridging of a Carbon Fiber-Reinforced Carbon Matrix Lamina Composite, Journal of Materials, Materials research Society, 6: 539-547

32. Lekhnitskii S.G. (1963) Theory of Elasticity of an Anisotropic Body, Holdenday, San Francisco, CA

33. Sih G.C., Paris P.C., Irwin G.R. (1965) On Cracks in Rectilinearly Anisotropic Bodies, International Journal of Fracture Mechanics, 42: 65-75

34. Sutton M.A. (2013) Computer Vision-Based Non-contacting Deformation Measurements in Mechanics: A Generational Transformation, Applied Mechanics Reviews, ASME 65:050000-1-23

35. Bruck H. A., McNeill S. R., Sutton M. A., and Peters (1989) Determination of Deformations Using Digital Correlation With the Newton Raphson Method for Partial Differential Corrections, Experimental Mechanics, 29(3): 261–267.

36. Haldar S., Bruck H.A. (2013) Characterization of Dynamic Damage Mechanisms in Palmetto Wood as Biological Inspiration for Impact Resistant Polymer Composites, Mechanics of Materials, 57: 97-108

37. Hamam R., Hild F., Roux S. (2007) Stress Intensity Factor Gauging by Digital Image Correlation: Application in Cyclic Fatigue, Strain, 43: 181-192

38. Mogadpalli G.P., Parameswaran V. (2008) Determination of Stress Intensity Factor for Cracks in Orthotropic Composite Materials using Digital Image Correlation, Strain, 44: 446-452

39. Bruck H.A. (2014) "ENME 672: Composite Materials", Lecture Notes, University of Maryland, 4: 9-16

40. Williams J.G., (1989) The Fracture Mechanics of Delamination Tests, Journal of Strain Analysis, 24(4): 207-214

41. Kinloch A.J., Wang Y., Williams J.G. (1993) The Mixed Mode Delamination of Fiber Composite Materials, Composites Science and Technology, 47(3): 225-237

42. Wang Y., Williams J.G. (1992) Corrections for Mode II Fracture Toughness Specimens of Composites Materials, Composites Science and Technology, 43(3): 251-256

43. Bhashyam S., Davidson B.D. (1997) Evaluation of Data Reduction Methods for the Mixed Mode Bending Test, AIAA Journal, 35: 546-552

44. Balzani C., Wagner W. (2012) Adhesive Joints in Composite Laminates- A Combined Numerical/ Experimental Estimate of Critical Energy Release Rates, International Journal of Adhesion & Adhesives, 32: 23-38

45. Brunner A.J., Murphy N., Pinter G. (2009) Development of a Standard Procedure for the Characterization of Interlaminar Delamination Propagation in Advanced Composites under Fatigue Mode I Loading Conditions, Engineering Fracture Mechanics, 76: 2678-2689

46. Brunner A.J., Blackman B.R.K., Williams J.G. (2006) Calculating a Damage Parameter and Bridging Stress from G_{IC} Delamination Tests on Fiber Composites, Composites Science and Technology, 66: 785-795

47. ASTM Standard D5528 (2013) Standard Test Method for Mode I Interlmainar Fracture Toughness of Unidirectional Fiber-Reinforced Polymer Matrix Composites

48. Vic-2D 2009 Reference Manual, Correlated Solutions

49. Liu C., Rosakis A.J., Ellis R.W. Stout M.G. (1998) A Study of the Fracture Behavior of Unidirectional Fiber –Reinforced Composites Using Coherent Gradient Sensing(CGS) interferometry, International journal of Fracture, 90: 355-382

50. Shukla A., Agarwal B.D., Bhushan B. (1989) Determination of Stress Intensity Factor in Orthotropic Composite Materials Using Strain Gauges, Engineering Fracture Mechanics, 32(3): 469-477

51. Miyajima T., Sakai M. (1991) Fiber Bridging of a Carbon Fiber –Reinforced Carbon Matrix Lamina Composite, Journal of Materials Research, 6(3): 539-547

52. Tamuzs V., Tarasovs S., Vilks U. (2001) Progressive Delamination and Fiber Bridging Modelling in Double Cantilever Beam Composite Specimen, Engineering Fracture Mechanics, 68, 513-525

53.   Sorensen B. F., Jacobsen T.K. (1998) Large Scale Bridging in Composites: R-curves and Bridging Laws, Composites Part A, 29A, 1443-1451

54.   Virakhti A., Lee S.W. (2014) Unpublished work, University of Maryland